Stony Brook University

Modeling study of flocculation effects on sediment transport in estuaries

A Dissertation Presented

by

Fanghua Xu

to

The Graduate School

in Partial Fulfillment of the

Requirements

for the Degree of

Doctor of Philosophy

in

Marine and Atmospheric Science

Stony Brook University

May 2009

Stony Brook University

The Graduate School

Fanghua Xu

We, the dissertation committee for the above candidate for the
Doctor of Philosophy degree, hereby recommend acceptance of this dissertation.

Advisor
Dong-Ping Wang, Professor
School of Marine and Atmospheric Sciences, Stony Brook University

Chairman
Roger D. Flood, Professor
School of Marine and Atmospheric Sciences, Stony Brook University

Kamazima M.M. Lwiza, Associate Professor
School of Marine and Atmospheric Sciences, Stony Brook University

Nicole Riemer, Assistant Professor
Atmospheric Sciences, University of Illinois at Urbana-Champaign

Gail C. Kineke, Associate Professor
Department of Geology and Geophysics, Boston College

This dissertation is accepted by the Graduate School

Lawrence Martin

Dean of the Graduate School

Abstract of the Dissertation

Modeling study of flocculation effects on sediment transport in estuaries

by

Fanghua Xu

Doctor of Philosophy

in

Marine and Atmospheric Science

Stony Brook University

2009

Our current understanding of sediment transport in rivers and estuaries is insufficient to permit quantitative predictions of the fate of fine-grained sediment particles. In order to improve our ability to model sediment transport and depositional patterns, flow models need to be coupled with models that allow for the creation and destruction of flocs and subsequent changes in their settling velocity. A size-resolved flocculation model has been developed and tested to fulfill this goal. The flocculation model can predict the temporal evolution of the floc size distribution undergoing aggregation and breakup. In addition to flocculation, a one-dimensional (1-D) model has been developed where we consider particle settling, deposition and erosion and calculate the floc size distribution depending on friction velocity. The 1-D simulation is verified by comparing with observed size distributions over tidal cycles by *Bale et al.* [2002]. The flocculation scheme has been successfully incorporated with the sediment transport component in a 3-D hydrodynamic circulation model (Princeton Ocean Modeling

(POM)). An idealized study to simulation of ETM variations over tidal cycles has been carried out. The continuous variations in floc size and settling velocity from the model study indicate that a fixed settling velocity does not well represent particle settling. The combination of gravitational circulation convergence and tidal asymmetry associated with settling flocs are primarily responsible for an ETM formation. Lateral circulation in estuaries which results in cross-channel transport of water mass and suspended sediments is important for lateral trapping of particles and formation of axial asymmetrical channel profile. An idealized three-dimensional simulation is done to investigate the effects of lateral circulation on lateral trapping of sediments associated with flocculation processes.

Table of Contents

List of Figures

Chapter 2

Chapter 3

Chapter 4

List of Tables

Chapter 2

Chapter 3

Acknowledgements

I would like to thank all people who have helped and inspired me during my doctoral study at Stony Brook University.

Especially, I want to thank my advisor, Professor Dong-Ping Wang, for his guidance during my study at Stony Brook University. His perpetual energy and enthusiasm in research has motivated all his students, including me. In addition, he is always accessible and willing to help and encourage his students. As a result, research life becomes smooth and rewarding for me.

I am gratefully indebted to Prof. Nicole Riemer, of University of Illinois at Urbana-Champaign, for helping me develop the size-resolved flocculation model and many helpful discussions and comments about my research.

Prof. Flood, Prof. Lwiza, and Prof. Kineke deserve a special thank as my thesis committee members. They give me many kind comments to my dissertation and help me to improve my research.

I also like to thank Prof. Wilson, my counselor in my first year, who encourages me and helps me to start a doctorate study at Stony Brook University.

All my colleagues have made SOMAS a convivial place to work. In particular, I would like to thank Yuan Liu and Tiantian Tang for our long-term friendship, Dr. Wuyin Lin for helping solving computer problems, and Zhenrui Cao, Dr. Peng Cheng, Yanjuan Guo, Jie Gong, Dr. Yan Hao, Xiaona Li, Dr. Xiaolin Li, Dr. Jenq-Chi Mau, Hua Song, Jingdong Wang, Dr. Jun Wei, Yi Zheng for inspiring me in research and life.

Most of all, my special gratitude go to my family, especially my parents and husband, for their unflagging love and support throughout my life.

Chapter 1

Introduction

1.1 Motivation

Estuaries have been observed to slowly fill up with sediment (Meade, 1969). Sediment accumulation is attributed to decreasing flow velocities and flocculation of fine particles (Menon et al., 1998). Flow conditions in estuaries continuously rework sediment distribution. The transport, sedimentation, temporary storage, and resuspension constitute a significant loop for sediment dispersion in estuaries and coastal areas. The flocculation, including aggregation and breakup, alters the pattern of sediment settling and transport and subsequently further complicates the dispersal of the suspended sediments. Therefore, quantitative prediction of the fate of fine-grained sediment requires the flocculation to be included in sediment transport models.

1.2 Overview

In order to improve our ability to model sediment transport and depositional patterns, circulation models need to be coupled with models that allow for the creation and destruction of flocs and subsequent changes in their settling velocity. In Chapter 2 (published in Continental Shelf Research), a size-resolved flocculation model is described. It approximates the real size distribution of particles by a range of size bins and solves a mass balance equation for each bin. The flocculation model alone (no transport at this point) predicts the temporal evolution of the floc size distribution

undergoing aggregation and breakup, by considering the influence of turbulence. The simulated floc size distributions are compared with the lab experiment of Winterwerp (1998). In addition, a one-dimensional (1-D) model is developed where we consider particle settling, deposition and erosion. The effects of differential settling are also included. The 1-D simulation is verified by comparing with observed size distributions over tidal cycles by Bale et al. (2002). Floc size is small during maximum currents and increases with decreasing currents.

The flocculation model is incorporated with the sediment transport component in a three-dimensional (3-D) hydrodynamic circulation model (Princeton Ocean Modeling (POM)). In Chapter 3 (submitted to Continental Shelf Research), we carry out a series of idealized study to simulate suspended sediment trapping near the salt front over tidal cycles in a two-dimensional (2-D) model domain (x,z). The size-resolved flocculation simulation generates the continuous variations in floc size and settling velocity. Intense sediment trapping occurs near the salt front. Also, strong flood-ebb asymmetry in sediment trapping is observed. This is consistent with observations in the estuarine turbidity maximum (ETM) of the upper Chesapeake Bay, where elevated near bottom suspended sediment concentration was observed during maximum currents, with concentration three times higher on flood than on ebb (Sanford et al. 2001). The comparison between size-resolved flocculation simulation and one-size flocculation simulation indicates that a fixed settling velocity cannot well represent particle settling. The combination of gravitational circulation convergence and tidal asymmetry associated with settling flocs is primarily responsible for ETM formation.

Lateral circulation in estuaries which results in cross-channel transport of suspended sediments is important for lateral trapping of particles and formation of axial asymmetrical channel profile. In Chapter 4, an idealized 3-D simulation is done to investigate the effects of lateral circulation on lateral trapping of sediments associated with flocculation processes. The lateral flow exhibits a three-layer structure during flood with divergent currents at the surface and bottom and convergent currents at mid-depth. During ebb, the lateral circulation shows a two-layer structure with divergent flow near the surface and convergent flow in the deep water. Suspended sediment tends to be trapped near the salt front as in the 2-D simulation. For one-size flocculation simulation, most of suspended sediment tends to concentrate at the channel center with slight redistribution of suspended sediment toward banks by lateral advection. The stronger lateral circulation over the left bank than over the right (looking into the estuary) by bottom Ekman veering contributes to the higher suspended sediment concentration on the left bank. For the size-resolved flocculation simulation, the preferential sediment trapping on the left bank is further enhanced by right-left asymmetry in floc growth, which underlines the role of flocculation in long-term formation of estuary channel profile. Furthermore, the development of a pronounced ETM near the salt front is facilitated by floc size variations.

1.3 Future Study

In estuaries and coastal seas, floc size and settling velocity may change significantly in energetic environments. Real time in-situ monitoring and measurements of the flocs in some specific environments (e.g. Manning, 2001) have been collected. It is necessary to carry out a series of flocculation simulations with realistic forcing and

geometry. The flocculation model can be evaluated with these in-situ measurements, including time series of floc size spectrum and suspended sediment concentrations. Spatial and temporal variations in floc size and settling velocity associated with freshwater discharge, tides, topography, lateral circulations, winds, and surface gravity waves in estuaries and coastal waters should be explored. In addition, sediment consolidation and the decreasing of cohesive sediment erodibility with depth have been neglected in this study. Including these two processes in the simulation should improve prediction of the fate of suspended fine-grained sediment and help better understanding of short-time stratigraphy.

The role of small-scale, turbulence-induced shear in limiting maximal floc size has been challenged because prediction from this hypothesis has not succeeded in explaining the maximal floc size found in coastal waters (Geyer et al., 2004). Under low-to-moderate energy conditions floc size may be controlled by force acting on sinking particles instead of turbulence (Hill et al., 2001). The limited residence time also may prevent floc growth. Sensitivity analysis of the flocculation model is necessary to identify the role of turbulence. In addition, high suspended sediment concentration, like fluid mud, tends to suppress turbulence and produce hindered settling. Thus the interaction between turbulence and flocculation is complicated and challenging.

Particle stickiness is an important parameter in the flocculation model, and a constant value is used in the study. In reality, particle stickiness has a large natural variability, ranging from $O(10^{-3})$ to $O(1)$, which changes in response to composition and concentration of sticky organic matter in estuaries. However, an assessment of particle stickiness remains elusive. A degree of stickiness can be estimated through the content of

carbohydrates, uronic acids, or other extracellular polymeric substances (EPS) (Droppo et al., 2005). Therefore, it may be useful to interface with biological models to predict particle stickiness for flocculation simulation.

Most contemporary sediment transport models have oversimplified flocculation processes. Settling velocity is either assumed constant or is parameterized in terms of environmental conditions such as turbulence and suspended sediment concentration (Baugh and Manning, 2007). It seems promising to use flocculation model simulation to improve the empirical formula used in sediment transport models. This intermediate step is necessary because at present the 3D flocculation model is too expensive computationally to run for long-term (say, over a month) simulation. Alternatively, it may be feasible to simplify the flocculation scheme yet maintaining adequate accuracy for practical application.

References

Bale, A.J., Uncles, R.J., Widdows, J., Brinsley, M.D., Barrett, C.D., 2002. Direct observation of the formation and break-up of aggregates in an annular flume using laser reflectance particle sizing, in Winterwerp, J.C., Kranenburg C. (Eds.), Fine Sediment Dynamics in the Marine Environment, Elsevier, pp. 189-201.

Baugh, J.V., Manning, A.J., 2007. An assessment of a new settling velocity parameterization for cohesive sediment transport modeling, *Continental Shelf Research*, 27, 1835-1855.

Droppo, I.G., Leppard, G.G., Liss, S.N., Milligan, T.G., 2005. Opportunities, needs, and strategic direction for research on flocculation in natural and engineered systems. In: Droppo, I.G., Leppard, G.G., Liss, S.N., Milligan, T.G. (Eds.), Flocculation in Natural and Engineered Environmental Systems, Boca Raton, Florida, CRC Press, pp. 407-421.

Geyer, W.R., Hill, P.S., Kineke, G.C., 2004. The transport, transformation and dispersal of sediment by buoyant coastal flows, *Continental Shelf Research*, 24, 927-949.

Hill, P.S., Voulgaris, G., Trowbridge, J.H., 2001. Controls on floc size in a continental shelf bottom boundary layer, *Journal of Geophysical Research*, 106(C5), 9543-9549.

Menon, M., Gibbs, R., and Phillips A. 1998. Accumulation of muds and metals in the Hudson River Estuary turbidity maximum, *Environmental Geology*, 34, 212-222.

Sanford, L.P., Suttles S.E., Halka, J.P., 2001. Reconsidering the physics of the Chesapeake Bay estuarine turbidity maximum. *Estuaries*, 24, 655-669.

Winterwerp, J.C., 1998. A simple model for turbulence induced flocculation of cohesive sediment, *Journal of Hydraulic Research*, 36, 309-326.

Xu, F., Wang, D.P., Riemer, N., 2008. Modeling flocculation processes of fine-grained particles using a size-resolved method: Comparison with published laboratory experiments, *Continental Shelf Research*, 28, 2668-2677.

Chapter 2

Modeling flocculation processes of fine-grained particles using a size-resolved method: Comparison with published laboratory experiments

2.1 Introduction

Suspended fine-grained sediments (< 63 μm) in estuaries often exist in the form of flocs (Eisma et al., 1994). Flocs are capable of adsorbing organic carbon, nutrients and anthropogenic contaminants (Syvitski et al., 1995), thus, they play a key role in the transport of the suspended matter to the bottom. The main difficulties in predicting the fate and transport of the suspended matter are the spatial and temporal variations in the floc size and hence their settling velocity (Mikkelsen et al., 2005). The floc size can vary from a few micrometers to hundreds, even thousands of micrometers (Hill et al., 1998; Fugate and Friedrichs, 2003; Traykovski et al., 2004; Uncles et al., 2006). Typically, large flocs sink much faster than their component grains. The variations in floc size are primarily due to flocculation processes, such as aggregation and breakup. A better understanding of these processes is critical to predict the transport of fine-grained sediments.

Flocculation is affected by many factors, including suspended sediment concentration (SSC), turbulence-induced shear, differential settling of flocs and sticky organic matter in the water column (Dyer and Manning 1999; Geyer et al., 2004). The individual contribution of these factors to the floc size is unclear. The floc growth rate

appears to depend on SSC in a nonlinear way. Kranck and Milligan (1992) found that the floc size increases with increasing SSC. However, the floc size is not always positively correlated with SSC. For example, Hill et al. (2000) found that the floc size was uniform despite a wide variability in concentration. They suggested that highly turbid water might limit floc growth. Turbulence can increase particle collisions and form flocs; on the other hand, turbulent shear may tear large floc apart and limit maximal floc size under energetic conditions (Hunt, 1986). Under low-to-moderate energy environments, the floc size is possibly controlled by forces exerted on sinking flocs by the relative particle-fluid motion (Hill et al. 2001). Differential settling describes the process that large particles sink faster than smaller ones and may capture the small particles during settling. Sticky organic matter in the water column affects the particle stickiness, that is, the probability that two particles will adhere once they have collided. Stickiness has a large natural variability, ranging from $O(10^{-3})$ to $O(1)$ (Hill and Nowell, 1995).

The importance and complexity of particle aggregation have triggered numerous numerical modeling in various fields of the atmospheric sciences, environmental sciences and in engineering. Smoluchowski (1917) originally proposed a coagulation equation for particles colliding due to Brownian motion. After that other physical mechanisms, such as shear and differential settling, have been proposed to influence the particle size distribution (Pruppacher and Klett, 1980). Regarding the coagulation in open ocean environments, Farley and Morel (1986) numerically solved the coagulation equation for a single pulse input of colloidal particles (size < 1 μm) in a well-mixed (zero dimension) system by assuming spherical particles with constant density. Burd and Jackson (1997) updated the model of Farley and Morel (1986) by including effects of fractal structure

and hydrodynamic interaction. Their study shows that the fractal structure alters the floc density and settling velocity, and the simulation results are sensitive to the variations in fractal dimension. On the other hand, the hydrodynamic deflection of particles around each other does not have a significant impact.

Sediment transport models involving flocculation processes are few (Lavelle, 1993). A 'characteristic' settling velocity for flocs is commonly used for simulation of SSC profiles (e.g. Orton and Kineke, 2001; Warner et al., 2005). The merit of this approach is that only one parameter needs to be calibrated. Power law parameterizations are also widely used to describe variations in settling velocity with SSC. However, the parameters for the power law can vary considerably from site to site (Spearman and Roberts, 2002). Power law with dissipation parameter function, which includes the effect of increasing turbulence on floc breakup, was suggested by van Leussen (1994). A simple flocculation model incorporating turbulence-induced growth and breakup of flocs was proposed by Winterwerp (1998). The model estimates the equilibrium median floc size and applies a fractal treatment to modify the Stokes' law relating settling velocity to floc size. The flocculation model was implemented in a three-dimensional hydrodynamic model to simulate the turbidity maximum in the Ems estuary (Winterwerp, 2002). These model studies have clearly demonstrated the importance of including flocculation processes in sediment transport models.

The objective of this study is to develop a flocculation model which explicitly predicts the particle size and concentration distributions in estuarine and coastal environments. In section 2, we simulate flocculation processes using a size-resolved method which is mass-conserved and computationally efficient. The flocculation

simulation is compared with published laboratory observations. Both aggregation and breakup processes are included, considering the effects of turbulent shear. The breakup kernel calculation accounts for the fractal dimension of the flocs. Sensitivity tests are performed to inspect the influence of fractal dimension and particle stickiness. Section 3 presents a one-dimensional (1-D) sediment transport model and the comparison of the simulation results with laboratory observations published in the current literature. We also explore the sensitivity of the model towards model parameters like the parameterizations of settling velocity and erosion rate. Section 4 concludes our findings.

2.2 Flocculation

Our size-resolved method for understanding flocculation of sediment particles is based on the Smoluchowski framework. This framework considers mass conservation for particles in different size bins, which approximates the real size distribution of particles. For each bin, a balance equation for the mass density is solved. A basic form of the equation is (Hill and Nowell, 1995; Bott, 1998):

$$\frac{\partial n(m,t)}{\partial t} = \frac{1}{2}\int_{m_0}^{m} n(m_c,t)K(m_c,m')n(m',t)dm' - \int_{m_0}^{\infty} n(m,t)K(m,m')n(m',t)dm' + \int_{m_0}^{\infty} Q(m,m')P(m')n(m',t)dm' - n(m,t)P(m), \quad (1)$$

where $n(m,t)$ is the particle number density as a function of time t and mass m, m_0 is the mass of particle in the first bin, $K(m_c,m')$ is the aggregation kernel describing the rate of particle contacts ($m_c = m\text{-}m'$), $P(m)$ is the breakup kernel due to turbulent shear, and $Q(m,m')$ represents the number density function for the fragments formed by the breakup of a parent particle of mass m'. The integrals on the right hand side of Equation (1) represent: the gain rate of particles of mass m by collision of two smaller particles; the loss of particles with mass m due to collision with other particles; the number increase of

particles with mass m from breakup of larger flocs; and the loss of particles with mass m due to breakup.

Theoretical and numerical investigations on floc breakup dynamics have been reported in the literature (Spicer and Pratsinis, 1996; Zhang and Li, 2003; Maggi, 2005), but experimental data are rare. Three distinct breakage distribution functions, binary, ternary and Gaussian distribution, were proposed by Spicer and Pratsinis (1996). Numerical experiments by Zhang and Li (2003) showed no significant differences in the results of the steady-state size distributions from the three breakage functions. The simplest binary breakup is used in the present study. $Q(m,m')$ is defined as (Zhang and Li, 2003):

$$Q(m,m') = \begin{cases} 2 & (m = m'/2) \\ 0 & (m \neq m'/2) \end{cases}. \tag{2}$$

The breakup kernel, P, is a function of shear rate and floc size. The flocs are considered to be composed of primary particles. Assuming a fractal treatment, the breakup frequency can be written as (Winterwerp, 1998):

$$P_i = E\sqrt{\frac{\mu}{F_y}}G^{1.5}(2r_i)\left(\frac{r_i - r_1}{r_1}\right)^{3-n_f}, \tag{3}$$

where μ is the dynamic viscosity, n_f is the fractal dimension, and $F_y \approx 10^{-10}$ Pa is the estimated yield strength. The fractal dimension of flocs is defined as (Winterwerp, 2002)

$$n_f = \lim_{L\to\infty}\frac{\ln(N(L))}{\ln(L)}, \tag{4}$$

where $N(L)$ is the number of self similar primary particles and L is the linear particle size. The typical value of n_f varies from about 1.4 for fragile flocs to about 2.2 for strong estuarine flocs (Winterwerp, 1998). n_f=2 is applied in calculating breakup kernel.

The aggregation is due to turbulent shear and differential settling. Brownian motion is neglected because it is only important when the particle size is less than 1 μm (*Winterwerp*, 2002). The concentration of particles of this size is negligible in estuaries. The rectilinear aggregation kernel is $K = \alpha(K_{ts} + K_{ds})$ (Burd and Jackson, 1997), where α is the particle stickiness, and the kernels K_{ts} and K_{ds} estimate the collision rate per unit volume caused by turbulence shear and differential settling (Hill et al., 2001). Specifically, the kernels K_{ts} and K_{ds} are given by:

$$K_{ts} = \frac{4}{3} G(r_i + r_j)^3 , \tag{5}$$

and

$$K_{ds} = \pi \cdot (r_i + r_j)^2 \cdot \left| w_{s,i} - w_{s,j} \right| , \tag{6}$$

where r_i and r_j are the floc radius, $w_{s,i}$ and $w_{s,j}$ are the settling velocity of flocs in bin i and j. The shear rate is defined as $G = \sqrt{\varepsilon / \nu}$, where ε is the turbulent dissipation rate and ν is the kinematic viscosity of fluid. The settling velocity is calculated as a function of particle size from Sternberg et al. (1999),

$$w_{s,j} = 347.5602(2r_j)^{1.54} , \tag{7}$$

where r_j is in m, and $w_{s,j}$ is in m s^{-1}. Equation (7) is an empirical relationship obtained by the regression between measured size and settling velocity of suspended flocs. It incorporates the effects of variable floc densities due to the fractal structure. Substituting Equation (7) into the Stokes' Law, the floc effective density $\Delta\rho = \rho_{floc} - \rho_{water}$ can be estimated as a function of floc size, i.e. $\Delta\rho \propto D^{-0.46}$. Sternberg et al. (1999) found their results comparable with several other measurements with the exponent between $\Delta\rho$ and

floc size varying from -1.40 to -0.46. The effect of fractal structure of flocs is implicitly included in Equation (7). The differential settling kernel (Equation 6) is further multiplied by a factor of 5 to include the fact that irregular floc shapes can increase the efficiency of floc contacts. The empirical factor 5 is selected, which best fits the lab flume experiment.

For the numerical solution of Equation (1) we use the flux method by Bott (1998), which has been successfully used in predicting the coagulation of cloud droplets (Riemer and Wexler, 2005). We introduce the mass density function *g(y,t)* by

$$g(y,t)dy = mn(m,t)dm, \qquad n(m,t) = \frac{1}{3m^2} g(y,t), \tag{8}$$

where $y = \ln r$ and *r* is the radius of flocs with mass *m*. When Equation (8) is substituted into Equation (1), a balance equation for the mass density is obtained:

$$\begin{aligned} \frac{\partial g(y,t)}{\partial t} = {} & \frac{1}{2}\int_{y_0}^{y} \frac{m^2}{m_c^2 m'} g(y_c,t)K(y_c,y')g(y',t)dy' - \int_{y_0}^{\infty} \frac{1}{m'} g(y,t)K(y,y')g(y',t)dy' \\ & + \int_{y_0}^{\infty} \frac{m}{m'} Q(y,y')P(y')g(y',t)dy' - \frac{1}{3m^2} g(y,t)P(y). \end{aligned} \tag{9}$$

To solve Equation (9) numerically, we use a logarithmically equidistant mass grid,

$$m_{k+1} = \beta m_k, \qquad k = 1,\ldots,n, \tag{10}$$

where β is an arbitrary number ($\beta > 1$) and *n* is the total number of bins for particle size spectrum. Thus, the *y* grid is equally spaced, $\Delta y_k = \ln r_{k+1} - \ln r_k = \ln \beta / 3$. Typically, β is set to be $2^{1/x}$ with *x* is an integer. This yields a doubling of the particle mass after *x* bins. It has been shown that the increasing value of *x* decelerates the evolution of the floc spectrum (Bott, 1998). To achieve a reasonable compromise between numerical accuracy and efficiency, $\beta = 2^{1/4}$ is applied in the study.

As a result of the discretization, the collision of floc of mass m_i with floc of mass m_j will produce a new floc whose mass $m' = m_i + m_j$ which in general falls between m_k and m_{k+1}. To conserve particle mass a two-step procedure is used. In the first step, the newly formed floc with mass m' is added to grid box k. In the second step, an advection equation is solved to move a certain fraction, proportional to $(m' - m_k)/(m_{k+1} - m_k)$, of the floc mass from grid k to k+1. A higher-order positive definite advection scheme (Bott, 1989) is used to prevent numerical diffusion. A detailed description of the numerical implementation of the flocculation model is given in the Appendix of this Chapter.

Winterwerp (1998) performed a settling column lab experiment to measure floc size variations with turbulent shear and SSC. Initially, a certain amount of particles with primary particle size (D_p = 4 μm) is placed into a cylinder where a homogenous turbulence field is generated through an oscillating grid. The particles are initially homogeneously mixed, and measurements are taken at the bottom when the system reaches equilibrium. Three test cases (T71, T69, and T73) with experimental parameters and results are listed in Table 1.

We carry out a flocculation simulation to verify the size-resolved method described above. Our simulation applies the same initial concentrations, shear rates, and primary particle size as in the experiments. Effects of differential settling on the aggregation rate are not considered, i.e. $K_{ds} = 0$.

We run the simulation until the floc size distribution reaches a dynamic steady state. The variations in median floc size (D_{50}) with time and the floc size distribution at steady state for the three tests are shown in Fig. 1. The floc size distributions at steady state (the lower panel of Fig. 1) show $D_{25} - D_{75} \approx 0.5 D_{50}$, where D_{25} and D_{75} are the

upper and lower quartile of floc size by mass. The median floc sizes are about 209, 199, and 157 μm at steady state, and the flocculation time scales (T_f), defined as the time scale for 95% of particles to reach their equilibrium values (Winterwerp, 2002), are about 6000, 900 and 200 seconds for test T71, T69 and T73, respectively. The model results are comparable with the experimental values (see Table 1 and Fig. 4 in Winterwerp (1998)).

Fig. 2 shows temporal evolution of the floc size distribution for the test case T69. At the beginning of the simulation, aggregation dominates and quickly shifts the flocs towards larger sizes. As the flocs become larger and more fragile, breakup becomes more important and starts to decelerate the growth of flocs. Finally, equilibrium between aggregation and breakup and a steady state of the particle size distribution is achieved. We note that the wiggles in the small floc size at t =300 s in Fig. 2 are caused by the simulation starting with all particles in the first bin. At t=300 s the simulation has not reached a steady state and there are some primary particles and small flocs left. We have conducted another simulation with an initial log–normal distribution of flocs, and the wiggles are eliminated (not shown).

To test the sensitivity of the model towards fractal dimension and particle stickiness, two sets of numerical experiments were done. For the first set, the fractal dimension (n_f) in the expression for the breakup frequency varies from 1.8 to 2.2, with the other settings the same as in the base case. The resulting median floc sizes are listed in Table 2 and show that the floc size increases as fractal dimension increases. The reason is that the increase of n_f reduces the breakup frequency (Equation (3)), and allows the formation of larger flocs.

For the second set, the particle stickiness α is taken as 0.05, 0.1, 0.2, 0.4, and 1.0 with the other settings identical to the base case. Table 3 shows the results for the median floc size for different α values. The floc size generally increases with increased α. $D_{50} \propto \alpha^{0.5}$ is found using unconstrained nonlinear optimization (γ^2=0.93). Also, as α decreases, the flocculation time scale increases due to the longer time required to reach equilibrium.

Winterwerp (1998) proposed a relationship for the median floc size,

$$D_{50} = D_p + \frac{k_A C_0}{k_B \sqrt{G}}, \tag{11}$$

where k_A and k_B are aggregation and breakup coefficients, respectively, determined from fitting the experiment results, and C_0 is the total suspended sediment concentration. To evaluate this relationship with our model results, five additional model runs are completed with different values for $C_0/\sqrt{G}$ to increase the data range. Excellent regression (γ = 0.99) is obtained (Fig. 3). However, in our regression fit, the constant (D_p) is about 1×10^{-4} m, and the slope is about 4×10^{-4} m^4 kg^{-1} $s^{-0.5}$. From Winterwerp (1998), D_p is about 4×10^{-6} m, and the slope is about 1×10^{-3} m^4 kg^{-1} $s^{-0.5}$. In our simulation the particle size distributions are slightly skewed to the right (lower panel in Fig. 1). Thus the D_{50} is larger than the floc size in one-floc approach in Winterwerp (1998) that assumes symmetrical distribution.

2.3 A one-dimensional (1-D) sediment transport model

In the following section we investigate the interplay of flocculation processes with vertical transport. The governing equation for this 1-D simulation is

$$\frac{\partial g(y,t)}{\partial t} - \frac{\partial w_{s,j} g(y,t)}{\partial z} = \frac{\partial}{\partial z}\left(K_3 \frac{\partial g(y,t)}{\partial z} \right) + flocculation, \qquad (12)$$

where z is the vertical dimension and K_3 is the vertical eddy diffusivity. Equation (12) describes the change in the mass density distribution due to vertical transport and flocculation. Settling, turbulent diffusion and flocculation are considered, while vertical advection is ignored (small compared to settling). The flocculation term is as in Equation (9). The eddy viscosity/diffusivity follows the Prandtl mixing-length theory, and the Prandtl Schmidt number is assumed to be unity. The diffusivity K_3 and turbulent dissipation rate ε are calculated (Orton and Kineke, 2001; Hill and McCave, 2001):

$$K_3 = \kappa u_* z(1 - z/H), \text{ and } \varepsilon = u_*^3 / \kappa z, \qquad (13)$$

where κ is von Kármán's constant (κ=0.4), and u_* is the friction velocity. The settling velocity $w_{s,j}$ is calculated from Equation (7). The bottom erosion mass flux $E_{s,i}$ of particle in bin i is modified from Warner et al. (2005),

$$K_3 \left. \frac{\partial g_i}{\partial z} \right|_{bottom} = E_{s,i} = E_0 (\frac{\tau_b}{\tau_c} - 1)/i, \quad \text{when} \quad \tau_b > \tau_c \qquad (14)$$

where E_0 is a bed erodibility constant. The bed shear stress $\tau_b = \rho u_*^2$, where ρ is the fluid density, 1010 kg m^{-3}. τ_c is the critical shear stress for erosion and is set to 0.12 pa in the study (Righetti and Lucarelli, 2007). The constant E_0 = 0.001 kg m^{-2} s^{-1} is used (Ariathurai and Arulanandan, 1977). Equation (14) is an empirical approach to account for the fact that larger particles are more difficult to erode than smaller ones. This is accounted for by the bin number i in the denominator. Equation (12) is solved in two steps. First, the mass density function ($g(y,t)$) is updated at each vertical grid point via

flocculation. Next, sedimentation and turbulent diffusion terms are applied on the vertical distribution of flocs of each bin.

The 1-D simulation results are compared with the observed size distribution over tidal cycles in a laboratory flume experiment of Bale et al. (2002). In the flume, oscillating currents are generated via a stirring plate. The current velocities range from 0.05 m s^{-1} to 0.45 m s^{-1} over a period of 2 hours, i.e., a full tidal cycle is 4 hours. SSC and the particle sizes are measured. The experimental results show that SSC and median particle size vary periodically over the tidal cycles. Sediment erosion occurs when a critical velocity is exceeded. SSC increases quickly before the entire sediments are resuspended into the water column. The median size of particles is smallest near the minimum velocity, increases with erosion, but then decreases with the increasing of current velocity. As the velocity decreases, the median size of particles increases again, and SSC starts to decrease due to deposition.

We carry out model simulations of the flume experiment. The same parameters are used in both the simulation and experiment. The water column is 0.28 m deep, the initial SSC is 3520 mg l^{-1}, the primary particle size is 30 μm, and the density of the primary particles is 2650 kg m^{-3}. The lab experiments were carried out for different salinity, but the results are not sensitive. Our model simulation corresponds to salinity of 0.2 psu. We use 70 size bins to represent the particle size distribution, ranging from 30 to 1562 μm. The particle stickiness is 1.0. The sediment effects on water density are ignored due to low SSC. Friction velocity is set to be sinusoidal cycles with a period of 4 hours.

The simulation is integrated for 3 tidal cycles. Fig. 4 shows the contours of the floc median size in the water column during the last two tidal cycles. Typically, the floc

size is smaller near the bottom due to the high turbulent level and dominant breakup process near the bottom. Fig. 5 compares the variations in floc size and SSC over the tidal cycles at the height of 0.1 mab (meter above bottom) between model simulation and lab experiment; the half hourly lab data are interpolated from Fig. 2 of Bale et al. (2002). The results of the model simulation are in good agreement with the experiment. The floc size is small during peak tidal currents even though SSC is high, due to the dominant breakup process caused by high turbulent shear. The floc size then starts to increase as tidal currents decrease, and reaches its maximum near slack tides due to dominant aggregation. After that, the floc size decreases rapidly due to preferential settling of large flocs coincident with an abrupt decrease of SSC. The floc size and SSC increase again when erosion occurs with the increased tidal currents.

The individual contributions to the temporal change of the floc mass density distribution ($\partial g/\partial t$) at hour 4.5 and 5.5 at 0.1 mab are separated to evaluate the effects of aggregation, breakup, diffusion, sedimentation, erosion and deposition on floc size variations (Fig. 6). The SSC is lower at hour 5.5 (Fig. 5), and hence, the magnitudes of $\partial g/\partial t$ are smaller at hour 5.5 than at hour 4.5. Fig. 6a shows that aggregation moves the mass from smaller sizes to larger sizes, while breakup has the opposite effect. The net effect of aggregation and breakup is shown in Fig. 6b. Production of large flocs (D>100 μm) and depletion of small flocs (D<100 μm) are observed at hour 4.5. As the aggregation proceeds, the maximum of the floc growth rate moves towards larger sizes as seen at hour 5.5. $\partial g/\partial t$ due to diffusion and sedimentation are shown in Fig. 6c. At hour 4.5, the mass of small flocs (D<100 μm) increases due to a dominant upward diffusive flux, while the mass of large flocs (100<D<200 μm) decreases due to a downward

diffusive flux. At 0.1 mab, sedimentation contributes to the increase of large flocs (D>150 μm). Thus, both diffusion and sedimentation contribute to the transport of large flocs towards the bottom where floc growth is mainly controlled by breakup processes. The simulation supports the hypothesis that the floc size throughout the water column can be limited by near-bed turbulence (Hill et al., 2001). The sum of the temporal changes by the above four processes indicates that the overall floc size increases at hour 4.5, but decreases at hour 5.5 (Fig. 6d). Erosion only occurs when the critical shear stress is reached. At hour 4.5, erosion and deposition rate balance each other at the bottom (Fig. 6e). At hour 5.5, the deposition rate increases because particles are mostly in the form of large flocs with high settling velocity.

The deposition rate describes the reduction of SSC throughout the water column with time. It is calculated in the lab experiment by fitting the observed concentration decline with time to an exponential function. In the laboratory experiment a deposition rate of 17.12 g m^{-2} min^{-1} is obtained for an initial SSC of 3780 mg l^{-1} (Table 1 in Bale et al. (2002). The deposition rate calculated from the simulation is 19.47 g m^{-2} min^{-1} using $\frac{d}{dt}\int cdz$ where c is local SSC and the integration is through the entire water column during the period when the total concentration decreases, e.g. from hour 5.5 to hour 6. Another simulation with initial SSC of 830 mg l^{-1} is performed for further comparison. The calculated deposition rate is 4.46 g m^{-2} min^{-1}, which compares well with the experimental value of 3.31 g m^{-2} min^{-1} (see Table 1 in Bale et al. (2002)). These comparisons reinforce the model's fidelity in simulating particle size and SSC variations.

The simulation has shown that the floc size distribution changes depending on SSC and turbulent shear conditions. The relationship between median floc size, SSC and

G can be explored (Fig. 7). In the previous study, we found that D_{50} is proportional to $C_0/\sqrt{G}$. For a regression fit for D_{50} and $C_0/\sqrt{G}$ of 1-D study we obtain a correlation coefficient $\gamma^2 = 0.52$. The decrease in correlation may be due to the 1-D floc sizes not being in equilibrium; hence Equation (11) is not valid. A much better regression, on the other hand, is obtained between D_{50} and C_0/G ($\gamma^2 = 0.90$), suggesting that the effect of turbulent diffusion is more important. Since $G = \sqrt{\varepsilon/\nu} = \nu/\lambda_0^2$, where λ_0 is the Kolmogorov microscale of turbulence, the inverse relationship between D_{50} and G is consistent with the observations that floc size is characterized by the Kolmogorov microscale (Fugate and Friedrichs, 2003).

A one-size simulation/simulation without size-resolved flocculation is carried out to highlight the effects of rapid flocculation on sediment transport. For this simulation we need to specify the floc size, which is kept constant throughout the whole simulation. To create conditions that are comparable to the simulation with size-resolved flocculation we use the tidally-averaged floc size of 138 μm. For a fair comparison of the simulations with or without size-resolved flocculation, we also change back the bottom erosion flux to its original form,

$$E_{s,i} = E_0\left(\frac{\tau_b}{\tau_c} - 1\right), \quad \text{when} \quad \tau_b > \tau_c . \tag{15}$$

where E_0=5×10^{-5} kg m^{-2} s^{-1} and τ_c=0.05 Pa (Warner et al. 2005). Fig. 8 shows variations in SSC with tidal currents at 0.1 mab. The maximum SSC is about 3520 mg l^{-1} during high tidal currents, and the minimum SSC is about 250 mg l^{-1} near slack tides. The timing difference between maximum current and SSC is due to the settling lag of particles (Friedrich et al., 1998; Cheng, 2007). In both cases, all particles are eroded into the water

column during maximum currents, hence, similar maximum SSCs are expected in the simulations with and without size-resolved flocculation. Also, the constant floc size, 138 μm, is chosen to be the same as the averaged floc size from the case with flocculation. Thus, the same minimum SSCs are expected as both have the same averaged settling velocity. Simulation tests with a larger or smaller floc size cannot produce the expected SSC distribution. Hence, without the 'right' floc size, the simulation without size-resolved flocculation will not produce the correct SSC. For these two scenarios (with and without size-resolved flocculation) the difference comes from the variations in the settling velocity. Without size-resolved flocculation the deposition rate during the time when the SSC declines sharply is only about 50% of that for the simulation with flocculation (Note the much sharper drop in SSC in the simulation with flocculation, Fig. 8.). With flocculation the floc size increases sharply as the currents decrease, whereas without size-resolved flocculation the particle size remains the same.

Two sensitivity studies are performed to explore the effects of settling velocity and erosion rate on the floc size distribution and SSC. In the first numerical experiment, the settling velocity parameterization from Equation (7) is replaced by a modified Stokes' law (Winterwerp, 2002),

$$w_{s,j} = \frac{2(\rho_s - \rho_w)g}{9\mu} \cdot r_1 r_j \qquad (16)$$

where ρ_s and ρ_w are the densities of the primary particles and fluid, μ is dynamic viscosity of the fluid, 0.001 Pa S, and r_1 is the radius of primary particles. The results are similar to the base case, except that the maximum median floc size is slightly smaller, 160 μm versus 190 μm in the base case (not shown). For floc sizes < 400 μm the settling velocity from Equation (16) is larger than that from Equation (7) (Fig. 9). The larger

settling velocity contributes to a faster sinking of the flocs. As a result, the maximum floc size becomes smaller. Also, SSC is near zero near slack tides.

In the second experiment, the bottom erosion flux is changed to Equation (15). All other settings are the same as in the base case. The variation patterns of the median floc size and SSC are qualitatively similar to the base case (Fig. 10). However, the maximum median floc size is much larger ~ 270 μm, due to the increase in erosion flux of the larger particles. Also, the secondary peak of the median floc size becomes more pronounced.

2.4 Discussions

We have developed a size-resolved flocculation model to simulate the variations in floc size and SSC distributions. The size-resolved model is evaluated with published laboratory measurements. The flocculation simulation results are comparable with Winterwerp (1998). Varying the particle stickiness indicates that the median diameter and stickiness are related by $D_{50} \propto \alpha^{0.5}$. Floc size variations over tidal cycles are simulated in the 1-D study in which sedimentation, diffusion, deposition and erosion are considered besides flocculation. The results are in good agreement with Bale et al. (2002). Analysis of the temporal changes of the floc mass density distribution shows the interplay of particle flocculation and vertical transport. The high turbulence intensity during the peak currents limits the maximum floc size. Diffusion and sedimentation influence the distribution of suspended particles in the water column. Large flocs are moved to the bottom and destroyed by intense near-bed turbulence. The competition between erosion and deposition controls the SSC. The study clearly demonstrates the need to include transport and flocculation simultaneously for sediment simulation.

The sensitivity test suggests that the floc formation is sensitive to the erosion flux and the availability of bottom sediments. Since most previous erosion model studies have dealt with a single particle size, it is not clear whether our simple generalization to a size-dependent erosion flux (Equation 14) is adequate in real world applications. The settling velocity formulation, on the other hand, does not appear to have significant effect for the floc size range considered in this study. For large aggregates (D>500 μm) different settling velocity formulation could become critical.

In a study of the turbidity maximum in the upper reaches of the Tamar estuary, UK, Bass et al. (2007) and Manning et al. (2007) found that over a tidal cycle the maximum floc size was over 600 μm at SSC=4.2 kg m^{-3} and $\tau_b = 0.38$ Pa, and decreased to about 220 μm at SSC= 0.04 kg m^{-3} and $\tau_b = 0.01$ Pa. The corresponding median floc size was about 380 μm and 150 μm (see Fig. 5 and Fig. 7 of Manning et al. (2007)). Using the regression relationship (lower panel of Fig. 7) derived from our model simulations, we obtain the median floc size of 393 and 143 μm, respectively. Considering the large temporal variations of the median floc size, the excellent agreement with field observations is probably fortuitous.

The sediment transport modeling results are generally consistent with the observations of floc size in estuaries. Traykovski et al. (2004) described the suspended sediment size distribution at 1.5 mab over eight tidal cycles in the Hudson Estuary. On both flood and ebb tides, the particle size was small with means around 40 μm during maximum currents, but became significantly larger with means around 250 μm as currents decreased. Measurements of floc size in the turbidity maximum of the Ouse Estuary, UK, showed that near mid-depth the median floc size was about 500 μm at high

water slack, but decreased to about 100 μm on the ebb and about 70 μm on the flood (Uncles et al., 2006). Estimates of floc size from the estimates of settling velocity in the York River Estuary suggested that the floc size was limited by the Kolmogorov microscale under peak tidal currents (Scully and Friedrichs, 2007). In the 1-D simulation, the floc size variation shows qualitatively the same temporal patterns with tidal currents as the observations. The size range, which depends on local tidal currents and total SSC, is different from the observations.

Appendix A. Description of the size-resolved flocculation model

The flocculation model solves two processes, aggregation and breakup.

A.1. Aggregation processes

For the treatment of the aggregation processes, we use the method by Bott (1998). The particle mass density function *g(y,t)* is the prognostic variable. In discretized form, a change in the mass distributions g_i and g_j is calculated by the aggregation of flocs with mass m_i with flocs of mass m_j.

$$g_i(i,j) = g_i - g_i \frac{K(i,j)}{m_j} g_j \Delta y \Delta t, \qquad \text{(A1)}$$

$$g_j(i,j) = g_j - g_j \frac{K(i,j)}{m_i} g_i \Delta y \Delta t, \qquad \text{(A2)}$$

where g_i and g_j are the mass distribution functions at bin *i* and *j* before aggregation while $g_i(i,j)$ and $g_j(i,j)$ are the new mass distributions after aggregation. New flocs with mass m' ($m' = m_i + m_j$) are produced by aggregation of smaller flocs in bin *i* and *j*. The new mass distribution is the sum of the second term on the right hand side of (A1) and (A2):

$$g'(i,j) = \frac{m'(i,j)}{m_i m_j} g_i K(i,j) g_j \Delta y \Delta t. \qquad \text{(A3)}$$

However, usually the newly-formed m' is not fit in the pre-defined mass bins (Equation 10), and

$$m_k \le m' \le m_{k+1}. \qquad \text{(A4)}$$

Then the mass density $g'(i,j)$ has to be split into bin k and k+1. A two-step procedure is applied to accomplish the partitioning. First, all $g'(i,j)$ is added to bin k and yields

$$g'_k(i,j) = g_k + g'(i,j). \qquad \text{(A5)}$$

Second, a certain fraction of the new mass $g'(i,j)$ is moved to bin k+1. The distribution can be expressed as

$$\begin{aligned} g_k(i,j) &= g'_k(i,j) - f_{k+1/2}(i,j) \\ g_{k+1}(i,j) &= g_{k+1} + f_{k+1/2}(i,j). \end{aligned} \qquad \text{(A6)}$$

$f_{k+1/2}(i,j)$ is the mass transported from bin k to k+1. A upstream scheme called upstream flux method (UFM) in Bott (1998) is used to calculate $f_{k+1/2}(i,j)$,

$$f_{k+1/2}(i,j) = c_k g'(i,j), \qquad \text{(A7)}$$

where c_k is defined as

$$c_k = \frac{\ln(m'(i,j)/m_k)}{3\Delta y_k}. \qquad \text{(A8)}$$

Note that $3\Delta y = 3(\ln\beta/3) = \ln\beta = \ln(m_{k+1}/m_k)$. Hence if c_k is about 1, all new flocs go into bin k+1, otherwise only a percentage of new flocs is moved to bin k+1.

A.2. Breakup processes

In discretized form, the floc mass distributions due to breakup is updated by

$$g'_i = g_i - P_i g_i \Delta t$$
$$g'_j = g_j + P_i g_i \Delta t \qquad \text{(A9)}$$

where g'_i and g'_j are the floc mass density functions in bin *i* and *j* after breakup, and P_i is the breakup kernel defined in Equation (3). We assume one large floc is broken up into two flocs with equal mass. According to Equation (10) and $\beta = 2^{1/x}$, floc mass is doubling after every *x* bins. Thus the mass of broken-up flocs, is moved to bin *j*=*i*-*x*. The breakup procedure starts from flocs in bin $i = x + 1$. The mass is transported to bin 1. In the next step, the broken flocs in bin $i = x + 2$ is moved to bin *2*. The calculation is continued until the breakup of the largest flocs.

References

Ariathurai, C.R., Arulanandan, K., 1978. Erosion rates of cohesive soils, *Journal of the Hydraulics Division*, ASCE 104(2), 279-282.

Bale, A.J., Uncles, R.J., Widdows, J., Brinsley, M.D., Barrett, C.D., 2002. Direct observation of the formation and break-up of aggregates in an annular flume using laser reflectance particle sizing, in Winterwerp, J.C., Kranenburg C. (Eds.), Fine Sediment Dynamics in the Marine Environment, Elsevier, pp. 189-201.

Bass, S.J., Manning, A.J., Dyer, K.R., 2007. Preliminary findings of a study of the upper reaches of the Tamar Estuary, UK, throughout a complete tidal cycle: Part I: Linking hydrodynamic and sediment cycles, in Maa, J.P.-Y., Sanford, L.P., Schoellhamer, D.H. (Eds.), Estuarine and Coastal Fine Sediments Dynamics-proceedings in Marine Science, vol. 8, Elsevier, Amsterdam, pp. 1-14.

Bott, A., 1989. A positive definite advection scheme obtained by nonlinear renormalization of the advection fluxes, *Monthly Weather Review*, 117, 1006-1015.

Bott, A., 1998. A flux method for the numerical solution of the stochastic collection equation, *Journal of Atmospheric Sciences*, 55, 2284-2293.

Burd, A., Jackson, G.A., 1997. Predicting particle coagulation and sedimentation rates for a pulsed input, *Journal of Geophysical Research*, 102(C5), 10,545-10,561.

Cheng, P., 2007. Modeling sediment transport in estuarine environment: effects of tidal asymmetry, lateral circulation and sediment-induced stratification, Ph.D. Thesis, Stony Brook University, USA.

Dyer, K.R., Manning, A.J., 1999. Observation of the size, settling velocity and effective density of flocs, and their fractal dimensions, *Journal of Sea Research*, 41, 87-95.

Eisma, D., Chen, S., Li, A., 1994. Tidal variations in suspended matter floc size in the Elbe river and Dollard estuaries, *Netherlands Journal of Aquatic Ecology*, 28, 267-274.

Farley, K.J., Morel, F.M.M., 1986. Role of coagulation in the kinetics of sedimentation, *Environmental Science and Technology*, 20, 187-195.

Friedrichs, C.T., Armbrust, B.D., de Swart, H.E., 1998. Hydrodynamics and equilibrium sediment dynamics of shallow, funnel-shaped tidal estuaries, in Dronkers, J., Scheffers M. (Eds.), Physics of Estuaries and Coastal Seas, Balkema, Amsterdam, pp. 315-327.

Friedrichs, C.T., Wright, L.D., Hepworth, D.A., Kim, S.C., 2000. Bottom-boundary-layer processes associated with fine sediment accumulation in coastal seas and bays, *Continental Shelf Research*, 20, 807-841.

Fugate, D.C., Friedrichs, C.T., 2003. Controls on suspended aggregate size in partially mixed estuaries, *Estuarine, Coastal and Shelf Science*, 58, 389-404.

Geyer, W.R., Hill, P.S., Kineke, G.C., 2004. The transport, transformation and dispersal of sediment by buoyant coastal flows, *Continental Shelf Research*, 24, 927-949.

Hill, P.S., McCave, I.N., 2001. Suspended particle transport in benthic boundary layers, in: Boudreau, B.P., Jorgensen, B.B. (Eds.), The Benthic Boundary Layer: Transport Processes and Biogeochemistry. Oxford University Press, Oxford, pp. 78-103.

Hill, P.S., Nowell, A.R.M., 1995. Comparison of two models of aggregation in continental-shelf bottom boundary layers, *Jouranl of Geophysical Research*, 100(C11), 22,749-22,763.

Hill, P.S., Syvitski, J.P., Cowan, E.A., Powell, R.D., 1998. In situ observations of floc settling velocities in Glacier Bay, Alaska, *Marine Geology*, 145, 85-94.

Hill, P.S., Milligan, T.G., Geyer, W.R., 2000. Controls on effective settling velocity in the Eel River flood plume, *Continental Shelf Research*, 20, 2095-2111.

Hill, P.S., Voulgaris, G., Trowbridge, J.H., 2001. Controls on floc size in a continental shelf bottom boundary layer, *Journal of Geophysical Research*, 106(C5), 9543-9549.

Hunt, J.R. 1986. Particle aggregate breakup by fluid shear, in Mehta A.J. (Eds.), Estuarine Cohesive Sediment Dynamics, Springer, Berlin, pp. 85-109.

Kranck, K., Milligan, T.G., 1992. Characteristics of suspended particles at an 11-hour anchor station in San Francisco Bay, California, *Journal of Geophysical Research*, 97, 11,373-11,382.

Lavelle, J.W., 1993. A model for estuarine sedimentation involving marine snow, in Mehta, A.J. (Eds.), Nearshore and Estuarine Cohesive Sediment Transport, Washington, D.C., USA, pp. 148-166.

van Leussen, W., 1994, Estuarine macroflocs and their role in fine-grained sediment transport, Ph.D. Thesis, University of Utrecht, Netherlands.

Maggi, F., 2005. Flocculation dynamics of cohesive sediment, Ph.D. Thesis, Delft University of Technology, Netherlands.

Manning, A.J., Bass, S.J., Dyer, K.R., 2007. Preliminary findings of a study of the upper reaches of the Tamar Estuary, UK, throughout a complete tidal cycle: Part II: *In-situ* floc spectra observations, in Maa, J.P.-Y., Sanford, L.P., Schoellhamer, D.H. (Eds.), Estuarine and Coastal Fine Sediments Dynamics-proceedings in Marine Science, vol. 8, Elsevier, Amsterdam, pp. 15-33.

Mikkelsen, O.A., Hill, P.S., Milligan, T.G., Chant, R.J., 2005. In situ particle size distributions and volume concentrations from a LISST-100 laser particle sizer and a digital floc camera, *Continental Shelf Research*, 25, 1959-1978.

Riemer, N., Wexler, A., 2005. Droplets to drops by turbulent coagulation, *Journal of Atmospheric Sciences*, 62, 1962–1975, 2005.

Orton, P.M., Kineke, G.C., 2001. Comparing calculated and observed vertical suspended-sediment distributions from a Hudson River Estuary turbidity maximum, *Estuarine, Coastal and Shelf Science*, 52, 401-410.

Righetti, M., Lucarelli, C., 2007. May the shields theory be extended to cohesive and adhesive benthic sediments? *Journal of Geophysical Research*, 112, C05039, doi:10.1029/2006JC003669.

Spicer P.T., Pratsinis, S.E., 1996. Coagulation and fragmentation: Universal steady-state particle-size distribution. *American Institute of Chemical Engineers,* 42(6), 612-620.

Scully, M.E., Friedrichs, C.T., 2007. Sediment pumping by tidal asymmetry in a partially mixed estuary, *Journal of Geophysical Research*, 112, C07028, doi: 10.1029/2006JC003784.

Smoluchowski, M. 1917. Versuch einer mathematischen Theorie der Koagulationskinetik kolloider Lősunger, *Zeitschrift fur Physikalische Chemie*, 92, 129-168.

Spearman, J.R., Roberts, W., 2002. Comparison of flocculation models for applied sediment transport modeling, in Winterwerp J.C., Kranenburg, C. (Eds.), Fine Sediment Dynamics in the Marine Environment*,* Elsevier, pp. 277-293.

Sternberg, R.W., Berhane, I., Ogston, A.S., 1999. Measurement of size and settling velocity of suspended aggregates on the northern California continental shelf, *Marine Geology*, 154, 43-53.

Syvitski, J.P.M., Asprey, K.W., Le Blanc, K.W.G., 1995. In-situ characteristics of particles settling within a deep-water estuary, *Deep Sea Research II*, 42, 223-256.

Traykovski, P., Geyer, W.R., Sommerfield, C., 2004. Rapid sediment deposition and fine-scale strata formation in the Hudson estuary, *Journal of Geophysical Research*, 109, F02004, doi:10.1029/2003JF000096.

Uncles, R.J., Stephens, J.A., Law, D.J., 2006. Turbidity maximum in the macrotidal, highly turbid Humber Estuary, UK: Flocs, fluid mud, stationary suspensions and tidal bores, *Estuarine, Coastal and Shelf Science*, 67, 30-52.

Warner, J. C., Sherwood, C. R., Arango, H.G., Signell, R.P., 2005. Performance of four turbulence closure models implemented using a generic length scale method, *Ocean Modeling*, 8, 81-113.

Winter, C., Katoshevski, D., Bartholomä, A., Flemming, B.W., 2007. Grouping dynamics of suspended matter in tidal channels, *Journal of Geophysical Research*, 112, C08010, doi: 10.1029/2005JC003423.

Winterwerp, J.C., 1998. A simple model for turbulence induced flocculation of cohesive sediment, *Journal of Hydraulic Research*, 36, 309-326.

Winterwerp, J.C., 2002. On the flocculation and settling velocity of estuarine mud, *Continental Shelf Research*, 22, 1339-1360.

Zhang, J.J., Li, X.Y., 2003. Modeling particle-size distribution dynamics in a flocculation system, *American Institute of Chemical Engineers*, 49, 1870-1882.

Table 1 Parameters and results in the three test cases (adopted from *Winterwerp* (1998)). C_0 is the total mass concentration, G is the shear rate, and D_{50} is median particle size at equilibrium.

Test No.	C_0 (g l^{-1})	G (s^{-1})	D_{50} (μm)
T71	0.65	7.3	270
T69	1.17	28.9	241
T73	1.21	81.7	140

Table 2 The median floc size (μm) under different fractal dimension (n_f) simulations.

Test No.	n_f=1.8	n_f=1.9	n_f=2.0	n_f=2.1	n_f=2.2
T71	145	172	209	256	322
T69	139	165	199	245	307
T73	112	132	157	190	236

Table 3 The median floc size (μm) under different particle stickiness (α) simulations.

Test No.	α = 0.05	α = 0.1	α = 0.2	α = 0.4	α = 0.7	α = 1.0
T71	56	80	113	158	209	249
T69	55	76	107	151	199	238
T73	43	60	85	119	157	187

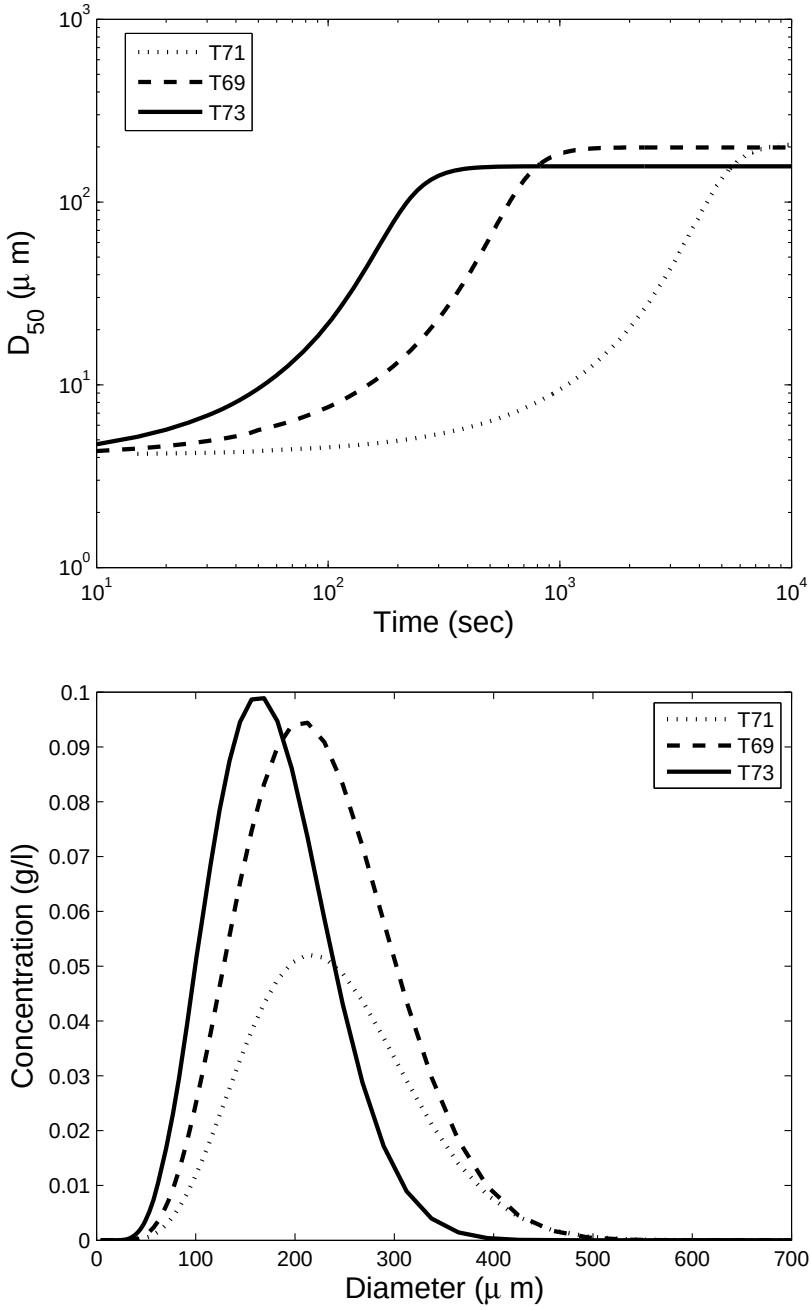

Figure 1 Variations of median floc size (D_{50}) with time (upper panel), and floc size distributions at steady state (lower panel) for three test cases of flocculation simulation.

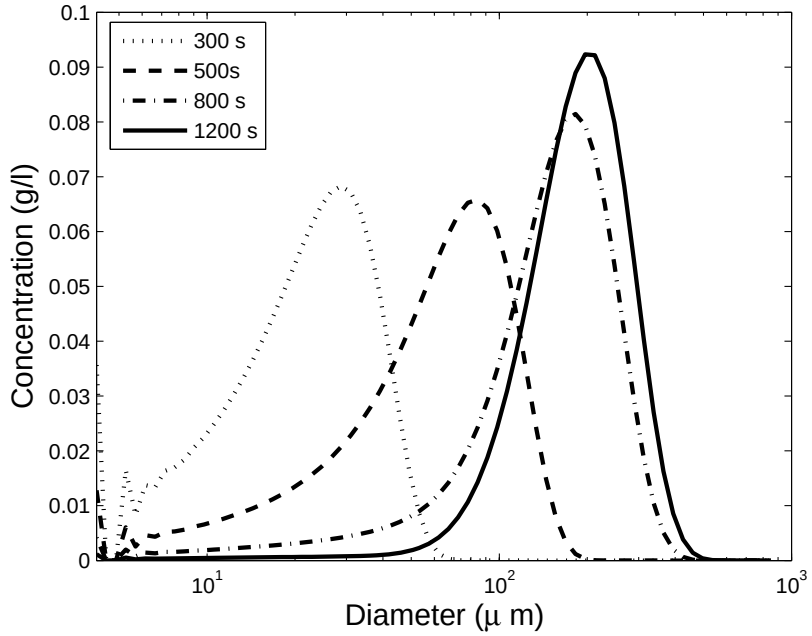

Figure 2 Temporal evolution of floc size distributions for test case T69.

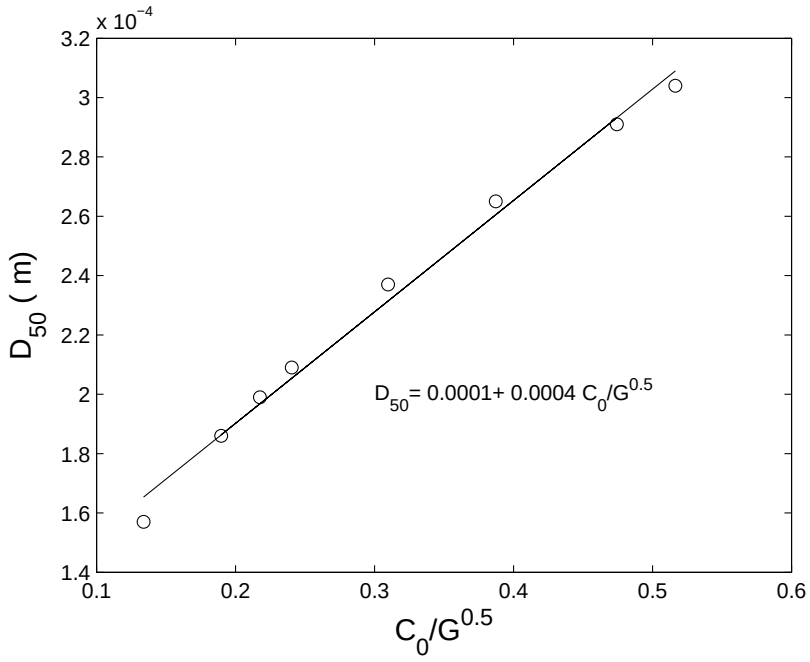

Figure 3 Regression of median floc size (D_{50}) with the ratio of total SSC to square root of shear rate ($C_0 / G^{0.5}$); the line indicates a linear regression fit (γ^2= 0.99).

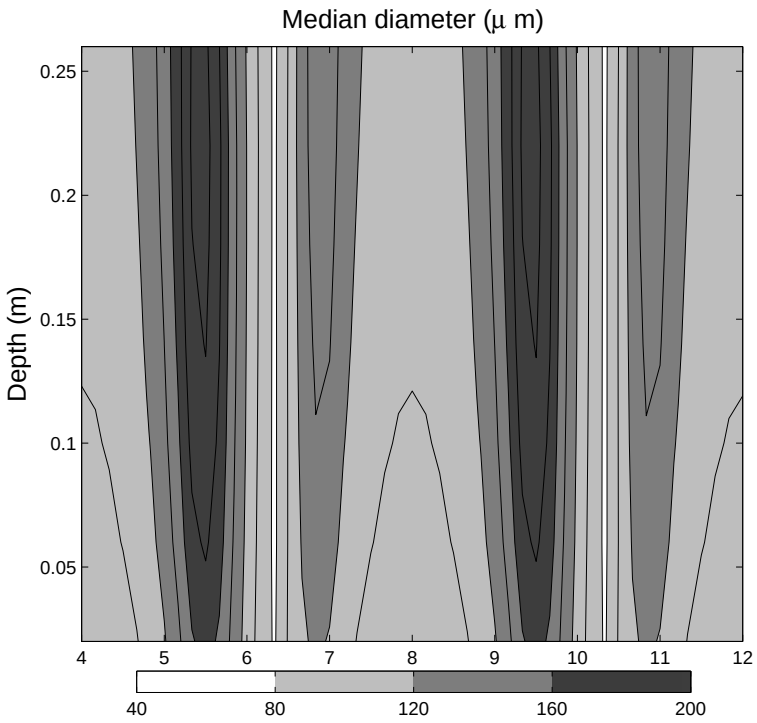

Figure 4 Variations of median floc size (μm) with depth and time (hour) from 1-D simulation.

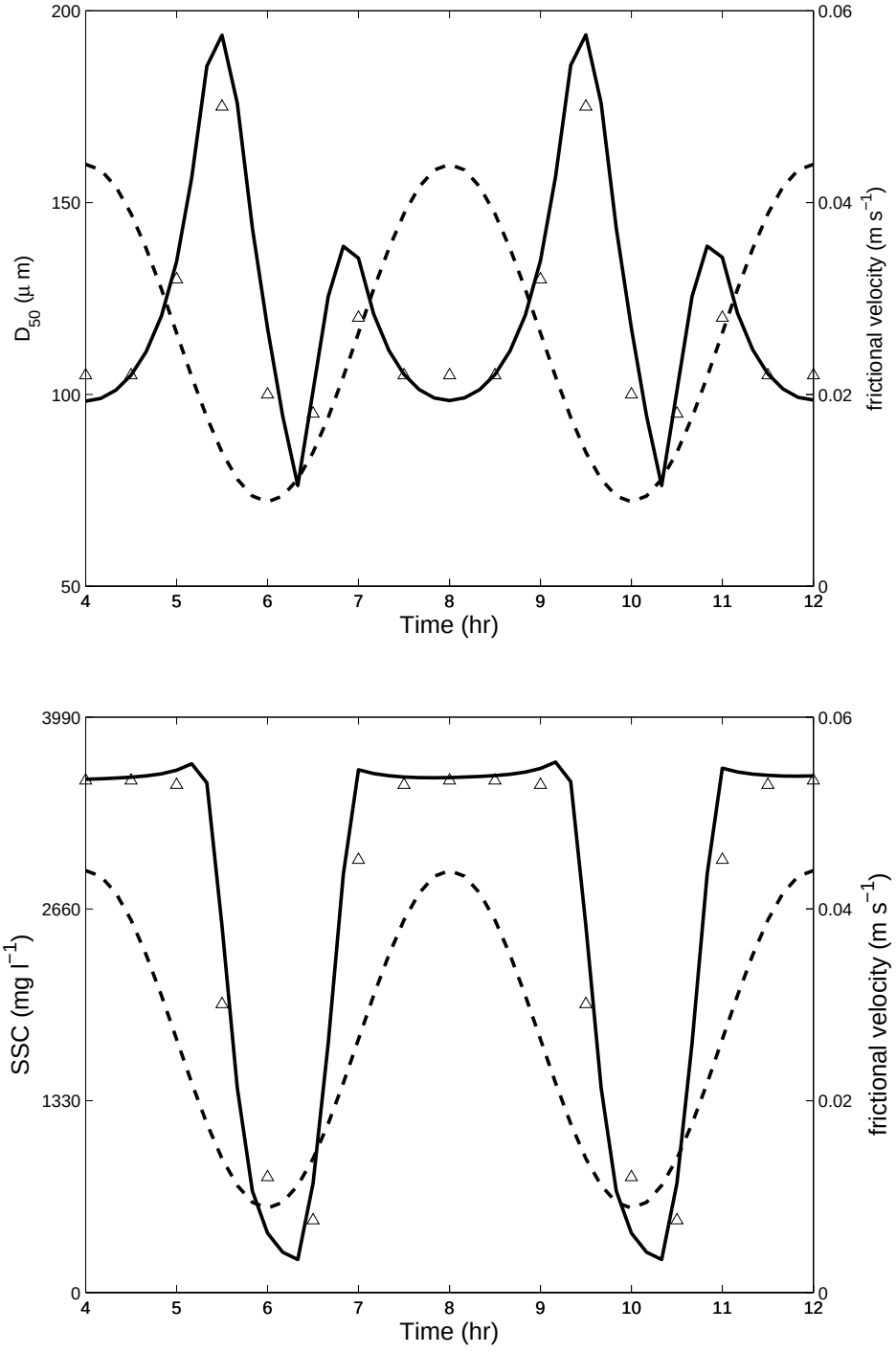

Figure 5 Variations in floc size (solid line) over shortened tidal cycles (upper panel) and variations in SSC (solid line) (lower panel) at 0.1 mab for 1-D simulation. The dash line is the frictional velocity, and the triangles are laboratory data adapted from *Bale et al*., (2002).

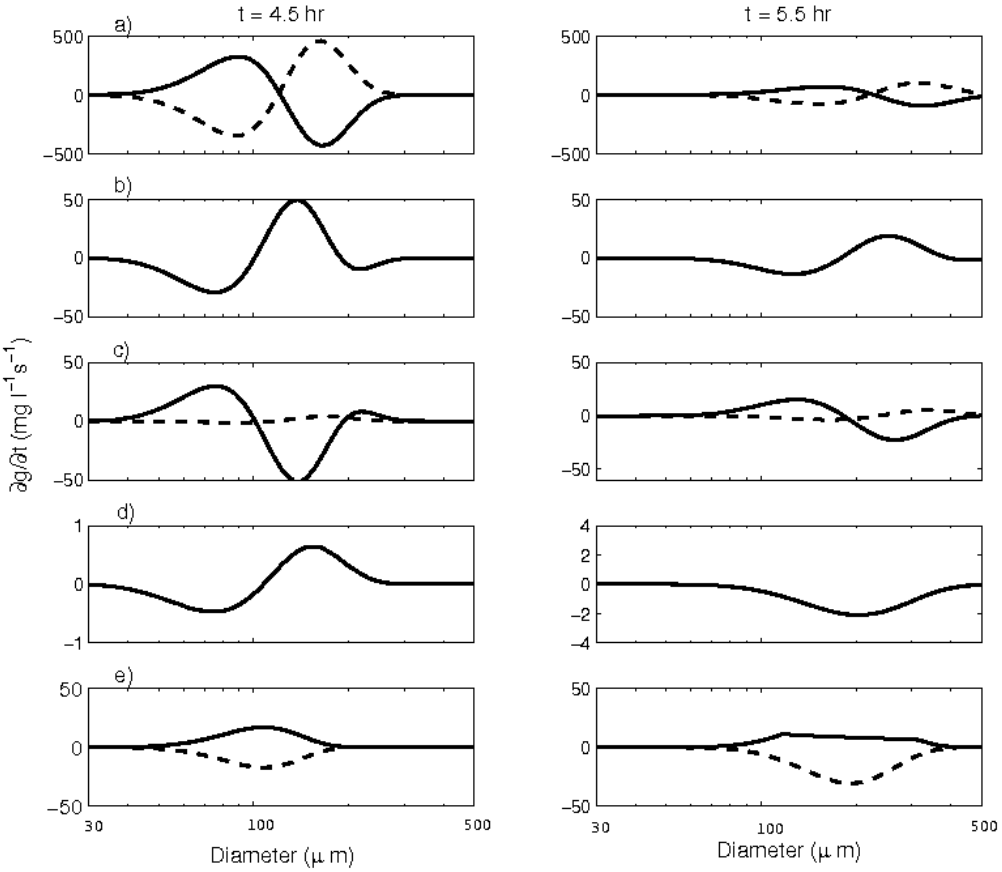

Figure 6 The temporal changes of floc mass density distribution at 0.1 mab by (a) breakup processes (solid line) and aggregation processes (dash line), (b) the sum of changes by aggregation and breakup processes, (c) changes by diffusion (solid line) and sedimentation (dash line), (d) the sum of changes by the above four processes, and (e) by erosion (solid line) and deposition (dash line) at hours 4.5 (left) and 5.5 (right).

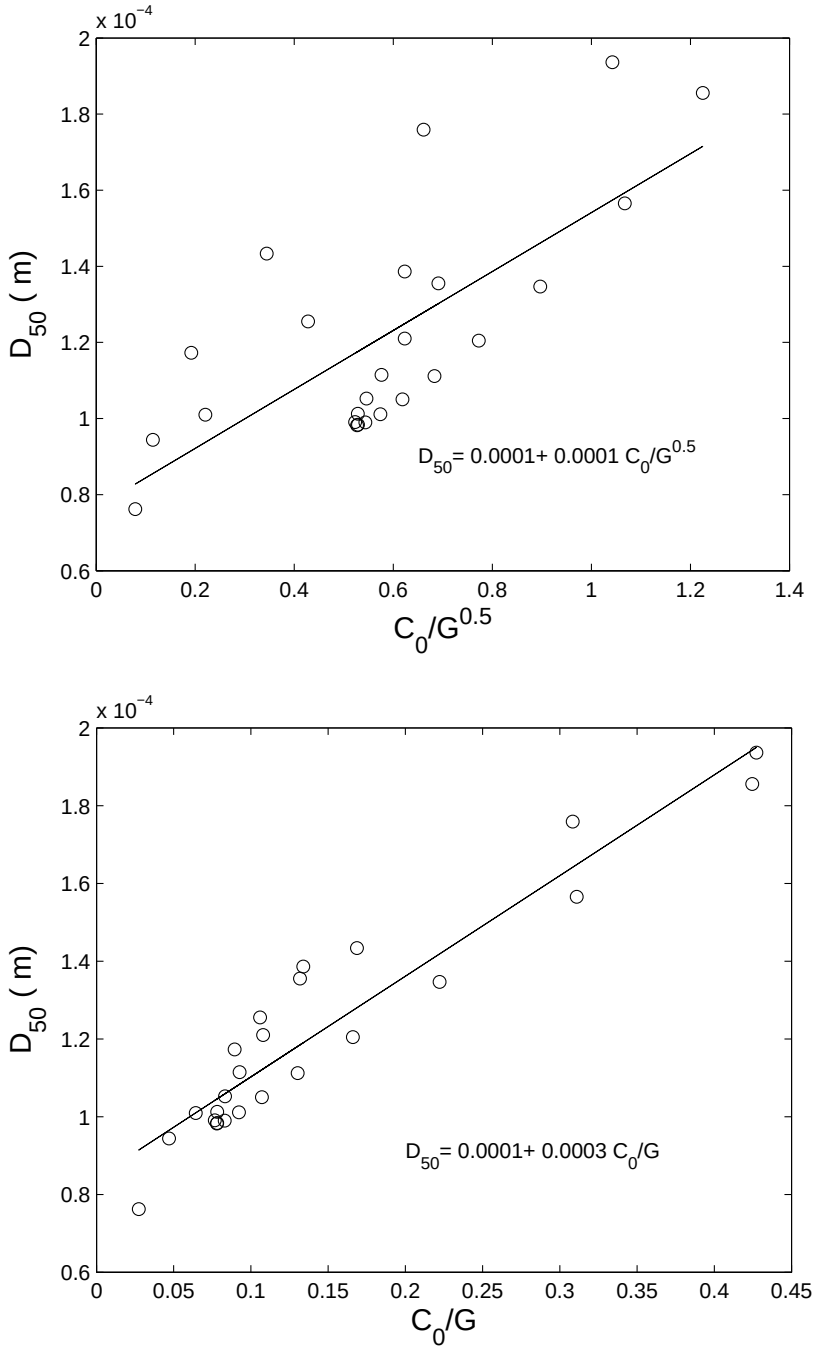

Figure 7 Regression of median floc size (D_{50}) with the ratio of total SSC to square root of shear rate ($C_0/G^{0.5}$); the line indicates a linear regression fit (γ^2=0.52) (upper panel). Regression of median floc size (D_{50}) with the ratio of total SSC to shear rate (C_0/G) ; the line indicates a linear regression fit (γ^2=0.90) (lower panel).

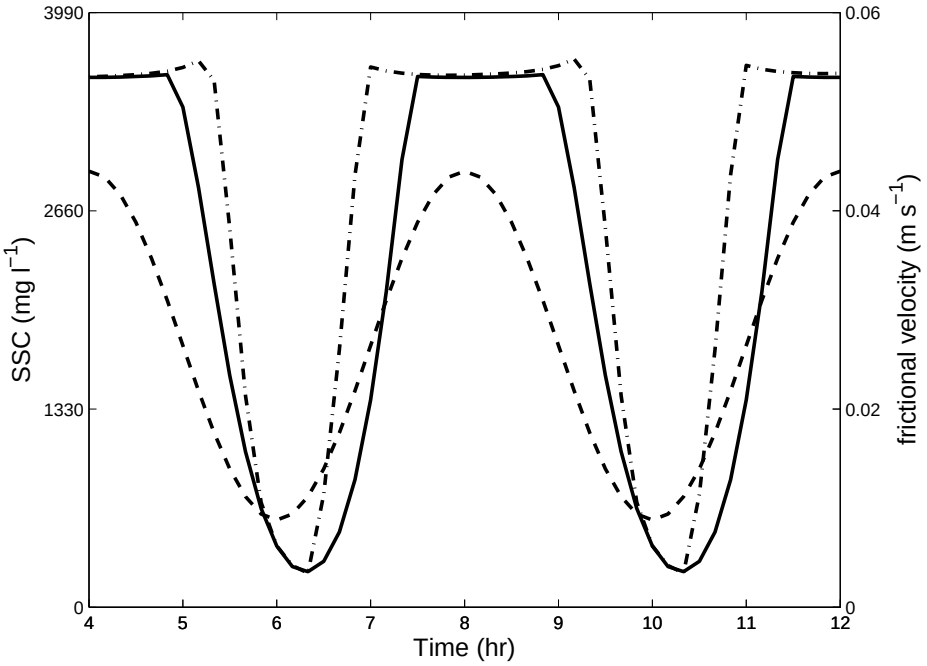

Figure 8 Variations of SSC (solid line) and frictional velocity (dash line) of 1-D simulation without size-resolved flocculation; SSC (dash-dotted line) with flocculation is included for comparison.

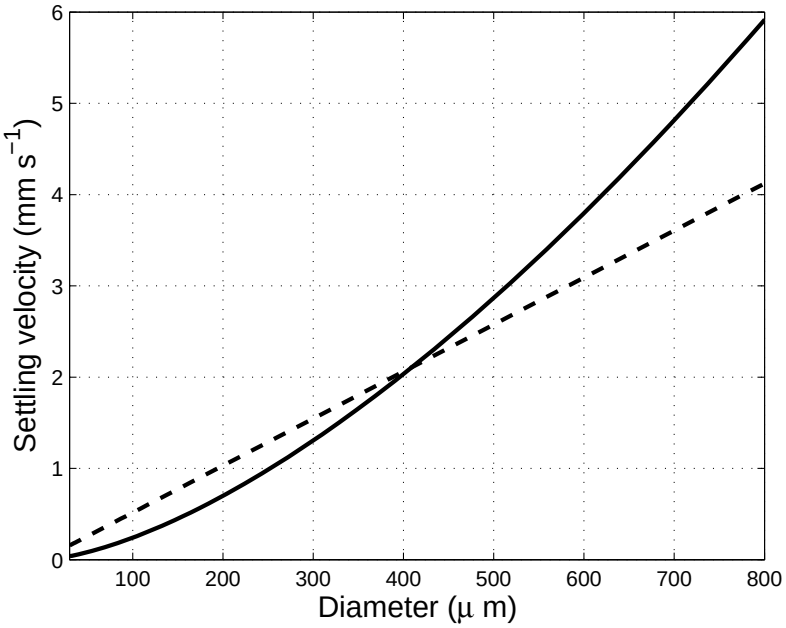

Figure 9 The settling velocity of *Sternberg et al* (1999) (solid line) and *Winterwerp* (2002) (dash line).

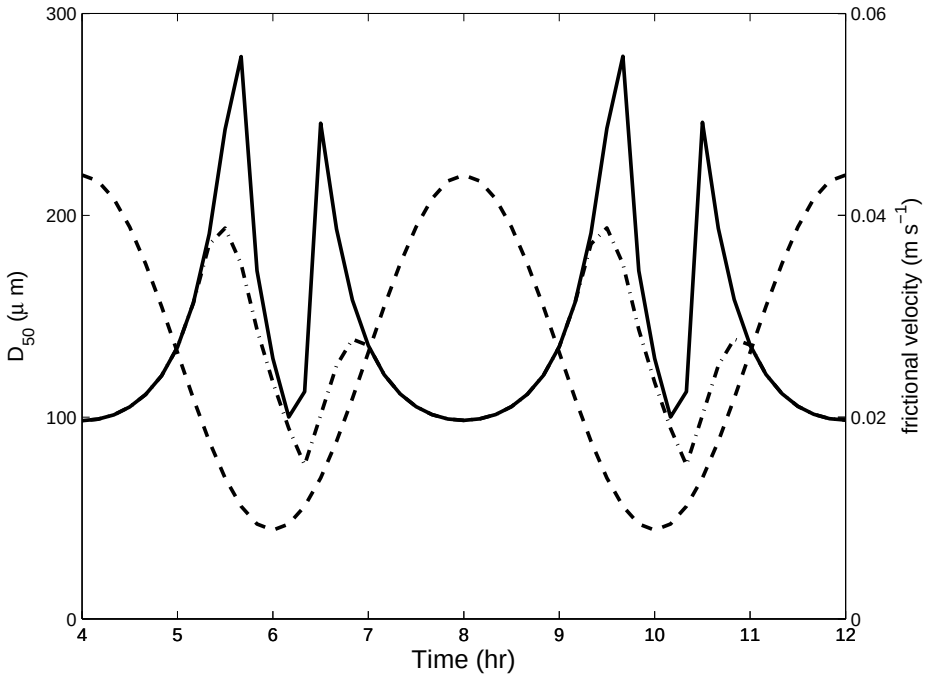

Figure 10 Variations of medium floc size (solid line) and frictional velocity (dash line) over shortened tidal cycles for 1-D simulation with the erosion flux of *Warner et al*. (2005); the median floc size of the base case (dash-dotted line) is included for comparison.

Chapter 3

An idealized study of flocculation effects on sediment trapping in an Estuarine Turbidity Maximum over tidal cycles

3.1 Introduction

An Estuarine Turbidity Maxima (ETM) is characterized as elevated suspended sediment concentration (SSC), which has an important impact on short-timescale stratigraphy (Traykovski et al., 2004) and estuarine ecosystem (Simenstad et al., 1994). Suspended sediment trapping at an ETM has been well documented, e.g. in the upper Chesapeake Bay (Schubel, 1968; Sanford et al., 2001), the Columbia River estuary (Jay and Musiak, 1994), and the Hudson estuary (Traykovski et al., 2004). For instance, in the ETM of the upper Chesapeake Bay, sediment trapping was very efficient during a large flood event in late October 1996 (Sanford et al., 2001).

The mechanisms of particle trapping at an ETM are complex. In general, a residual convergence of the estuarine circulation combined with adequate sediment supply is considered as a fundamental mechanism contributing to ETM formation (Postma, 1967). The convergence occurs where surface seaward flowing freshwater meets bottom landward flowing salty water (referred to as the salt front). In most estuaries, a spatially-limited pool of resuspendable particles is found near the salt front (Sanford et al., 2001), and tidal resuspension has been recognized as a key factor to maintain high SSC (Schubel, 1968). Tidal asymmetry also contributes to the ETM

formation. Tidal velocity profiles generally are surface intensified at ebb but are bottom intensified at flood. Also, vertical mixing tends to be suppressed at ebb but enhanced at flood, caused by the interactions of vertically sheared tidal currents with the along-channel salinity gradients. Jay and Musiak (1994) discussed an upstream net transport of suspended sediments resulting from strong tidal asymmetry in stratification and flow field. Geyer (1993) showed that the suppression of turbulence by density stratification tend to keep the particles near bed at the convergence zone. Lateral interactions between current and topography also have the potential to enhance asymmetric sediment trapping (Geyer et al., 1998).

A number of modeling studies of ETMs have investigated the importance of the aforementioned physical mechanisms. Festa and Hansen (1978) used a numerical model with constant diffusivity to verify that gravitational circulation could successfully trap particles independent of tidal forcing. Burchard and Baumert (1998) evaluated the relative influence of residual gravitational circulation, tidal velocity asymmetry, and tidal mixing asymmetry on the ETM using an idealized two-dimensional (x-z) model. The first two mechanisms are found to be necessary for ETM formation, but the tidal mixing asymmetry does not appear to be essential. North et al. (2004) explored the effects of wind and river pulses on the ETM. During pulse events, salt front structure and circulation pattern were significantly influenced, and so were the transport and distribution of suspended sediments. Park et al. (2008) found that the mechanisms responsible for an ETM formation were different between low and high flow conditions. For a low flow condition, an ETM is mainly formed by local erosion/deposition and the convergence of horizontal bottom sediment flux, while for a high flow condition an ETM

is produced by strong convergence of seaward sediment flux eroded from the upstream of the salt front and landward sediment flux settled near the salt front. Sensitivity of ETM formation to settling velocity, tidal mixing, and sediment supply were tested by Warner et al. (2007). They found that a proper estimate of particle settling velocity was critical for ETM formation. At low settling velocity, ~0.01 mm s^{-1}, particles would suspend long enough to escape from the estuary, whereas with high settling velocity, ~0.5 mm s^{-1}, particles tend to settle quickly upstream of the salt front and contribute little to the ETM.

Flocculation processes enhance particle settling and modulate ETM dynamics (van Leussen, 1994). In an ETM, particle size and settling velocity are continuously changing in response to estuarine conditions. For instance, the size of particles varied with tidal phases in the Hudson estuary that floc size became significantly larger after maximum flood and ebb (Traykovski et al., 2004). In the Humber estuary, UK, Uncles et al. (2006) observed large floc size and enhanced settling at slack waters and low shears. A pronounced SSC close to the bed was found at slack tides as a result of the rapid settling of large flocs. Overall, flocculation has a large impact on the transport and deposition of suspended particles in an ETM.

Previous numerical experiments have focused on effects of the tidal and residual circulation on the ETM formation. The influence of flocculation on ETM formation was only considered as an enhanced constant settling velocity. However, the spatial and temporal impact of flocculation on sediment trapping has not been explored. We have developed a size-resolved method based on the Smoluchowski framework to simulate flocculation (Xu et al., 2008). Our flocculation scheme which predicts the temporal evolution of the floc size distribution compares well with laboratory experiments by

Winterwerp (1998). We also have developed a one-dimensional (1-D) model considering particle settling, deposition, and erosion to simulate the floc size variation with tidal phase. The 1-D simulation results show small floc size during maximum currents and significantly larger sizes as currents decrease. This result, which was validated with laboratory experiments by Bale et al. (2002), is consistent with size distributions typically observed in an ETM.

In the study presented in this manuscript we implement the flocculation scheme into the Princeton Ocean Model (POM), and perform numerical experiments of an idealized estuary in a two-dimensional (*x*-*z*) domain. Our focus is to investigate the influence of flocculation on ETM characteristics and to quantify the different processes that determine the sediment budget during a tidal cycle. The manuscript is organized as follows: Section 2 presents a description of the flocculation scheme and the coupled sediment transport model. The results of the idealized experiments are presented and discussed in section 3 and 4. We conclude in section 5.

3.2. Methodology

3.2.1 The Flocculation scheme

The flocculation scheme has been introduced and tested in our previous work (Xu et al., 2008). Following Xu et al. (2008), we discretize the size distribution of sediment particles into a number of size sections or bins. The following flocculation equation describes the rate of change of mass density including aggregation and breakup:

$$\frac{\partial g(y,t)}{\partial t} = \frac{1}{2}\int_{y_0}^{y} \frac{m^2}{m_c^2 m'} g(y_c,t)K(y_c,y')g(y',t)dy' - \int_{y_0}^{\infty} \frac{1}{m'} g(y,t)K(y,y')g(y',t)dy' + \int_{y_0}^{\infty} \frac{m}{m'} Q(y,y')P(y')g(y',t)dy' - \frac{1}{3m^2} g(y,t)P(y). \quad (1)$$

where *g(y,t)* is the mass density as a function of time *t* and *y*, *y* is the logarithm of particle radius r with mass m , y_0 represents the first bin, $m_c = m - m'$, $y_c = y - y'$, K is the aggregation kernel describing the rate of particle contacts, P is the breakup kernel due to turbulent shear, and Q represents the number density function for the fragments formed by the breakup of a parent particle of mass m'. To denote the mass concentration in each bin, C_j ($= g_j d \ln r$) is used. The sum of C_j over all bins is the SSC.

The aggregation is due to turbulent shear and differential settling. The rectilinear aggregation kernel is $K = \alpha(K_{ts} + K_{ds})$, where α is the particle stickiness, and the kernels K_{ts} and K_{ds} estimate the collision rate per unit volume caused by turbulence shear and differential settling. α is assumed constant for all particle sizes in the study for simplicity. Specifically, the kernels K_{ts} and K_{ds} are given by:

$$K_{ts} = \frac{4}{3} G(r_i + r_j)^3 , \tag{2}$$

and

$$K_{ds} = 5\pi \cdot (r_i + r_j)^2 \cdot \left| w_{s,i} - w_{s,j} \right| , \tag{3}$$

where r_i and r_j are the floc radius, $w_{s,i}$ and $w_{s,j}$ are the settling velocity of flocs in bin *i* and *j*. The shear rate is defined as $G = \sqrt{\varepsilon / \nu}$, where ε is the turbulent dissipation rate and ν is the kinematic viscosity of fluid. The settling velocity is calculated as a function of particle size from Sternberg et al. (1999),

$$w_{s,j} = 347.5602(2r_j)^{1.54} , \tag{4}$$

where r_j is in m, and $w_{s,j}$ is in m s^{-1}. In Equation 3, the coefficient 5 is used to include the fact that irregular floc shapes can increase the efficiency of floc contacts. The selection of the empirical factor has been verified in Xu et al. (2008).

The binary breakup is used in the present study. Q is defined as:

$$Q = \begin{cases} 2 & (m = m'/2) \\ 0 & (m \neq m'/2) \end{cases}. \tag{5}$$

The breakup kernel, P, is a function of shear rate and floc size. Assuming a fractal treatment, the breakup frequency can be written as (Winterwerp, 1998):

$$P_i = E\sqrt{\frac{\mu}{F_y}}G^{1.5}\left(2r_i\right)\left(\frac{r_i - r_1}{r_1}\right)^{3-n_f}, \tag{6}$$

where μ is the dynamic viscosity, n_f is the fractal dimension, and $F_y \approx 10^{-10}$ Pa is the estimated yield strength. The fractal dimension of flocs is defined as (Winterwerp, 2002)

$$n_f = \lim_{L\to\infty}\frac{\ln(N(L))}{\ln(L)}, \tag{7}$$

where *N(L)* is the number of self similar primary particles and *L* is the linear particle size. n_f=2 is applied in calculating breakup kernel.

3.2.2 Circulation model description

The Princeton Ocean Model (POM) (Blumberg and Mellor 1987; Mellor 1998) is a hydrostatic, primitive equation ocean model, and has been used extensively in estuarine circulation studies (e.g. North et al. (2004); Wang (2006)). To simulate suspended sediment flocculation and transport processes, the size-resolved flocculation scheme and a transport component are implemented into POM.

An idealized estuary configured as a flat-bottom, rectangular channel with 25 km long, 1 km wide, and 10 m deep is used. The model's horizontal resolution is 1 km and vertical resolution is ~0.67 m (16 sigma levels). Lateral variations are not considered. At the two open ends, a constant river discharge plus a barotropic, semidiurnal (12-hour) tidal forcing is specified, $\bar{u} = -0.1 + 0.4\sin(2\pi t/T)$ (m s^{-1}). Radiation conditions are used for the outgoing waves. The longitudinal salinity distribution is initiated with $s(x) = 5(1 + \tanh(0.2(L_x/2 + 5000 - x)))$ (psu). The inflow salinity is specified at 0 psu on the east end and 10 psu at the west end.

The model solves the equation for the time variation of mass concentration in each particle size bin,

$$\frac{\partial C_j}{\partial t} + u\frac{\partial C_j}{\partial x} + w\frac{\partial C_j}{\partial z} - \frac{\partial w_{s,j} C_j}{\partial z} = \frac{\partial}{\partial z}\left(K_3 \frac{\partial C_j}{\partial z}\right) + \textit{flocculation}, \qquad (8)$$

where u and w are the longitudinal and vertical velocity respectively, $w_{s,j}$ is the particle settling velocity in the bin j, and K_3 is the vertical eddy diffusivity. Equation (8) describes the change in SSC due to longitudinal and vertical advection, turbulent diffusion, particle settling, and flocculation (Equation 1). A small horizontal diffusion is included only for numerical stability. The whole model is fully coupled so that u and w are predicted by POM. The Mellor-Yamada level 2.5 turbulence closure (Mellor and Yamada, 1974) is used to obtain K_3 and ε. The particle mass flux from bottom erosion $E_{s,j}$ in bin j is described as:

$$K_3 \frac{\partial C_j}{\partial z}\bigg|_{bottom} = E_{s,j} = E_{0,j}\left(\frac{\tau_b}{\tau_c} - 1\right)/\, j\,, \quad \text{when} \quad \tau_b > \tau_c \qquad (9)$$

where $E_{0,j}$ is a bed erodibility constant, assumed to be 1×10^{-3} kg m^{-2} s^{-1} for all size ranges. The bin number *j* in the denominator is used to account for the fact that larger particles are more difficult to erode than smaller ones. This expression for erosion flux has been successfully used in Xu et al. (2008). The bed shear stress $\tau_b = \rho C_d u\sqrt{u^2+v^2}$, where ρ is the reference density, 1025 kg m^{-3}. τ_c is the critical shear stress for erosion and is set to 0.05 pa in the study (Warner et al., 2005). Considering the rapid tidal phase change, the consolidation process can be neglected (Uncles et al., 2006).

The model runs from rest until the circulation reaches a quasi-periodic state. Then, a vertically well-mixed constant loading of suspended primary particles, 0.1 kg m^{-3}, is imposed at the east boundary. The size of primary particle is 30 μm, which is the typical size of robust microflocs present in estuaries, like the upper Chesapeake Bay (Sanford et al. 2005). The total bin number *n* is set to be 50. Thus, the size of flocs can vary in 30-1277 μm, which includes most of the floc size range in estuaries. The external and internal time steps for the circulation model are 5 s and 50 s, respectively, and for the flocculation, 0.25 s is used. The SSC also will reach a quasi-periodic state. Six simulation tests are carried out. Simulations with or without size-resolved flocculation are done to explore the influence of flocculation on sediment trapping. The other simulations aim at testing the sensitivity of the model towards particle stickiness and the upstream loading of suspended sediments. They are summarized in Table 1.

3.3 Model Results

3.3.1 Salinity and velocity

Figure 1 illustrates along-channel variations in salinity and velocity from hour 156 toward hour 166. The salt front, defined as 1 psu isohaline, moves back and forth

with tidal currents from x=11 to x=15 km. Upstream (landward) of the salt front the water column is fresh. Downstream (seaward) of the salt front the salinity distributions vary with tidal currents, more stratified on ebbs than on floods. The estuarine circulation converges within the salt front. Figure 2 shows velocity profiles every two hours at x=4 km and x=20 km. The gravitational circulation is evident in intensified surface outflow during ebb and stronger bottom inflow on flood. At x=4 km, strong sheared ebb currents is present while a subsurface velocity maximum is developed during flood tide. At x=20 km, the water column is well-mixed in all tidal phases with maximum currents near surface. Figure 3 shows the salinity and along-channel velocity contours over a tidal cycle at the mean front location, x=13 km. The hour 156 denotes the slack tide before flood, and hour 162 denotes the slack tide before ebb. The time series begins at the end of ebb tide. The water column is well-mixed, since the salt front is further downstream. As the tide turns to flood, the salt front moves upstream past the transect location, and a well-developed bottom boundary layer is present capped by a sharp pycnocline. Also, a subsurface velocity maximum is present in the middle of the water column at the top of the bottom mixed layer during strong flood tide. In the following ebb tide, the salt front moves back past the transect location. The velocity maximum reaches towards the surface as a result of tidal currents enhanced by gravitational circulation. The strong tidal velocity asymmetry agrees well with observations in the Hudson River (Chant and Wilson, 2000).

3.3.2 One-size flocculation simulation (Run 1)

In the one-size flocculation simulation (Run 1), the settling velocity of particles must be properly estimated in order to create a pronounced ETM. According to simulated

salinity and velocity profiles, a dimensionless trapping length, l, is applied to estimate the settling velocity, $l = u_1 h_1 / w_s L$, where u_1 is the tidally-averaged velocity at the upper layer of convergence region, h_1 is the thickness of the bottom boundary layer, and L is the length of the salt intrusion. For l~1, a stable well-defined ETM can be formed (Geyer, 1993; Warner et al., 2007). Otherwise, if $l>1$ the sediments move out of the salt front region with few particles trapped, and when $l<<1$ all particles are trapped in a small area at the toe of the salt front. In the simulation, u_1 is about 0.22 m s^{-1}, h_1 is about 5 m, and L is about 4 km, hence w_s=0.35 mm s^{-1}, corresponding to l = 0.8, is chosen in order to form a stable ETM. The equivalent floc size is 127 μm (Equation 7).

Figure 4 shows snapshots of 1 psu isohaline and SSC distributions for the same points in time as in Fig.1. Landward of the salt front, SSC is ~0.1 kg m^{-3} (background value of SSC). Suspended sediments are trapped near the salt front, and move with the tidal currents. The center of the ETM is slightly upstream of the salt front at ebb (at hour 156 and 166), while it is further downstream at flood (e.g. hour 158 and 160). The fact that the ETM is behind the salt front in the direction of tidal flow is due to the tidal resuspension lag (Dyer and Evans, 1989). It is delayed because erosion takes place only after tidal velocity reaches the critical shear stress. The maximum SSC varies slightly around 0.2 kg m^{-3} over the tidal cycle. Then, an ETM is permanently present due to the small settling velocity.

A spatially limited pool of resuspendable sediment is observed near the salt front from x = 10 to 15 km (Fig. 5). It is mainly produced by the convergence of estuarine circulation. During flood (hour 158, 160, and 162), there is a net accumulation of bottom sediments landward of the salt front. As currents start to ebb (hour 164), these

accumulated sediments are gradually resuspended. This contributes to SSC increasing landward of the salt front (Fig. 4).

3.3.3 Simulation with flocculation processes/size-resolved flocculation simulation (Run 2)

Simulation with flocculation (Run 2) is done to investigate the modulation of flocculation on particle trapping in an ETM. The simulation setup is identical to the previous simulation except with the flocculation included. The particle stickiness α is fixed at 0.3. The salinity distribution and velocity structure are the same as those shown in Fig. 1. On the other hand, the SSC and its along-channel distributions show larger variations within a tidal cycle (Fig. 6). At slack tides (hour 156 and 162), the SSC in salt front region is low, about 0.2 kg m^{-3}. The SSC increases to more than 1 kg m^{-3} on flood (hour 158 and 160) and about 0.5 kg m^{-3} on ebb (hour 164 and 166). The salt front also leads the center of the ETM in the direction of tidal flows.

Figure 7 shows longitudinal distributions of median floc size (D_{50}) at the same six tidal phases as in Fig. 6. The predicted background median particle size is about 50 μm. Large flocs (>100 μm) are formed near the salt front due to convergence of suspended particles. At hour 156, the floc size increases up to 150 μm near the bottom. Note that the maximum SSC (Fig. 6) and D_{50} (Fig 7) are not coincident. The maximum SSC is located slightly landward of the salt front. On the other hand, the maximum D_{50} is seaward of the salt front because of the reduced turbulence. At subsequent flood tide, although the SSC is increasing, the median floc size is still about 150 μm (hour 160) because strong turbulent mixing limits floc growth. The largest flocs (over 300 μm) are formed at slack

tide before ebb due to the strong differential settling and reduced turbulence. On ebb, the maximum floc size is only about 100 μm due to the dominance of breakup process.

Figure 8 shows floc size distributions near the salt front region (x=13 km) and the corresponding settling flux at 1.7 meter above bottom (mab). At slack tide before flood (hour 156), concentrations of flocs are very low (~0.004 kg m^{-3}) with size in the range of 30 - 150 μm. With increasing flood currents (hour 159), SSC increases (~0.05 kg m^{-3}), and the floc size range extends to 60 ~ 250 μm with D_{50}=180 μm. At slack tide before ebb (hour 162), the floc size further increases with D_{50}=300 μm despite the low SSC (~0.02 kg m^{-3}). Resuspension at ebb tide (hour 165) increases SSC again (~0.0025 kg m^{-3}), but the strong shear limits floc growth with median floc size D_{50}=110 μm. The settling flux of particles ($w_{s,i}C_i$) varies significantly within the tidal cycle due to the floc size variations. For instance, settling flux at hour 162 is about two times larger than at hour 165 even though the floc concentration is higher at hour 165. The differences in settling flux result in the pronounced variations in SSC over a tidal cycle (Fig. 6).

A pool of resuspendable particles near the salt front also is created (Fig. 9). The sediment pool moves back and forth following the salt front. This indicates strong resuspension and deposition variability within a tidal cycle. With strong flood currents, most of particles are resuspended, resulting in the large SSC increase at hour 160 (Fig. 6). Comparing Fig. 9 to Fig. 5, Run 2 produces more tidal asymmetrical sediment accumulation than the Run 1.

Resuspension flux and deposition flux are compared in Fig. 10 at the same six tidal phases as in Fig. 6. Most of resuspension and deposition flux are present near the salt front. At slack tides (hour 156 and 162), only the deposition flux exists with peak

value about 2.5×10^{-4} kg m^{-2} s^{-1} for the former and 4.5×10^{-4} kg m^{-2} s^{-1} for the latter. During early flood and ebb tides (hour 158 and 164), the resuspension flux is about three times larger than the deposition flux. At strong flood tide (hour 160), the two are comparable with the peak resuspension flux slightly larger by about 1.0×10^{-4} kg m^{-2} s^{-1}. On the other hand, at strong ebb tide (hour 166) both fluxes are very small with dominant deposition flux. The tidal asymmetrical variations in the two fluxes at the water-bed interface determine the movement and change of the bottom sediment pool (Fig. 9). A net seaward movement of sediment pool on late ebb (hour 166 and 156) produces two concentration maxima of sediments caused by the dominant deposition flux downstream of the salt front. Enhanced resuspension at flood tide (hour 158 and 160) reduces the sediment pool and destroys the bimodal distribution. At flood slack (hour 162), a net landward movement of bottom sediments results from the large deposition flux.

To investigate the influence of the deposition flux, resuspension flux and horizontal advective flux on the SSC variations in the water column, a suspended sediment budget at six tidal phases as in Fig. 10 is examined (Fig. 11). In the water column, the net mass change of suspended sediments ($C_t = \partial / \partial t \iiint C dx dy dz$) is mainly caused by the horizontal advection ($uC_x = \delta_x \iint uC dy dz$) and deposition plus resuspension ($DE = \iint (-wC + E_s) dx dy$) at the water-bed interface. At slack tide before flood (hour 156), deposition (negative *DE*) causes the SSC decrease. As currents tend to flood (hour 158), resuspension of previously deposited particles (positive *DE*) mainly contributes to the SSC increase (C_t), while advection (uC_x) becomes important in the following flood tide (hour 160). At the end of flood (hour 162), many suspended sediments settle to the bed (negative *DE*). Resuspension (positive *DE*) becomes

dominant again with the ebb current increasing (hour 164). At late ebb tide (hour 166), the seaward advection of suspended sediments (uC_x) is a dominant factor for the SSC downstream movement. Therefore, both horizontal advection (uC_x) and resuspension and deposition (DE) at bottom boundary are important for the ETM variations over a tidal cycle, but the dominant process varies with the tidal phases.

3.4 Discussion

In the conceptual model proposed by Sanford et al. (2001), the gravitational circulation and tidal asymmetry combined with asymmetrical tidal resuspension and transport of flocs are primarily responsible for the ETM formation. At slack before flood, only the gravitational circulation exists and the mixing is weak. Most of the suspended sediments settle to the bed. On flood, strong resuspension occurs due to intensified bottom currents. Then, the suspended sediments are advected landward toward the salt front. At slack before ebb, previously resuspended particles settle near the salt front. On ebb, the sediments are resuspended again and advected seaward. Seaward of the salt front, strong stratification in the upper water column favors particle sedimentation and subsequent accumulation to the bed. The sediment will again be resuspended in the following flood, repeating the cycle. The variability of SSC within a tidal cycle in the conceptual model is clearly exhibited in Run 2 (Fig. 6). The SSC near the salt front on flood tide is about twice larger than that on ebb tide. This is consistent with observations in the ETM of the upper Chesapeake Bay, where the near bottom SSC on flood was three times higher than that on ebb (Sanford et al. 2001). Run 1 also shows similar SSC variation pattern except that the range is small (Fig. 4). In addition, a suspended sediment budget for Run 1 illustrates that the C_t, uC_x and DE are only 20 percent of those

for Run 2 for all tidal phases, and during flood the small *DE* becomes comparable with uC_x. For Run 1, the tidal asymmetrical variations in SSC is mainly caused by tidal asymmetry in turbulent mixing, while for Run 2 the enhanced settling flux in the water column combined with larger resuspension flux on flood than those on ebb reinforce the intratidal variations. Run 2 reproduces more realistic results than Run 1 in terms of particle trapping and its intratidal variability. The flocculation processes play a key role in the strong tidal asymmetrical SSC variations and particle trapping.

The presence of an ETM is often associated with a spatially limited pool of resuspendable particles (Sanford et al., 2001). The existence of such a particle pool is present in both simulations. To investigate the importance of resuspension of these particles, another simulation with reduced tidal currents (0.2 m s^{-1}) is done (Run 3). No clear ETM is created and most of particles are deposited to the bottom near the salt front (not shown in the paper). The results emphasize the role of resuspension in the ETM formation.

Sensitivity studies are performed to investigate the influence of particle stickiness (α). The model setup is the same as the flocculation simulation except that α is changed from 0.3 (Run 2) to 0.1 and 0.6. Fig. 12 compares the tidally-averaged SSC distributions at different stickiness. At α =0.1 (Run 4), the SSC is about 0.2 kg m^{-3}, confined to the bottom in $4 < x < 14$ km. The median floc size is only about 50 μm, and settling velocity is about 0.08 mm s^{-1} with little change with tidal currents. Few particles are trapped at this low stickiness case due to low settling velocity. At α =0.6 (Run 5), the results are similar to α =0.3 (Run 2), though the suspended particles are more constrained in the salt front from km 10 to 15. The median floc size varies from 200 to 400 μm near the salt

front. The large floc size favors settling and subsequent particle trapping. Therefore, particle stickiness is very important for particle trapping.

In Run 2 the background SSC of 0.1 kg/m^3 is used, which is larger than typically found in the upper Chesapeake Bay (Sanford et al. 2001) and the Hudson River estuary (Orton and Kineke, 2001). Another simulation (Run 6) is carried out using a background SSC of 0.03 kg m^{-3} (Table 1). Note that the particle stickiness is increased to 0.6 to form large flocs under the low background SSC. Comparing the simulation results (Fig. 13 & 14) with Run 2 results (Fig. 6 & 7), similar variations in SSC and D_{50} are found. More particles are trapped on flood than on ebb. The near bottom SSC in the ETM at maximum currents is about ten times larger than the background value. The maximum median floc size is over 300 μm obtained at the slack tide before ebb, and the floc size decreases with increasing of tidal currents. The comparison illustrates that the decrease of background SSC changes the absolute amount of sediment trapping in the ETM but the variation of SSC and D_{50} with tidal currents remains about the same.

3.5 Conclusion

The study suggests that the gravitational circulation and tidal asymmetrical resuspension and transport are primarily responsible for an ETM formation. The variability of SSC near the salt front within a tidal cycle is reproduced well by the flocculation simulation. In contrast, although the convergence of suspended sediments near the salt front can be created by the one-size flocculation simulation, the variability of SSC within a tidal cycle is not produced at all. Also, a proper estimate of the constant settling velocity is required for a one-size flocculation simulation. Therefore, a realistic ETM simulation must include flocculation processes.

Analysis of suspended sediment budget shows that the roles of horizontal advection, deposition, and resuspension change with tidal phases. At early flood or ebb tides, resuspension is important. With the increasing of tidal current, advection becomes dominant. At slack tides, the formation of large flocs favors deposition. For each process, its magnitude varies significantly between flood and ebb tides.

Particle trapping in an ETM is closely associated with a pool of resuspendable particles near the salt front. In the study, the tidal asymmetrical transport of flocs is mainly responsible for the formation of the sediment pool. Another key factor for particle trapping is the particle stickiness, which has a large natural variability (0.001~1). The sensitivity tests exhibit that a proper estimate of the particle stickiness is necessary.

References

Ariathurai, C.R., Arulanandan, K., 1978. Erosion rates of cohesive soils, *Journal of the Hydraulics Division*, ASCE 104(2), 279-282.

Bale, A.J., Uncles, R.J., Widdows, J., Brinsley, M.D., Barrett, C.D., 2002. Direct observation of the formation and break-up of aggregates in an annular flume using laser reflectance particle sizing, in Winterwerp, J.C., Kranenburg C. (Eds.), Fine Sediment Dynamics in the Marine Environment, Elsevier, pp. 189-201.

Bott, A., 1989. A positive definite advection scheme obtained by nonlinear renormalization of the advection fluxes, *Monthly Weather Review*, 117, 1006-1015.

Bott, A., 1998. A flux method for the numerical solution of the stochastic collection equation, *Journal of Atmospheric Sciences*, 55, 2284-2293.

Burchard, H., Baumert, H., 1998. The formation of estuarine turbidity maxima due to density effects in the salt wedge. A hydrodynamic process study. *Journal of Physical Oceanography*, 28, 309-321.

Chant, R.J., Wilson, R.E., 2000. Internal hydraulics and mixing in a highly stratified estuary, *Journal of Geophysical Research*, 105, 14,215-14,222.

Dyer, K.R., Evans, E.M., 1989. Dynamics of turbidity maximum in a homogenous tidal channel. *Journal of Coastal Research* SI: 23-36.

Dyer, K.R., Manning, A.J., 1999. Observation of the size, settling velocity and effective density of flocs, and their fractal dimensions, *Journal of Sea Research*, 41, 87-95.

Geyer, W.R., 1993. The importance of suppression of turbulence by stratification on the estuarine turbidity maximum. *Estuaries*, 16, 113-125.

Geyer, W.R., Signell, R., Kineke, G., 1998. Lateral trapping of sediment in a partially mixed estuaries, In: Dronkers, J., Scheffers, M. (Eds.), Physics of Estuaries and Coastal

Seas: Proceedings of the 8th International Biennial Conference on Physics of Estuaries and Coastal Seas. A.A. Balkema, Rotterdam, The Netherlands, pp. 115-124.

Geyer, W.R., Hill, P.S., Kineke, G.C., 2004. The transport, transformation and dispersal of sediment by buoyant coastal flows, *Continental Shelf Research*, 24, 927-949.

Jay, D.A., Musiak, J.D., 1994. Particle trapping in estuarine tidal flows. *Journal of Geophysical Research*, 99, 20,445-20,461.

Hill, P.S., Milligan, T.G., Geyer, W.R., 2000. Controls on effective settling velocity in the Eel River flood plume, *Continental Shelf Research*, 20, 2095-2111.

Hill, P.S., Voulgaris, G., Trowbridge, J.H., 2001. Controls on floc size in a continental shelf bottom boundary layer, *Journal of Geophysical Research*, 106(C5), 9543-9549.

Hunt, J.R. 1986. Particle aggregate breakup by fluid shear, in Mehta A.J. (Eds.), Estuarine Cohesive Sediment Dynamics, Springer, Berlin, pp. 85-109.

Kranck, K., Milligan, T.G., 1992. Characteristics of suspended particles at an 11-hour anchor station in San Francisco Bay, California, *Journal of Geophysical Research*, 97, 11,373-11,382.

Van Leussen, W., 1994, Estuarine macroflocs and their role in fine-grained sediment transport, Ph.D. Thesis, University of Utrecht, Netherlands.

Mellor, G.L., Yamada, T., 1974. A hierarchy of turbulence closure models for planetary boundary layers. *Journal of Atmospheric Science* 31: 1791-1806.

North, E.W., Chao, S.-Y., Sanford, L.P., Hood, R.R., 2004. The influence of wind and river pulses on an estuarine turbidity maximum: Numerical studies and field observations in Chesapeake Bay. *Estuaries*, 27, 132-146.

Orton, P.M., Kineke, G.C., 2001. Comparing calculated and observed vertical suspended-sediment distributions from a Hudson River Estuary turbidity maximum, *Estuarine, Coastal and Shelf Science*, 52, 401-410.

Park, K., Wang, H.V., Kim, S.C., 2008. A model study of estuarine turbidity maximum along the main channel of the upper Chesapeake Bay. *Estuaries and Coasts*, 31, 115-133.

Postma, H., 1967. Sediment transport and sedimentation in the estuarine environment. In: Lauff, G.H. (Eds.), Estuaries, American Association Advanced Scientific Publication 83, Washington, D.C., pp. 158-179.

Sanford, L.P., Dickhudt, P.J., Rubiano-Gomez, L., Yates, M., Suttles, S.E., Friedrichs, C.T., Fugate, D.D., Romine, H., 2005. Variability of suspended particle concentrations, sizes, and settling velocities in the Chesapeake Bay turbidity maximum. In: Droppo, I.G., Leppard, G.G., Liss, S.N., Milligan, T.G. (Eds.), Flocculation in Natural and Engineered Environmental Systems, Boca Raton, Florida, CRC Press, pp. 211-236.

Sanford, L.P., Suttles S.E., Halka, J.P., 2001. Reconsidering the physics of the Chesapeake Bay estuarine turbidity maximum. *Estuaries*, 24, 655-669.

Schubel, J.R., 1968. Turbidity maximum of the northern Chesapeake Bay. *Science*, 161:1013-1015.

Simenstad, C.A., Morgan, C.A., Cordell, J.R., Baross, J.A., 1994. Flux, passive retention, and active residence of zooplankton in Columbia River estuarine turbidity maxima. In: Dyer, K.R., Orth, R.J. (Eds.), Changes in Fluxesin Estuarines: Implications from Science to Management, Olsen and Olsen, Fredensborg, Denmark, pp. 473-482.

Sternberg, R.W., Berhane, I., Ogston, A.S., 1999. Measurement of size and settling velocity of suspended aggregates on the northern California continental shelf, *Marine Geology*, 154, 43-53.

Traykovski, P., Geyer, W.R., Sommerfield, C., 2004. Rapid sediment deposition and fine-scale strata formation in the Hudson estuary, *Journal of Geophysical Research*, 109, F02004, doi:10.1029/2003JF000096.

Uncles, R.J., Stephens, J.A., Law, D.J., 2006. Turbidity maximum in the macrotidal, highly turbid Humber Estuary, UK: Flocs, fluid mud, stationary suspensions and tidal bores, *Estuarine, Coastal and Shelf Science*, 67, 30-52.

Wang, D.P., 2006. Tidally generated internal waves in partially mixed estuaries, *Continental Shelf Research*, 26, 1469-1480.

Warner, J.C., Sherwood, C.R., Geyer, W.R., 2007. Sensitivity of estuarine turbidity maximum to settling velocity, tidal mixing, and sediment supply. In: Maa, J.P.-Y., Sanford, L.P., Schoellhamer, D.H. (Eds.), Estuarine and Coastal Fine Sediments Dynamics – Proceedings in Marine Science, vol. 8. Elsevier, Amsterdam, pp. 355-376.

Winterwerp, J.C., 1998. A simple model for turbulence induced flocculation of cohesive sediment, *Journal of Hydraulic Research*, 36, 309-326.

Winterwerp, J.C., 2002. On the flocculation and settling velocity of estuarine mud, *Continental Shelf Research*, 22, 1339-1360.

Xu, F., Wang, D.P., Riemer, N., 2008. Modeling flocculation processes of fine-grained particles using a size-resolved method: Comparison with published laboratory experiments, *Continental Shelf Research*, 28, 2668-2677.

Zhang, J.J., Li, X.Y., 2003. Modeling particle-size distribution dynamics in a flocculation system, *American Institute of Chemical Engineers*, 49, 1870-1882.

Tabel 1 Summary of six simulation tests

Model Run	Flocculation scheme	Upstream sediment input (kg m^{-3})	Amplitude of tidal currents (m s^{-1})	Particle stickiness
Run 1	No	0.1	0.4	N/A
Run 2	Yes	0.1	0.4	0.3
Run 3	Yes	0.1	0.2	0.3
Run 4	Yes	0.1	0.4	0.1
Run 5	Yes	0.1	0.4	0.6
Run 6	Yes	0.03	0.4	0.6

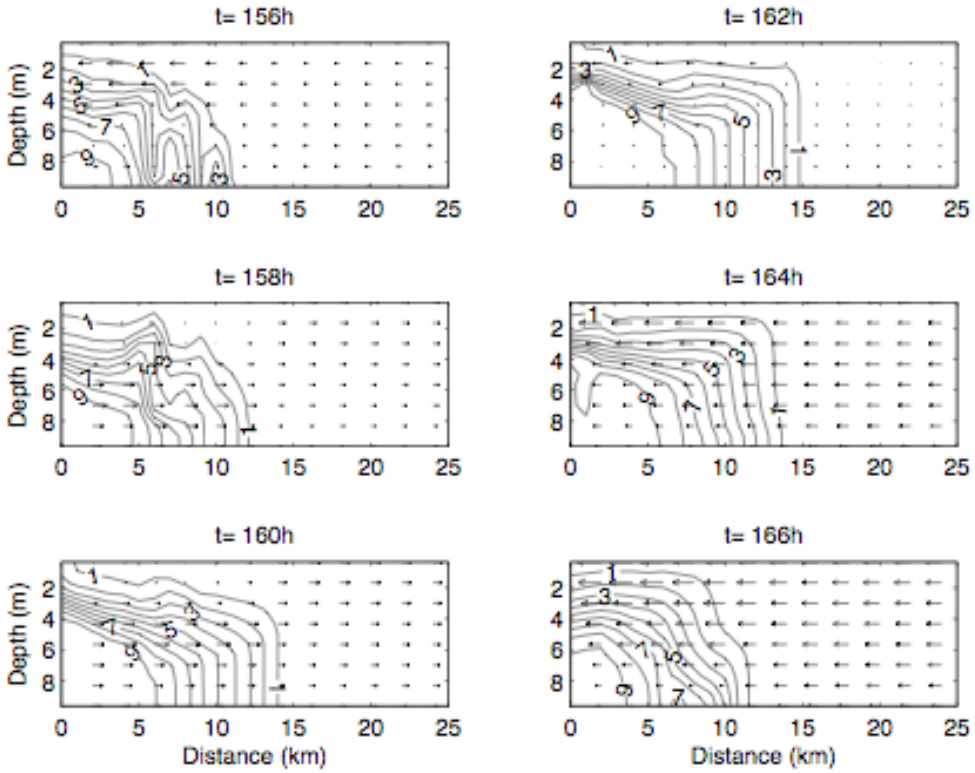

Figure 1 Snapshots of along channel salinity contours in psu (solid lines) and velocity vectors from hour 156 to 166. The hour 156 denotes the slack tide before flood, and hour 162 denotes the slack tide before ebb.

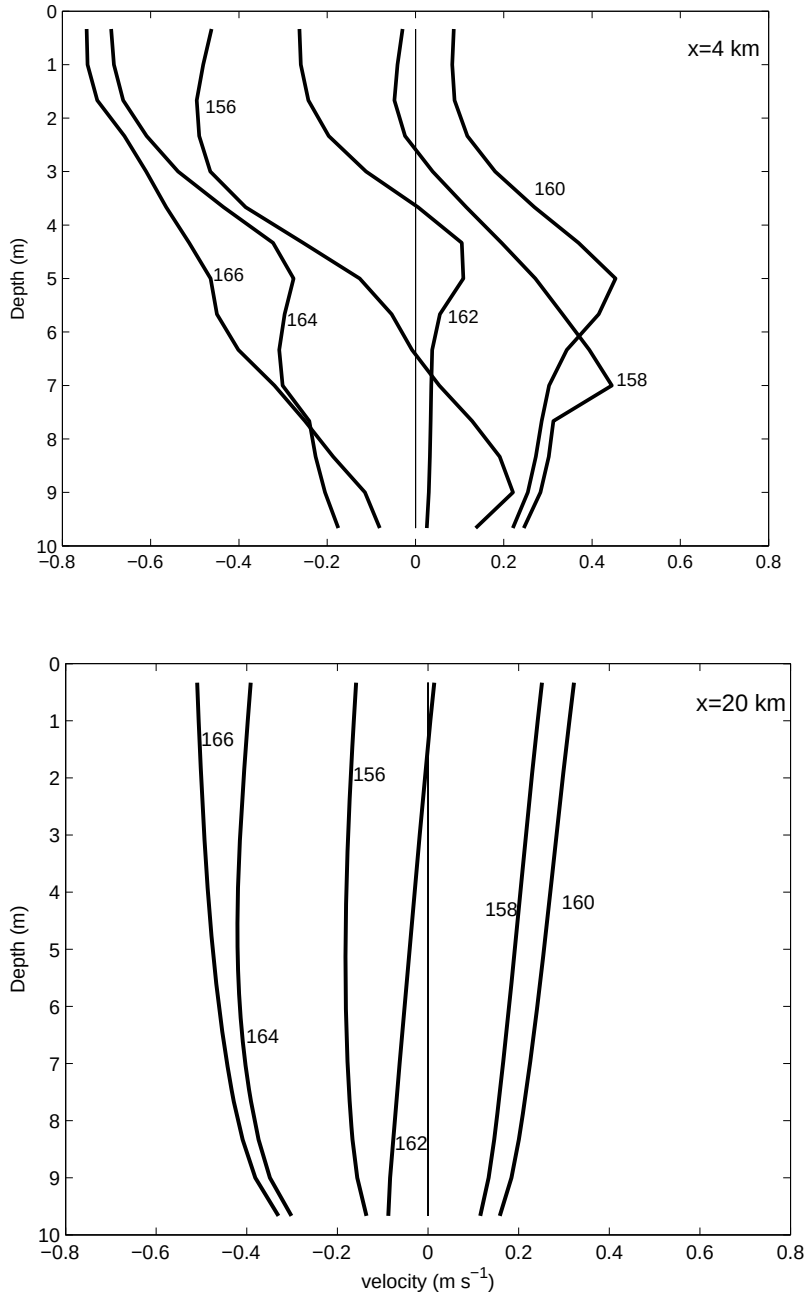

Figure 2 Along-channel velocity profiles over a tidal cycle at x=4 km (upper panel), and x=20 km (lower panel). The time (in hour) is marked in each profile. Positive velocities are flood. The hour 156 denotes the slack tide before flood, and hour 162 denotes the slack tide before ebb.

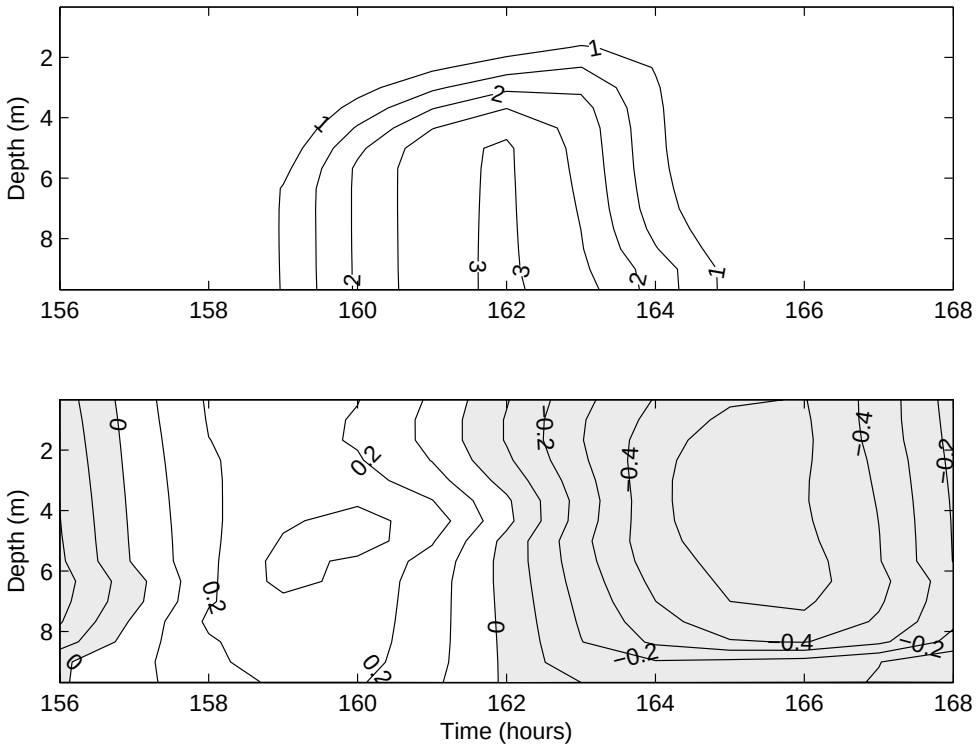

Figure 3 Time-depth contours of salinity and longitudinal velocity over a tidal cycle at x=13 km. Upper panel: salinity contours (psu). Lower panel: longitudinal current (m s^{-1}). Positive values are flood.

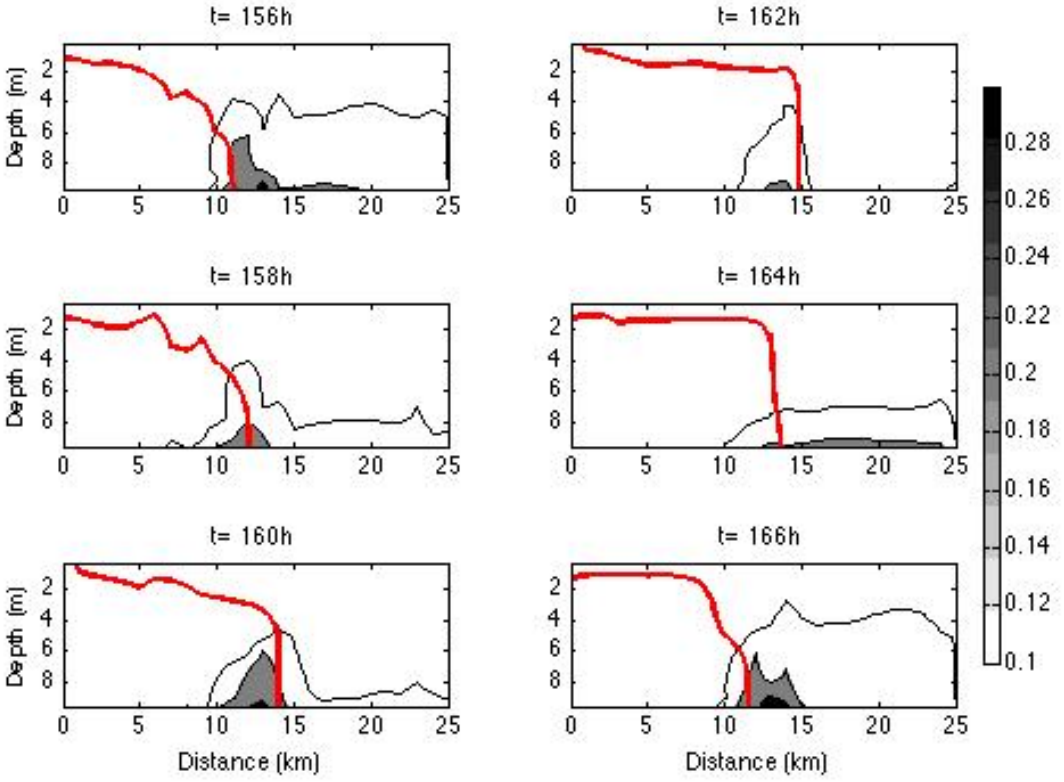

Figure 4 Instantaneous SSC distributions with contours of 0.1, 0.2, and 0.3 kg m^{-3} (solid lines) from hour 156 to 166 for Run 1 (no flocculation). The red line represents 1 psu isohaline (the salt front).

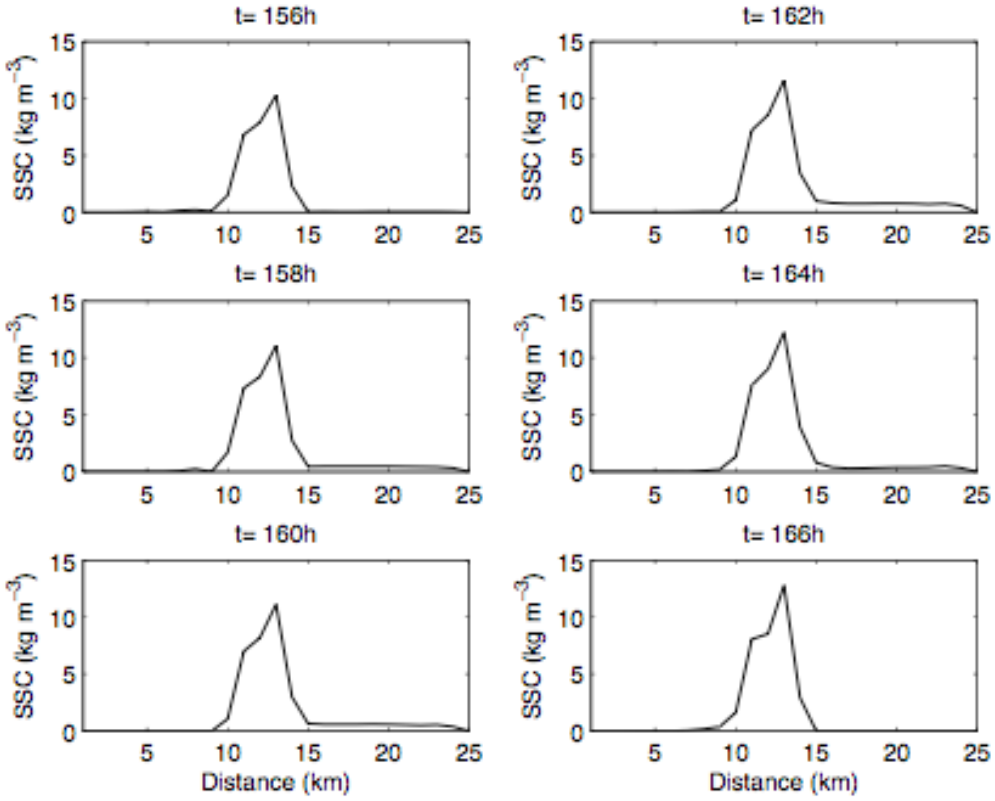

Figure 5 Bottom sediment concentrations from hour 156 to 166 for Run 1 (no flocculation).

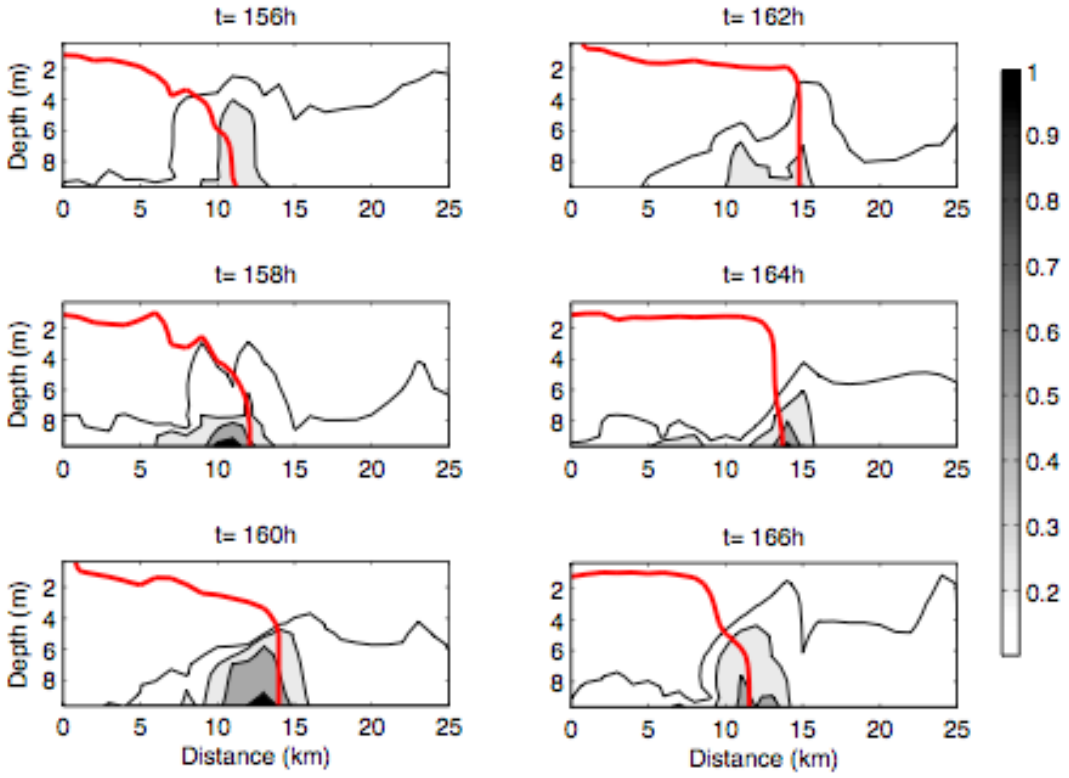

Figure 6 Instantaneous SSC distributions with contours of 0.1, 0.2, 0.5, and 1 kg m^{-3} (solid lines) from hour 156 to 166 for Run 2 (with flocculation). The red line is 1 psu isohaline.

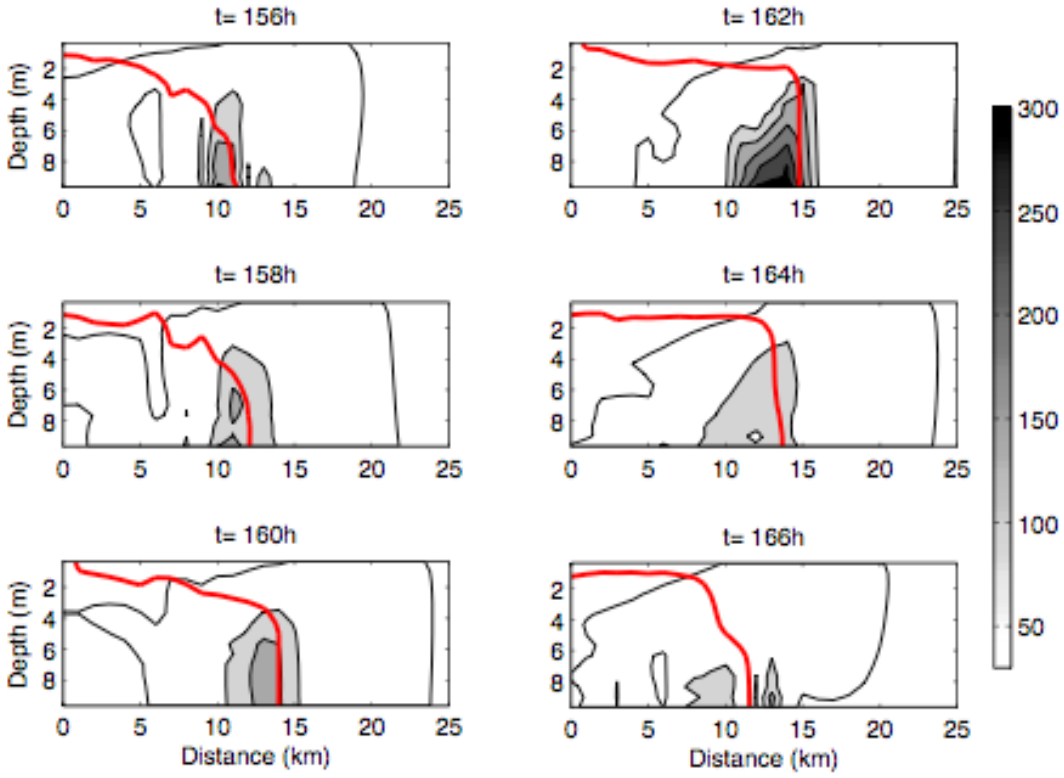

Figure 7 Instantaneous median floc size (D_{50}) contours (contour interval = 50 μm) for Run 2 (with flocculation) at the same times as Fig. 5. The background D_{50} is about 50 μm. The red line is 1 psu isohaline.

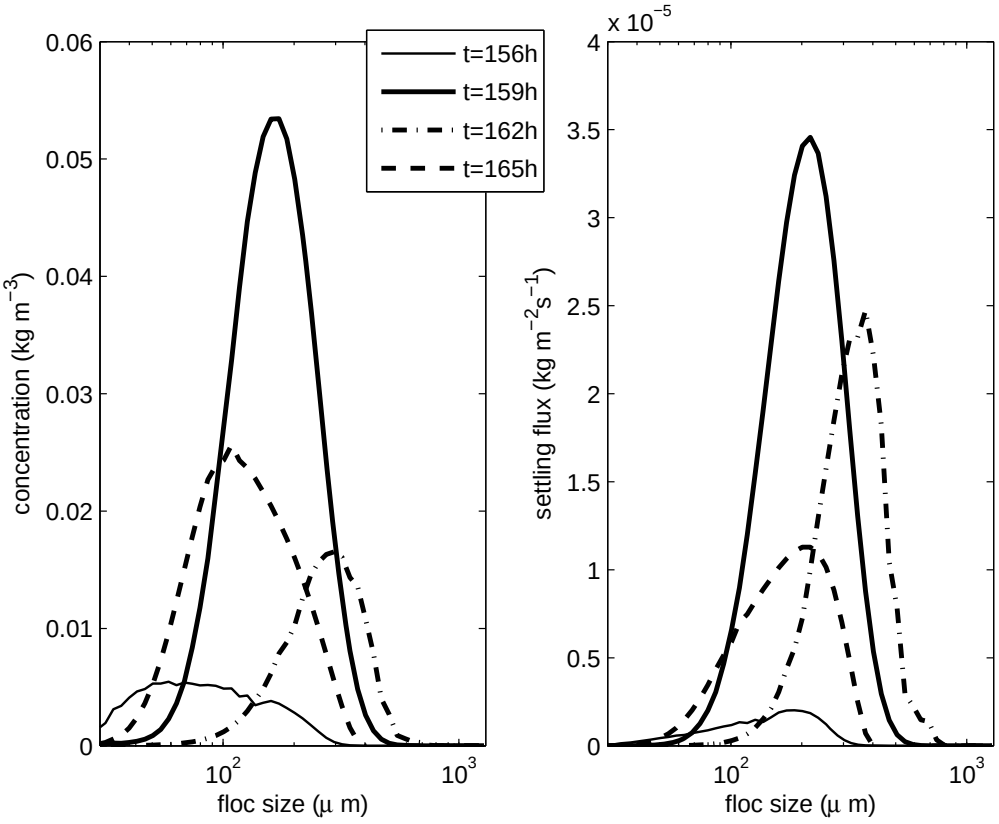

Figure 8 (left) Floc size distributions of mass concentration, and (right) settling flux of flocs at different tidal phases at 1.7 mab, x=13 km.

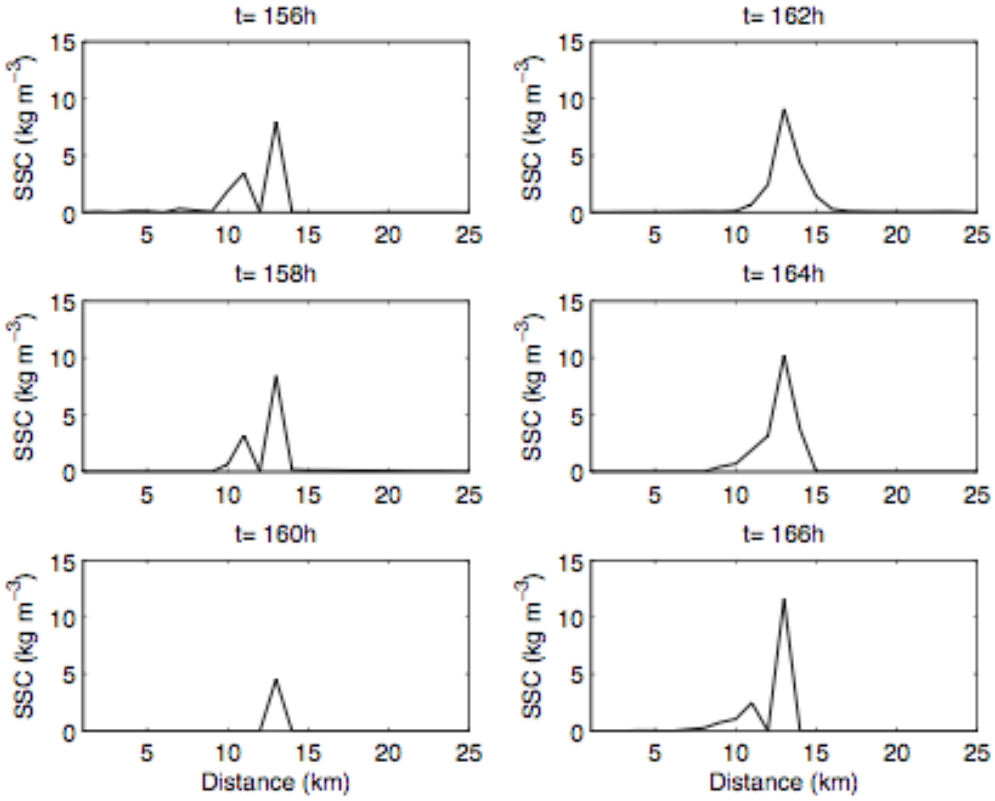

Figure 9 Instantaneous bottom sediment concentrations from hour 156 to hour 166 for Run 2 (with flocculation).

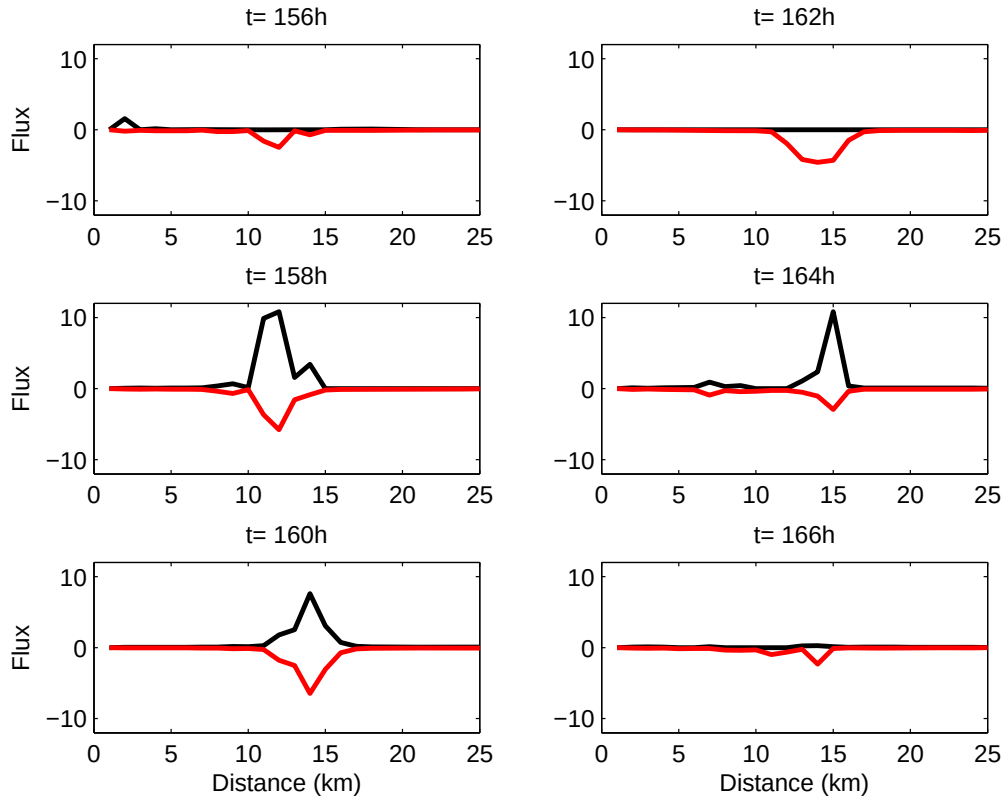

Figure 10 Instantaneous resuspension flux (black) and deposition flux (red) at the water-bed interface from hour 156 to hour 166 for Run 2. The flux unit is in 10^{-4} kg $m^{-2}s^{-1}$.

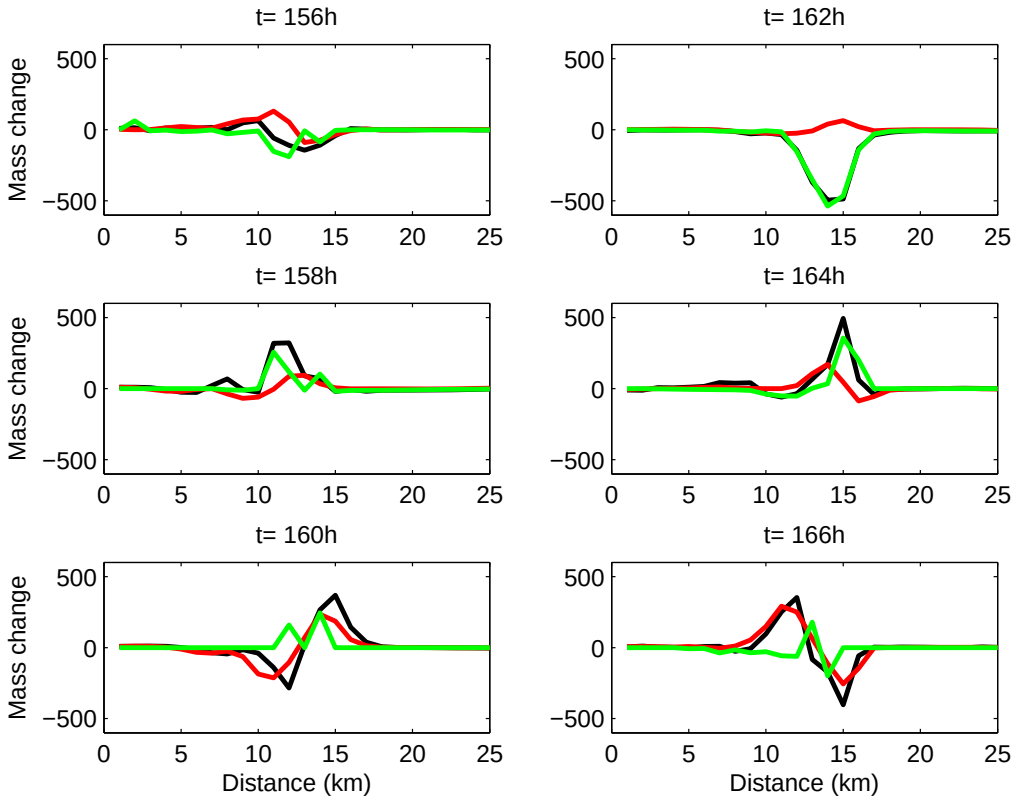

Figure 11 Instantaneous along-channel suspended sediment budget from hour 156 to hour 166 for Run 2 (with flocculation). The black line denotes time rate of change, the red line denotes horizontal advection and the green line denotes deposition/erosion. The mass change unit is in kg s^{-1}.

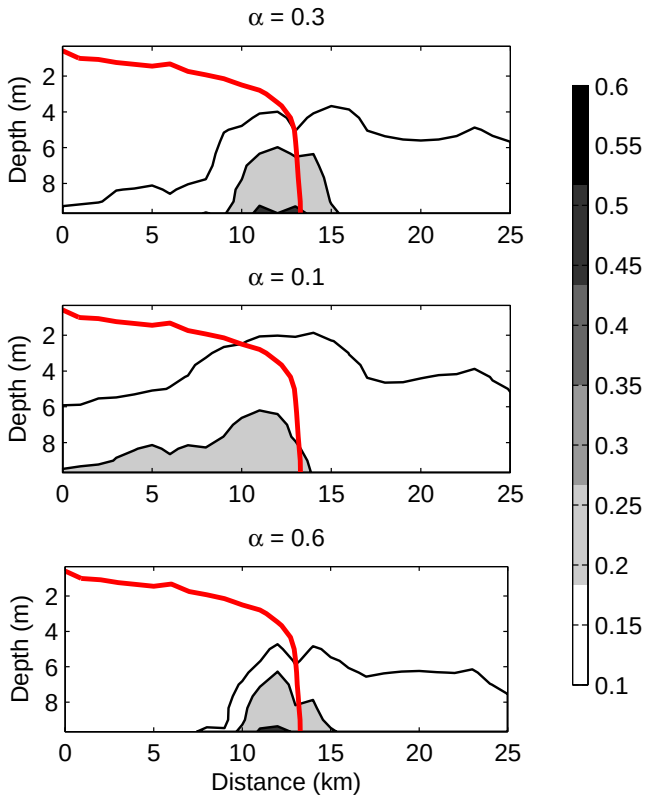

Figure 12 The tidally-averaged 1 psu isohaline (thick solid line), and SSC contours (solid lines) for different particle stickiness, 0.3 (Run 2), 0.1 (Run 4), and 0.6 (Run 5).

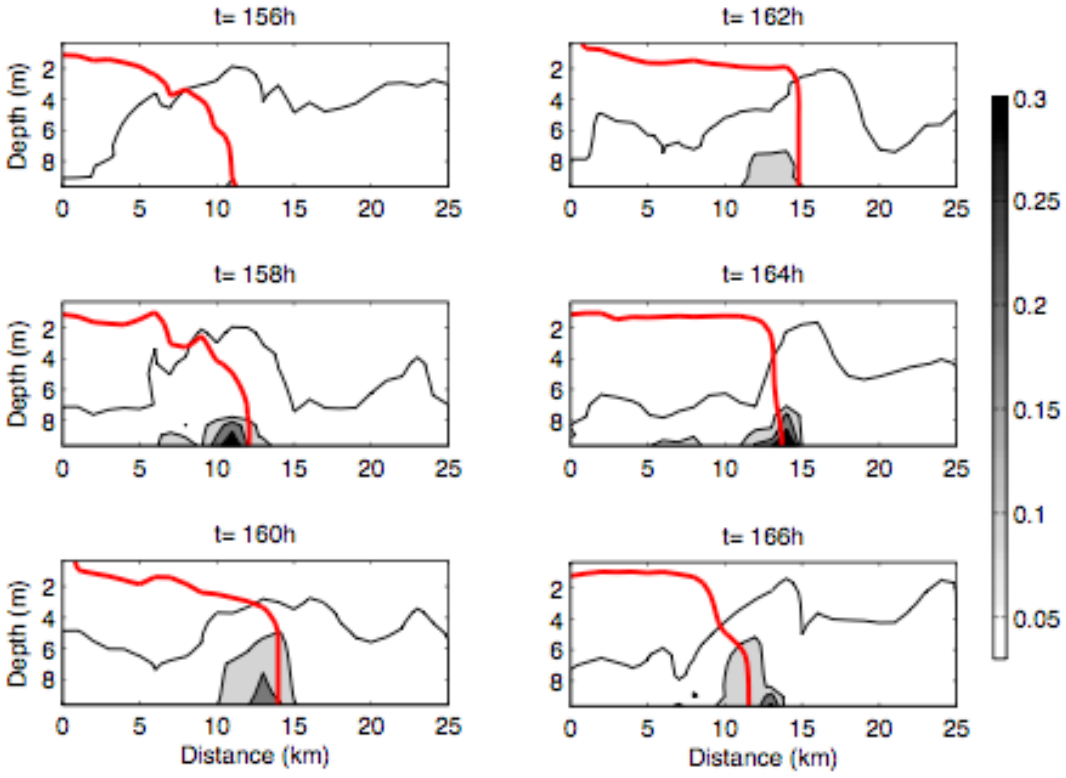

Figure 13 Instantaneous SSC with contours of 0.03, 0.1, 0.2, and 0.3 kg m^{-3} (solid lines) from hour 156 to 166 for Run 6. The red line is 1 psu isohaline.

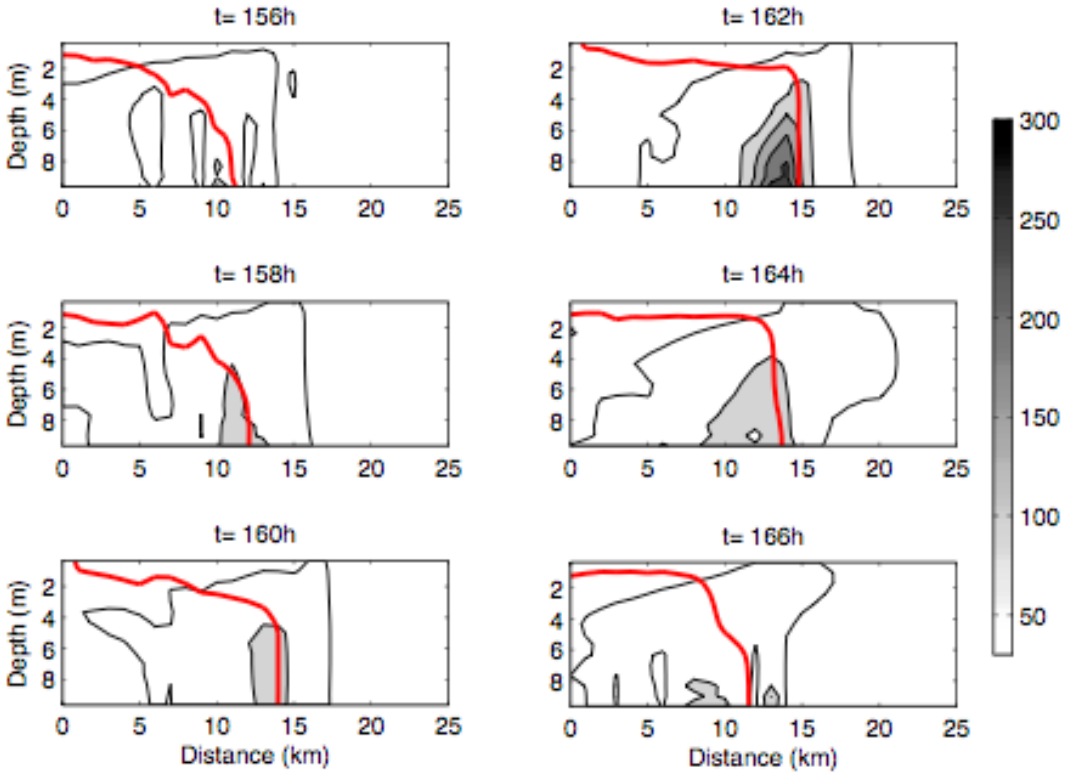

Figure 14 Instantaneous median floc size (D_{50}) contours (contour interval = 50 μm) at the same time as Fig. 15 for Run 6. The background D_{50} is about 50 μm. The red line is 1 psu isohaline.

Chapter 4

Flocculation effects on lateral trapping of fine-grained sediment in an idealized partially mixed estuary

4.1 Introduction

A region characterized by elevated suspended sediment concentrations, referred to as an estuarine turbidity maximum (ETM), is often present in the upper or middle portions of the salt intrusion in estuaries, e.g. the upper Chesapeake Bay (Sanford et al., 2001) and the Hudson River estuary (Geyer et al., 1998). Various mechanisms contribute to development of an ETM, including river discharge, tidal currents, stratification, estuarine circulation, and geometry (Postma, 1967). In addition to these along-channel mechanisms, lateral circulation, despite its magnitude of only about 10% of the along-channel flow, is recognized as an important factor for the along-channel sediment budget and cross-channel sediment dispersal (Lerczak and Geyer 2004; Fugate et al. 2007; Kim and Voulgaris, 2008). Flocculation of fine-grained particles is another important factor for particle trapping in an ETM (Sanford et al., 2005). However, the role of flocculation in the lateral sediment trapping remains unclear. In the study, we use a numerical model to explore the effects of lateral circulation associated with flocculation on cross-channel distribution of suspended sediment.

In general, mechanisms driving lateral circulation in estuaries include Coriolis force (e.g. Ott and Garrett, 1998), centrifugal force in a curved channel (e.g. Chant, 2002),

cross-channel density gradient induced by differential advection of along-channel salinity gradient (e.g. Lerczak and Geyer, 2004), cross-channel bathymetric variability (e.g. Valle-Levinson, 2008), and boundary mixing on a sloping bottom (e.g. Chen and Sanford, 2009). These mechanisms may reinforce or cancel each other depending on local estuarine environments (Kim and Voulgaris, 2008). For example, Kim and Voulgaris (2008) presented observations in Winyah Bay, USA, showing that during flood tides the centrifugal acceleration and the Coriolis force favor the clockwise lateral flow (looking into the estuary), which is further reinforced by lateral baroclinic pressure gradient, while during ebb the lateral flow is much weaker due to the interaction between the centrifugal force and the opposite-directed Coriolis force and lateral baroclinic gradient.

The aforementioned mechanisms contributing to lateral sediment transport have been explored via some observational (Geyer et al., 1998; Fugate et al., 2007; Kim and Voulgaris, 2008) and numerical studies (Geyer et al., 1998; Huijts et al., 2006; Chen and Sanford, 2009). Geyer et al. (1998) observed an ETM skewed toward the western side of the Hudson River estuary, which they used a numerical simulation to illustrate that the lateral convergence on flood and the longitudinal convergence on ebb are mainly responsible for the ETM formation. On the contrary, Fugate et al. (2007) found sediment was more trapped on the eastern side of the upper Chesapeake estuary, presumably due to the tidal asymmetry in lateral circulation, stratification, and resuspension. The difference in particle trapping between these two estuaries can be attributed to the competition between Coriolis force and friction influences (Huijts et al., 2006), which suggests that in response to Coriolis force sediments tend to concentrate on the east side under small friction, but on the west side with increasing friction.

The influence of flocculation which can cause significant temporal and spatial variations in particle size and settling velocity, has not been considered in the studies on lateral sediment transport. The objective of the study is to explore the interaction of lateral flow and flocculation on fine-grained sediment trapping in an idealized partially-mixed estuary. We implement a flocculation scheme (Xu et al., 2008) into the Princeton Ocean Model (POM), and perform numerical experiments of an idealized partially-mixed estuary in a three-dimensional (*x*-*y*-*z*) domain. The manuscript is organized as follows: Section 2 presents a description of sediment transport model and simulation setup. The results of the idealized experiments are presented and discussed in section 3 and 4. We conclude in section 5.

4.2 Model description

We use the Princeton Ocean Model (POM) (Blumberg and Mellor 1987; Mellor 1998) coupled with a size-resolved flocculation scheme and a sediment transport component to simulate suspended sediment flocculation and transport processes in Chapter 2 and 3. The model domain is configured as a straight channel with 25 km long from north to south and 1 km wide from west to east, and the bottom has a parabolic shape with maximum depth of 15 m in the center and minimum depth of 5 m at the sides. The grid configuration is 26 (along-channel) × 13 (cross-channel) × 16 (vertical sigma levels). At the two open ends, a constant river discharge plus a barotropic, semidiurnal (T = 12 hour) tidal forcing is specified, $\bar{u} = -0.1 + 0.4\sin(2\pi t/T)$ (m s^{-1}). Radiation conditions are used for the outgoing waves. Temperature is fixed at 15 ^{o}C in the domain. The longitudinal salinity distribution is initialized with $s(x) = 5(1 + \tanh(0.2(L_x/2 + 5 - x)))$ (psu), where L_x is channel length and x is the distance from the estuary mouth in km. The

inflow salinity is specified at 0 psu at the north end and 10 psu at the south end. No-slip condition is used at the lateral boundaries. Considering the effects of earth rotation, the Coriolis parameter is set to be 8.8×10^{-5} s^{-1} for mid latitude of the Northern Hemisphere.

The model solves the equation for the time variation of mass concentration in each particle size bin,

$$\frac{\partial C_j}{\partial t} + u\frac{\partial C_j}{\partial x} + v\frac{\partial C_j}{\partial y} + w\frac{\partial C_j}{\partial z} - \frac{\partial w_{s,j} C_j}{\partial z} = \frac{\partial}{\partial z}\left(K_3 \frac{\partial C_j}{\partial z}\right) + flocculation, \qquad (1)$$

where u, v, and w are the lateral, longitudinal, and vertical velocity respectively, $w_{s,j}$ is the particle settling velocity in the bin j, and K_3 is the vertical eddy diffusivity. Equation (1) describes the change in suspended sediment concentration (SSC) due to longitudinal, lateral, and vertical advection, turbulent diffusion, particle settling, and flocculation. Flocculation is solved via the size-resolved flocculation scheme (Xu et al., 2008). The Smagorinsky scheme is used for horizontal diffusion with a constant coefficient of 0.2. The model is fully coupled so that u, v, w, K_3 and ε are predicted by POM; the Mellor-Yamada level 2.5 turbulence closure (Mellor and Yamada, 1974) is used. The particle mass flux from bottom erosion $E_{s,j}$ in bin j is described as:

$$K_3 \frac{\partial C_j}{\partial z}\bigg|_{bottom} = E_{s,j} = E_{0,j}\left(\frac{\tau_b}{\tau_c} - 1\right)/i, \quad \text{when} \quad \tau_b > \tau_c \qquad (2)$$

where $E_{0,j}$ is a bed erodibility constant, assumed to be 1×10^{-3} kg m^{-2} s^{-1} for all size ranges. The bin number j in the denominator is used to account for the fact that larger particles are more difficult to erode than smaller ones. This expression for erosion flux has been successfully used in Xu et al. (2008). The bed shear stress $\tau_b = \rho C_d v\sqrt{u^2 + v^2}$, where ρ is the reference density, 1025 kg m^{-3}. τ_c is the critical shear stress for erosion and is set to

0.05 pa in the study. Considering the rapid tidal phase change, the consolidation process is neglected (Uncles et al., 2006).

The model runs from rest until the circulation reaches a quasi-periodic state. Then, a vertically well-mixed constant loading of suspended primary particles, 0.1 kg m^{-3}, is imposed at the east boundary. The size of primary particle is 30 μm, which is the typical size of robust microflocs present in estuaries, like the upper Chesapeake Bay (Sanford et al. 2005). The total bin number *n* is set to be 50. Thus, the size of flocs can vary in 30-1277 μm, which includes most of the floc size range in estuaries. The external and internal time steps for the circulation model are 1 s and 5 s, respectively, and for the flocculation, 0.25 s is used. The SSC also will reach a quasi-periodic state. One-size flocculation simulation and size-resolved flocculation simulation are done to explore the influence of flocculation on lateral sediment trapping.

4.3 Model results

4.3.1 Salinity and circulation pattern

Figure 1 shows the tidally averaged along-channel velocity and salinity distributions along the channel axis, which are typical of a partially mixed estuary (e.g. Chant, 2002; Geyer et al., 1998). A well-defined salt front (defined as 1 psu isohaline) is located around x = 14 km with a top to bottom salinity difference of about 7 psu. The along-channel velocity exhibits a two-layered circulation pattern with landward flow near bottom and seaward flow near surface. The residual flow converges near the salt front. Two cross-sections are selected to exhibit the typical lateral circulation pattern at moderately-stratified and well-mixed conditions. One is located seaward of the salt front (x = 7.5 km), and the other landward of the salt front (x = 21.5 km). They are located

apart from the salt front to reduce the influence of the rapidly changing along-channel salinity gradient.

Maximum flood and ebb tides occur at hour 111 and 117, respectively. At x = 7.5 km, during flood along-channel currents reach a maximum velocity of 0.6 m s^{-1} at depth of 10 m (Fig. 2a), whereas during ebb maximum currents (-0.7 m s^{-1}) are present near the surface (Fig. 2c). This tidal current asymmetry is mainly resulted from the interaction of the tidal currents with the estuarine circulation. At hour 114 and 120, the currents are much weaker approaching slack tides (Fig. 2b and 2d).

During flood (hour 111), the isohalines tilt down to the left (looking into the estuary in the Northern Hemisphere), setting up a cross-sectional baroclinic pressure gradient (Fig. 2e). In the deep part of the water column, water is saltier at the center than at the banks, induced by differential advection of along-channel salinity gradient. The titling isohaline is slightly relaxed at slack tide after flood (Fig. 2f) due to the reduced along-channel velocity. During ebb, the surface water becomes less salty at the center than at the banks. The isohalines still tilt down to the left (Fig. 2g and 2h) to maintain the thermal wind balance with ebbing currents.

The lateral flow exhibits a three-layer structure during flood (hour 111, Fig. 2a). Surface and bottom currents are divergent and currents are convergent at mid-depth (6 ~ 10 m). The lateral flow is stronger on the left side of the channel (looking into the estuary), with maximum lateral currents of 2.7 cm s^{-1}. The lateral circulation pattern at hour 114 is the same as that at hour 111, but the maximum lateral currents decrease to 1.0 cm s^{-1} due to decreasing of along-channel velocity (Fig. 2b). During ebb, the lateral circulation shows a two-layer structure with divergent flow near the surface and

convergent flow in the deep water (Fig. 2c and 2d), with maximum lateral currents of 3.4 cm s^{-1} on the left side.

In order to explore the influence of Earth rotation, we carry out a simulation without rotation by setting Coriolis parameter to zero. When rotation is excluded, the lateral circulation pattern is similar to the previous run, except that lateral circulation and salinity are symmetric along the channel axis (Fig. 3). Hence, the enhancement of lateral circulation on the left side of the channel for the simulation with rotation is driven by Coriolis forcing.

Lerczak and Geyer (2004) have carried out simulation of lateral circulation in a straight estuary under various stratification conditions. For their model run with strong stratification (ΔS = 9.22 psu), a lateral circulation was observed in the lower half of the water column during flood, with convergent flow at the mid-depth, divergent flow near bottom, and maximum bottom currents of 4.6 cm s^{-1}. During ebb, a weak lateral circulation with divergent near the surface and convergent near the bottom was shown. Our lateral circulation patterns are generally consistent with their results, except that the surface circulation shows a persistent divergent flow at the surface through the tidal cycle.

The combination of barotropic and baroclinic pressure gradient mainly drives the lateral circulation. Due to the variation in cross-channel bathymetry, the water surface is higher in the middle of the channel than over the bank. The resulting sideward directed barotropic pressure gradient drives a divergent lateral motion near the surface. The baroclinic pressure gradient, which is caused by differential advection, on the other hand, is towards the sidewall (higher salinity over the shoal than at the center) during ebb and is towards the center during flood. Also, the lateral density gradient has strong depth

dependency. The lateral density gradient is confined in the lower water column during flood when tidal currents are strong near the bottom (Fig. 2e-f), whereas it is concentrated in the upper water column during ebb when tidal currents are strong near the surface (Fig. 2g-h). Consequently, near the surface, currents are always divergent, and are stronger during ebb when barotropic and baroclinic pressure gradients are in concert. In the lower water column, the opposing baroclinic pressure gradient is dominant during flood, resulting in divergent currents near bottom and return currents at mid-depth. In addition, the Coriolis force introduces bottom Ekman veering, clockwise during flood and counterclockwise during ebb. This enhances on the left side of the channel the clockwise circulation in the lower layer during flood and counterclockwise circulation in the upper layer during ebb.

Landward of the salt front (x = 21.5 km), the water is nearly fresh (salinity structure not shown). The along-channel velocity is high (0.3 m s^{-1}) towards the surface on flood, and is maximum (-0.5 m s^{-1}) in the center of the channel on ebb (Fig. 4). Without the influences of salt, the lateral circulation is dominated by bottom Ekman veering (Fig. 4). The maximum lateral flow is 1.3 cm s^{-1} on flood and 0.9 cm s^{-1} on ebb.

4.3.2 Sediment trapping for one-size flocculation simulation

In the one-size flocculation simulation, a constant settling velocity of particles, 0.35 mm s^{-1} (equivalent floc size 127 μm and a floc density of 1030 kg m^{-3}), is used in order to form an ETM (Xu et al., 2009). The salinity and circulation patterns are the same as described in the previous section. Figure 5 shows snapshots of 1 psu isohaline and longitudinal distributions of SSC along the channel axis at the same four tidal phases as in Fig. 2. Landward of the salt front, SSC is about 0.05 kg m^{-3}. Suspended sediments are

trapped near the salt front, and moving with the tidal currents. Note that the salt front leads the center of the ETM in the direction of tidal flows, due in part to the resuspension lag. The maximum SSC (~ 0.3 kg m^{-3}) occurs on maximum flood and ebb. Low SSC (0.1 kg m^{-3}) is found at slack tides before ebb (at hour 114). Both longitudinal flow convergence and tidal resuspension contribute to the formation of the ETM. This result is basically similar to the two-dimensional case in Chapter 3.

The temporal and spatial variations of near bottom (one sigma level above the bottom) SSC are shown in Fig. 6. As expected, high SSC is observed at maximum flood and ebb, and decreases with decreasing currents. The SSC distribution is nearly symmetric along the channel axis. The longitudinal flow convergence has a strong impact on the sediment trapping near the salt front. At maximum flood and ebb (hour 111 and 117), the convergence is stronger in the thalweg than over the bank, leading to higher concentrations in the channel center than over the adjacent shoals. On the other hand, at hour 114 elevated concentrations occur near shoals due to cross-channel redistribution of suspended sediment by lateral advection. To examine the lateral variations, cross sections are selected at x = 12.5, 14.5, 13.5, and 10.5 km respectively for the four different tidal phases, following approximately the maximum along-channel SSC. These cross-sectional distributions of SSC are shown in Fig. 7. During flood (hour 111), near bottom SSC is relative high (~ 0.4 kg m^{-3}), with slightly higher SSC on the left bank due to larger lateral flow (Fig. 2a). In the following slack tide (hour 114), the dominant deposition process causes low SSC in the water column and favors sediment accumulation at the bed. The up-slope lateral flow transport suspended sediment toward the sidewalls, resulting in relative high SSC on banks. During ebb (at hour 117), SSC increases to about 0.4 kg m^{-3}

due to resuspension and flow convergence near the deepest bottom. At hour 120, bottom flooding currents (Fig. 2d) favor resuspension and diffusion, leading to increasing of SSC in the middle of the water column. Noticeably, slightly higher SSC is observed over the left shoals than over the right caused by asymmetry in lateral flows.

4.3.3 Sediment trapping for size-resolved flocculation simulation

In the size-resolved flocculation simulation, the model setup is identical to the previous simulation except with evolution of floc size with flocculation included. A pronounced ETM is formed near the salt front (Fig. 8). Background value of SSC is about 0.05 kg m^{-3}. In the ETM region, the SSC increases to 0.55 kg m^{-3} at maximum flood (hour 111), or about twice as large as in the one-size flocculation case. With the decreasing of currents, most of sediments are settled toward the bottom (hour 114). In the following ebb currents, the previous deposited sediments are resuspended. The SSC increases to more than 0.45 kg m^{-3} (hour 117). Approaching the slack tide, the SSC decreases again due to deposition and moves seaward with ebbing currents (hour 120).

Figure 9 shows along-channel distributions of median floc size (D_{50}) at the same four tidal phases as in Fig. 8. The background median particle size is about 50 μm. Large flocs (>100 μm) are formed near the salt front due to convergence of suspended particles. At hour 111, maximum floc size (~ 250 μm) is present at mid-depth seaward of the salt front due to reduced turbulence near the pycnocline. At subsequent slack tide, although the SSC is decreasing, the median floc size is still about 150 μm due to low turbulence and differential settling near the salt front. At maximum ebb (hour 117), despite large SSC, the floc size is only about 50 μm near the salt front due to the dominance of breakup process induced by high turbulence. On the contrary, seaward of the salt front

stratification creates flocs with size close to 100 μm. At hour 120, floc size increases up to 250 μm seaward of the salt front due to reduced turbulence and local resuspension. The variation in median floc size with tidal currents is consistent with previous studies (Chapter 2 & 3).

The temporal and spatial variations in near bottom SSC are shown in Fig. 10, taken at the same location and time as in in the one-size flocculation case. During flood (hour 111), SSC is nearly symmetric along the channel axis with maximum SSC of 0.8 kg m^{-3} over banks. In the following slack tide, SSC is reduced to about 0.2 kg m^{-3} by deposition. At maximum ebb (hour 117), more suspended sediment is evident over the left bank than over the right. At hour 120, ebbing currents advect SSC seaward with resuspension landward of the salt front. SSC tends to concentrate along the channel axis.

Noticeably, in contrast to the one-size flocculation case, at maximum currents high SSC is observed on banks instead of at the center. For the one-size flocculation model run, the suspended sediment trapping is mainly controlled by longitudinal flow convergence. Because the gravitational circulation is stronger in deeper water depth, the flow convergence is stronger at the channel center. Hence more sediment tends to concentrate at the center than on banks. The instantaneous bottom shear stress however also is stronger at the channel center, as the longitudinal momentum balance is mainly between barotropic pressure gradient and vertical stress divergence. Because the floc size is dependent on shear stress, flocs are larger on banks than at the channel center in the flocculation model run. Consequently, settling flux is larger on banks than at the center. The interaction of longitudinal flow convergence, bottom flow divergence and flocculation contributes to the preferential sediment trapping on banks. Also, the left-

right asymmetry in sediment trapping is more pronounced than in the one-size flocculation case due to enhanced settling flux of suspended sediment induced by flocculation processes.

To investigate the lateral variations in SSC associated with flocculation, Figure 11 shows the cross-sectional SSC and median floc size distributions following the maximum SSC as in Fig. 7. The larger floc size, in the range of 100 ~ 300 μm, contributes to the enhancement of settling flux of suspended sediment, resulting in increasing of SSC for the flocculation simulation. Also, flocs are larger over the left shoals than over the right at maximum flood and ebb (at hour 111 and 117) due to slightly higher SSC over the left by lateral advection (Fig. 7). The larger floc size over the left shoals further enhances SSC. As a result, the cross-sectional asymmetry in SSC is reinforced by the positive feedback between SSC and floc size.

4.4 Discussion

We have shown the formation of an ETM for one-size flocculation and flocculation simulation. The SSC near the salt front is about 50% larger for flocculation simulation than one-size flocculation simulation. Also, a distinct flood-ebb asymmetry in sediment trapping, which is often observed in an ETM (e.g. Sanford et al., 2001), is found for the flocculation simulation. These results are similar to the previous 2-D simulation (Chapter 3), indicating that longitudinal flow convergence at the salt front is the dominant mechanism for an ETM formation. On the other hand, variations in bottom shear stress across the channel have profound effect on floc size distribution, resulting in larger SSC on banks in the flocculation simulation.

The lateral asymmetry in sediment trapping is enhanced by the flocculation processes. The floc size is slightly larger over the left bank than over the right (looking into the estuary) (Fig. 11), resulting in larger deposition flux on the left bank. Since resuspension only occurs when the critical bottom stress is exceeded, continuous deposition flux controls the bottom sediment accumulation. Therefore, flocculation processes reinforce the asymmetrical sediment accumulation on the slopes. This finding is consistent with commonly observed axially asymmetrical channel profiles in shallow and narrow estuaries, like the Hudson River estuary (Geyer et al., 1998) and the upper Chesapeake Bay (Fugate et al., 2007). So, the importance of flocculation for lateral sediment trapping is evident in the study. In our study, SSC is enhanced on the west side due to the interaction of lateral flows and flocculation processes.

The tidal asymmetry in lateral flow pattern is commonly observed in estuaries. For instance, lateral flow was stronger during ebb than flood in Snag Channel (Lacy and Monismith, 2001); in contrast, lateral flow was about 4 times stronger during flood than ebb in the Hudson River estuary (Lerzak and Geyer, 2004). The conflicting observational results suggest that the relative importance of forcing terms, like Ekman veering, cross-channel pressure gradient and centrifugal force, varies with estuarine environment. In our study, lateral flow is slightly stronger during ebb than flood. Also, Lerczak and Geyer (2004) observed a three-layer structure of lateral flow during neap tidal conditions (strong stratification) in the Hudson estuary. Surface and bottom currents were directed toward the flank whereas return currents were at the mid-depth along a strong pycnocline. A similar three-layer lateral circulation is found during flood in the model run.

4.5 Conclusion

In this numerical study, we have shown that the combination of lateral flow and flocculation processes affects lateral fine-grained sediment trapping in an idealized partially-mixed estuary. The enhancement of the preferential sediment deposition on left bank (looking into the estuary) for the size-resolved flocculation simulation underlines the role of flocculation in long-term formation of estuary channel profile. Furthermore, the development of a pronounced ETM near the salt front is facilitated by floc size variations. Hence, a realistic ETM simulation must include flocculation processes.

Many factors are not considered in the study, such as curved channels, laterally and longitudinally varying bathymetry, wind forcing, and limited sediment supply from bottom. They can complicate estuarine dynamics and flocculation processes. So, further investigation on these factors is necessary for longitudinal and lateral fine-grained sediment transport in estuaries.

References

Chant, R.J., 2002. Secondary circulation in a region of flow curvature: Relationship with tidal forcing and river discharge. *Journal of Geophysical Research*, 107, 3131, doi: 10.1029/2001JC001802.

Chen, S.N., Sanford, L.P., 2009. Lateral circulation driven by boundary mixing and the associated transport of sediments in idealized partially mixed estuaries. *Continental Shelf Research*, 29, 101-118.

Fugate, D.C., Friedrichs, C.T., Sanford, L.P., 2007. Lateral dynamics and associated transport of sediment in the upper reaches of a partially mixed estuary, Chesapeake Bay, USA. *Continental Shelf Research*, 27, 679-698.

Geyer, W.R., Signell, R.P., Kineke, G.C., 1998. Lateral trapping of sediment in a partially mixed estuary. In: Dronkers, J., Scheffers, M.B.A.M. (Eds.), Physics of Estuaries and Coastal Seas, Balkema.

Huijts, K.M.H., Schuttelaars, H.M., de Swart, H.E., Valle-Levinson, A., 2006. Lateral entrapment of sediment in tidal estuaries: An idealized model study. *Journal of Geophysical Research*, 111, C12016, doi: 10.1029/2006JC003615.

Kim, Y.H., Voulgaris, G., 2008. Lateral circulation and suspended sediment transport in a curved estuarine channel: Winyah Bay, SC, USA. *Journal of Geophysical Research*, 113, C09006, doi: 10.1029/2007JC004509.

Lacy, J.R., Monismith, S.G., 2001. Secondary currents in a curved, stratified, estuarine channel. *Journal of Geophysical Research*, 106, 31,283-31,302.

Lerczak, J.A., Geyer, W.R. (2004). Modeling the lateral circulation in straight, stratified estuaries. *Journal of Physical Oceanography*, 34, 1170-1428.

Ott, M.W., Garrett, C. (1998). Frictional estuarine flow in Juan de Fuca Strait, with implications for secondary circulation. *Journal of Geophysical Research*, 103, 15,657-15,666.

Sanford, L.P., Dickhudt, P.J., Rubiano-Gomez, L., Yates, M., Suttles, S.E., Friedrichs, C.T., Fugate, D.D., Romine, H., 2005. Variability of suspended particle concentrations, sizes, and settling velocities in the Chesapeake Bay turbidity maximum. In: Droppo, I.G., Leppard, G.G., Liss, S.N., Milligan, T.G. (Eds.), Flocculation in Natural and Engineered Environmental Systems, Boca Raton, Florida, CRC Press, pp. 211-236.

Sanford, L.P., Suttles S.E., Halka, J.P., 2001. Reconsidering the physics of the Chesapeake Bay estuarine turbidity maximum. *Estuaries*, 24, 655-669.

Scully, M.E., Friedrichs, C.T., 2007. Sediment pumping by tidal asymmetry in a partially mixed estuary, *Journal of Geophysical Research*, 112, C07028, doi: 10.1029/2006JC003784.

Uncles, R.J., Stephens, J.A., Law, D.J., 2006. Turbidity maximum in the macrotidal, highly turbid Humber Estuary, UK: Flocs, fluid mud, stationary suspensions and tidal bores, *Estuarine, Coastal and Shelf Science*, 67, 30-52.

Winterwerp, J.C., 1998. A simple model for turbulence induced flocculation of cohesive sediment, *Journal of Hydraulic Research*, 36, 309-326.

Xu, F., Wang, D.P., Riemer, N., 2008. Modeling flocculation processes of fine-grained particles using a size-resolved method: Comparison with published laboratory experiments, *Continental Shelf Research*, 28, 2668-2677.

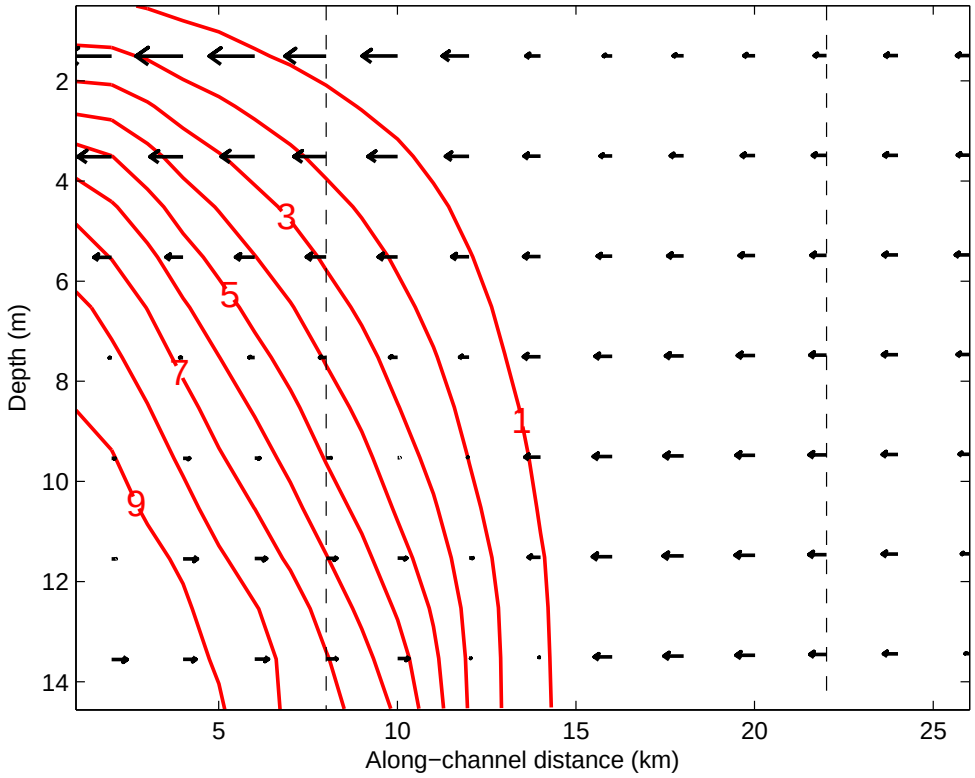

Figure 1 Tidally averaged salinity contours (red line) and velocity (arrow head) along the channel axis (depth = 15 m). Two locations (x = 7.5 and 21.5 km) are selected to show the cross sectional structure (dash line).

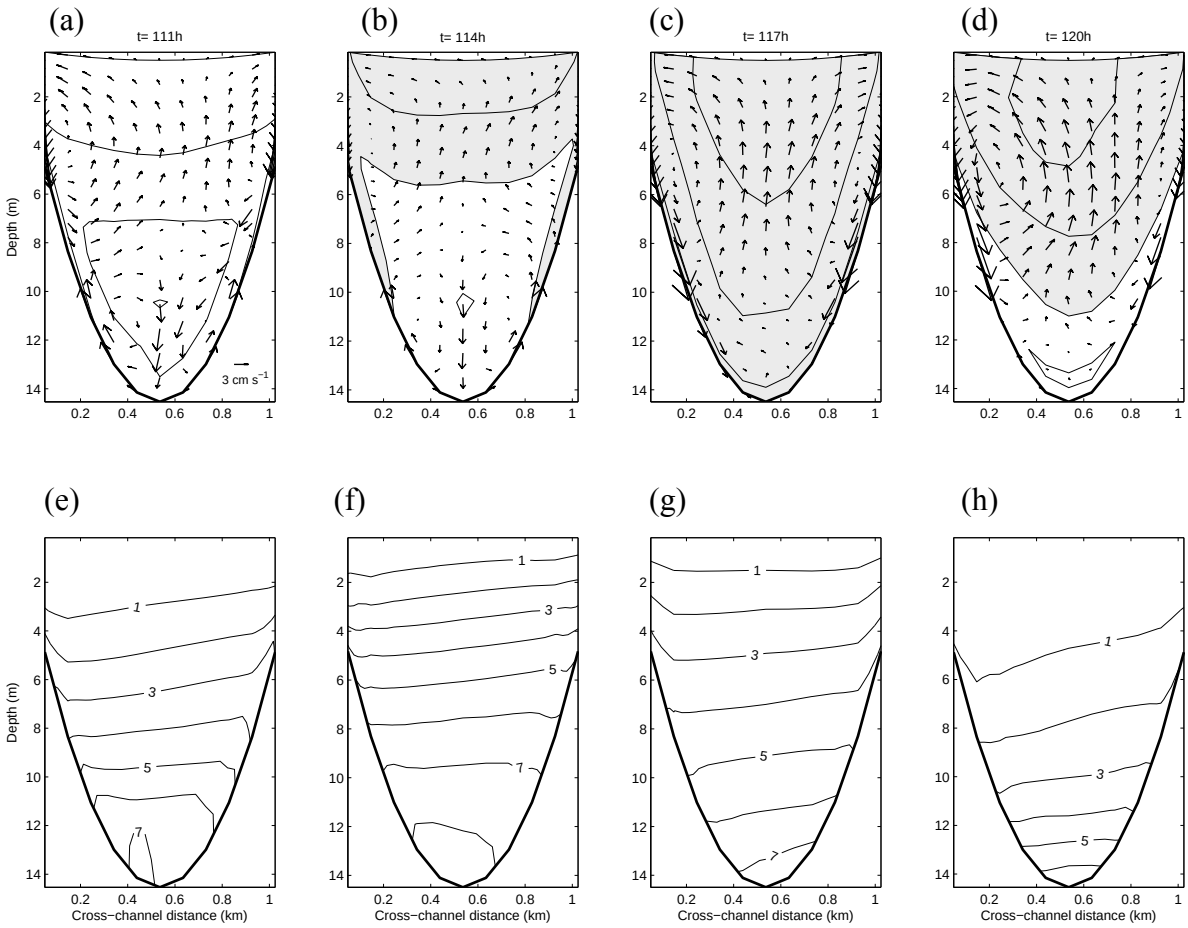

Figure 2 Upper panel: Cross-sectional profiles of along-channel velocity (contour interval in 0.2 m s^{-1}), and lateral velocity (arrow head), and lower panel: salinity contour from hour 111 to 120 for simulation with Earth rotation. The hour 111 denotes maximum flood, and hour 117 denotes maximum ebb. Ebbing currents (directed out of the page) are shaded gray. The cross section is at 7.5 km. All of the cross-sectional profiles presented in the study are looking into the estuary. The magnitude of vertical velocity is exaggerated 1000 times. Positive velocities are flood.

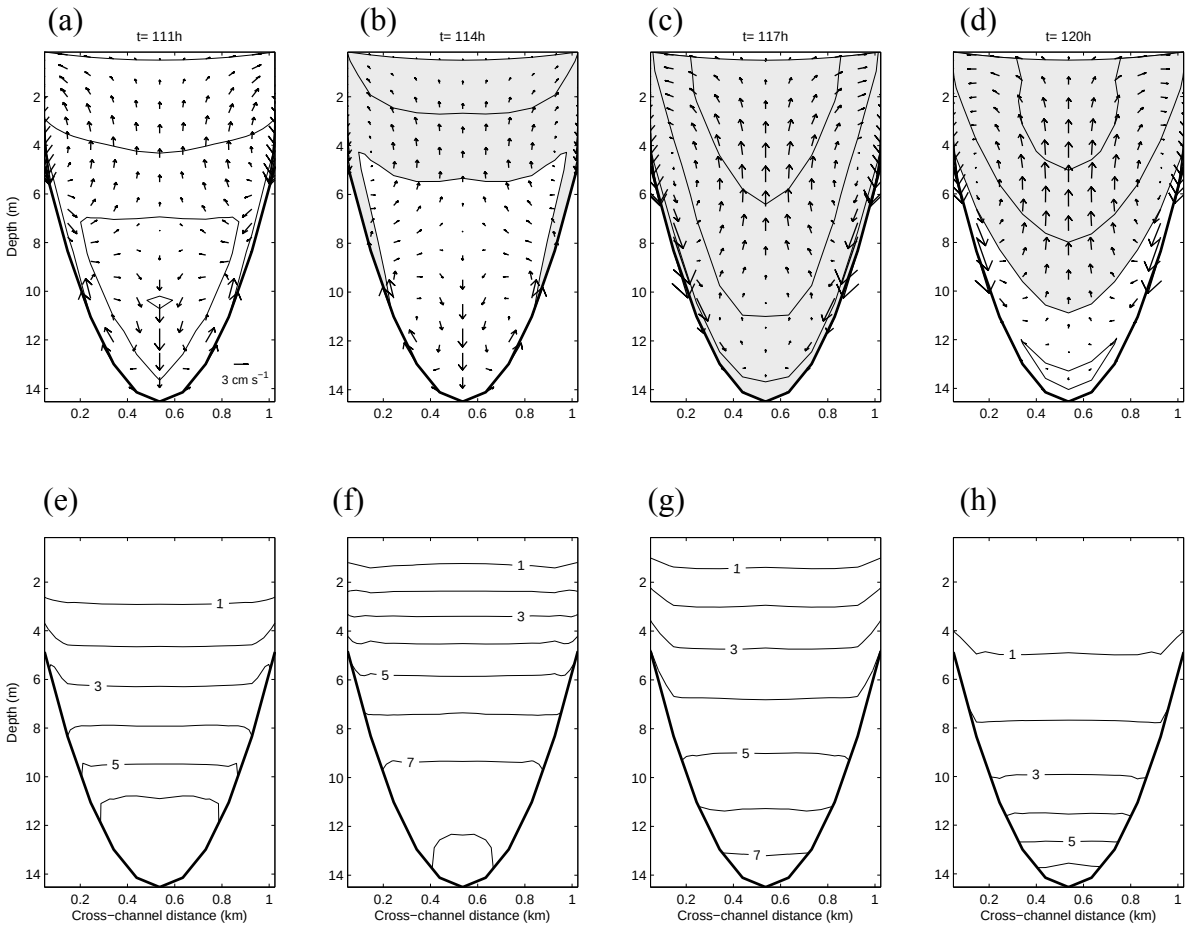

Figure 3 Upper panel: Cross-sectional profiles of along-channel velocity (contour interval in 0.2 m s^{-1}), and lateral velocity (arrow head), and lower panel: salinity contour from hour 111 to 120 for simulation without Earth rotation. The hour 111 denotes maximum flood, and hour 117 denotes maximum ebb. Ebbing currents (directed out of the page) are shaded gray. The cross section is at 7.5 km. All of the cross-sectional profiles presented in the study are looking into the estuary. The magnitude of vertical velocity is exaggerated 100 times. Positive velocities are flood.

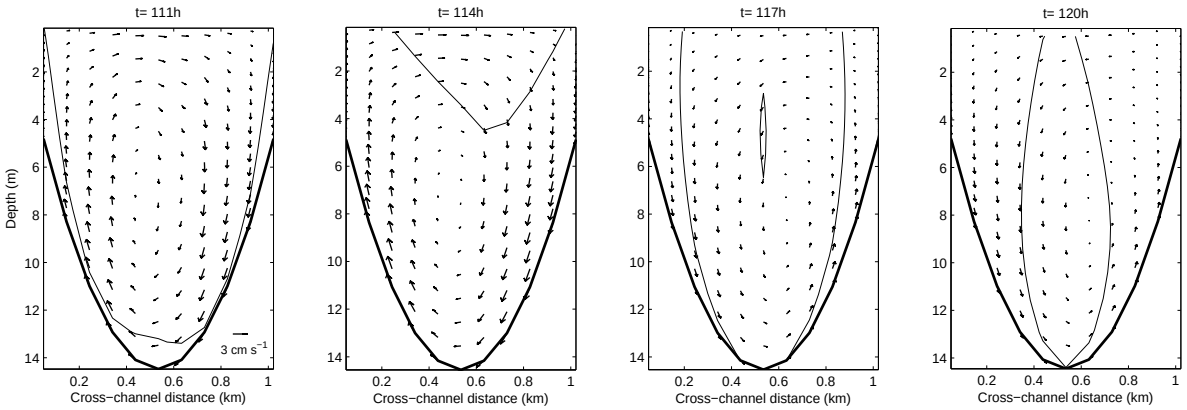

Figure 4 Cross-sectional profiles of along-channel currents (contour interval in 0.1 m s^{-1}), and lateral velocity (arrow head) for simulation with Earth rotation. The hour 111 denotes maximum flood, and hour 117 denotes maximum ebb. The cross section is at 21.5 km.

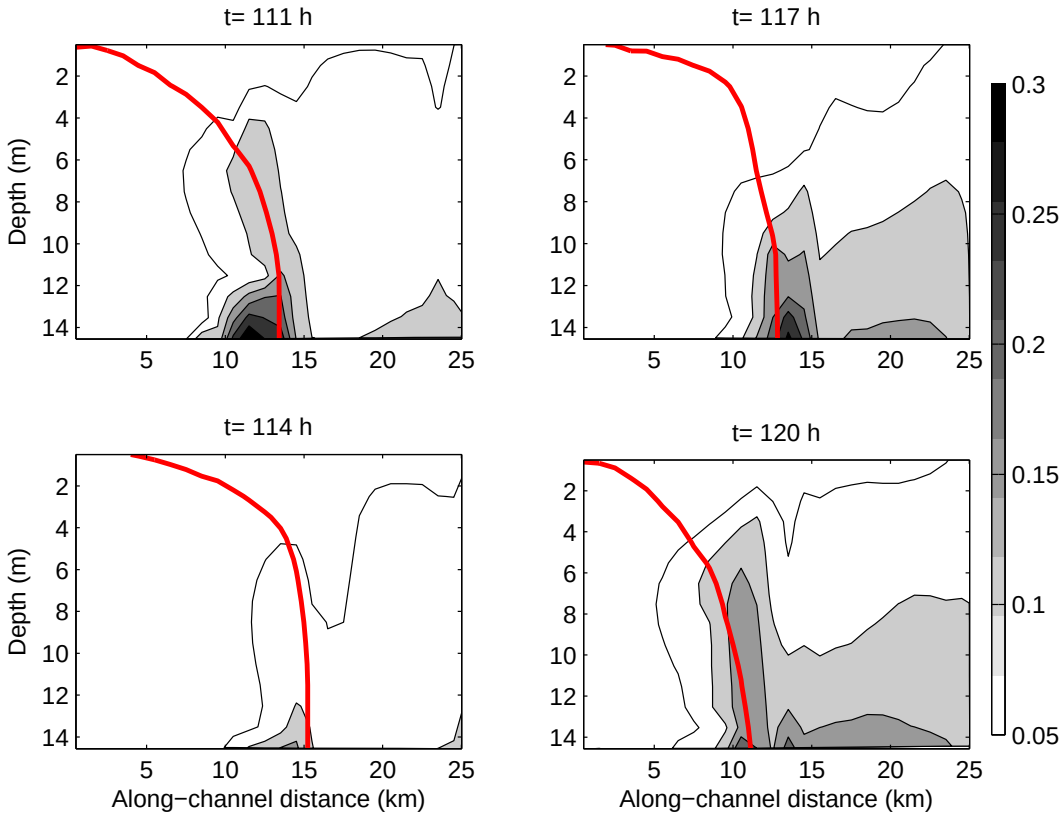

Figure 5 Instantaneous SSC distributions with contour interval 0.05 kg m^{-3} (solid lines) from hour 111 to 120 for one-size flocculation simulation with Earth rotation. The red line represents 1 psu isohaline (the salt front).

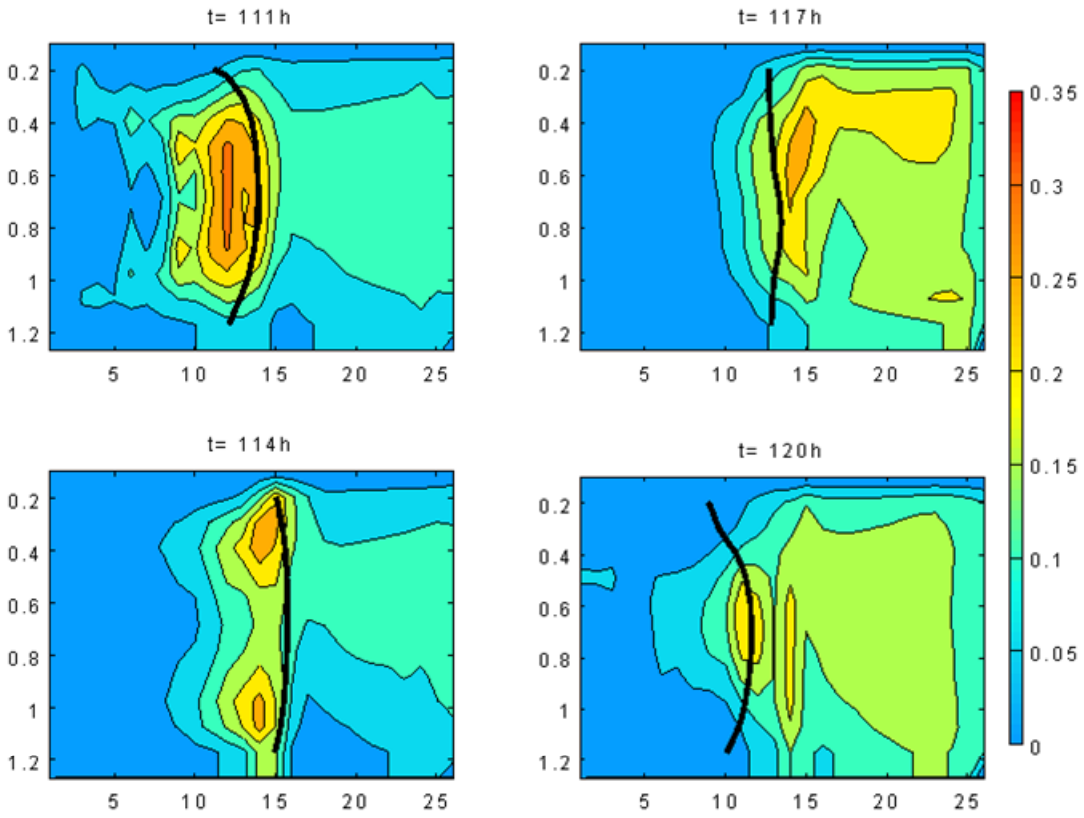

Figure 6 Instantaneous near bottom SSC distributions from hour 111 to 120 for one-size flocculation simulation with Earth rotation. The black line represents 1 psu isohaline (the salt front).

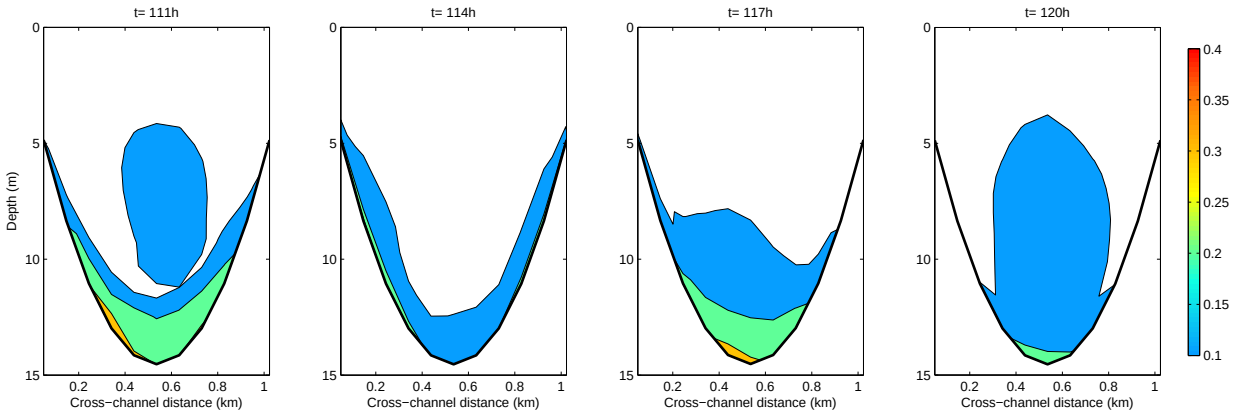

Figure 7 Cross sectional SSC distributions with contour interval 0.05 kg m^{-3} following the maximum SSC from hour 111 to 120 for one-size flocculation simulation with Earth rotation. The hour 111 denotes maximum flood, and hour 117 denotes maximum ebb.

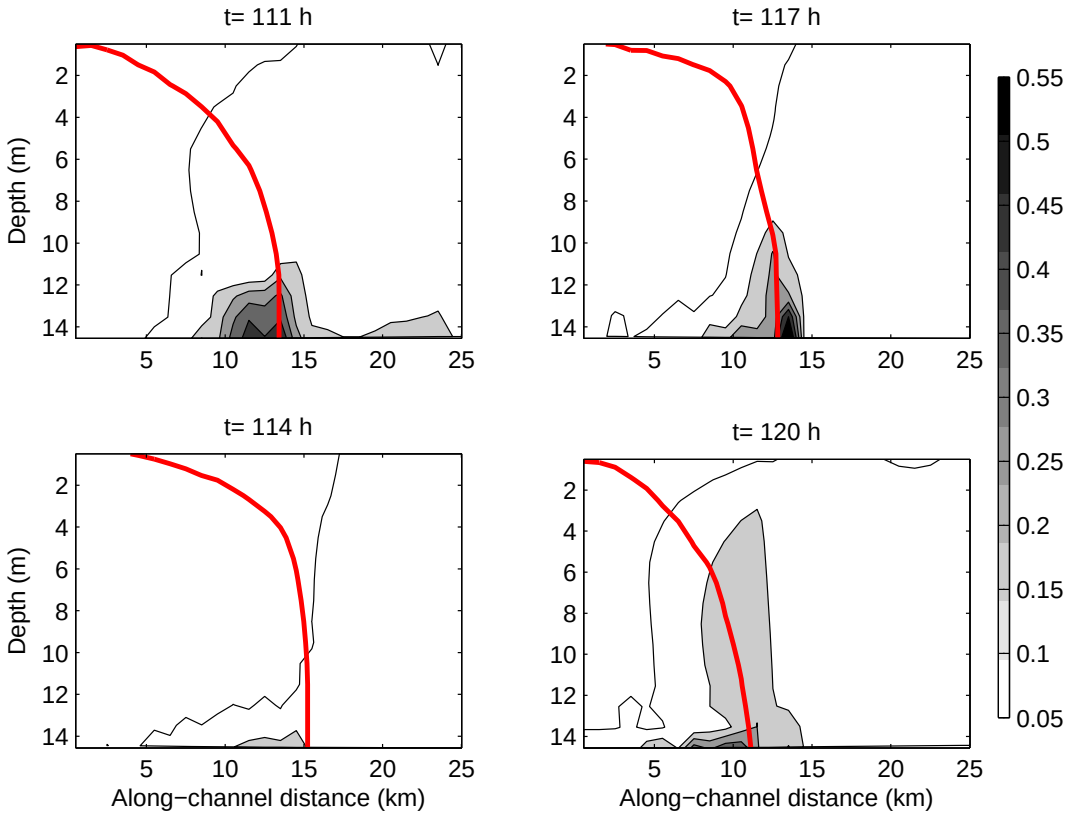

Figure 8 Instantaneous SSC distributions along the channel axis with contour interval 0.1 kg m^{-3} (solid lines) from hour 111 to 120 for size-resolved flocculation simulation with Earth rotation. The red line represents 1 psu isohaline (the salt front). The hour 111 denotes maximum flood, and hour 117 denotes maximum ebb.

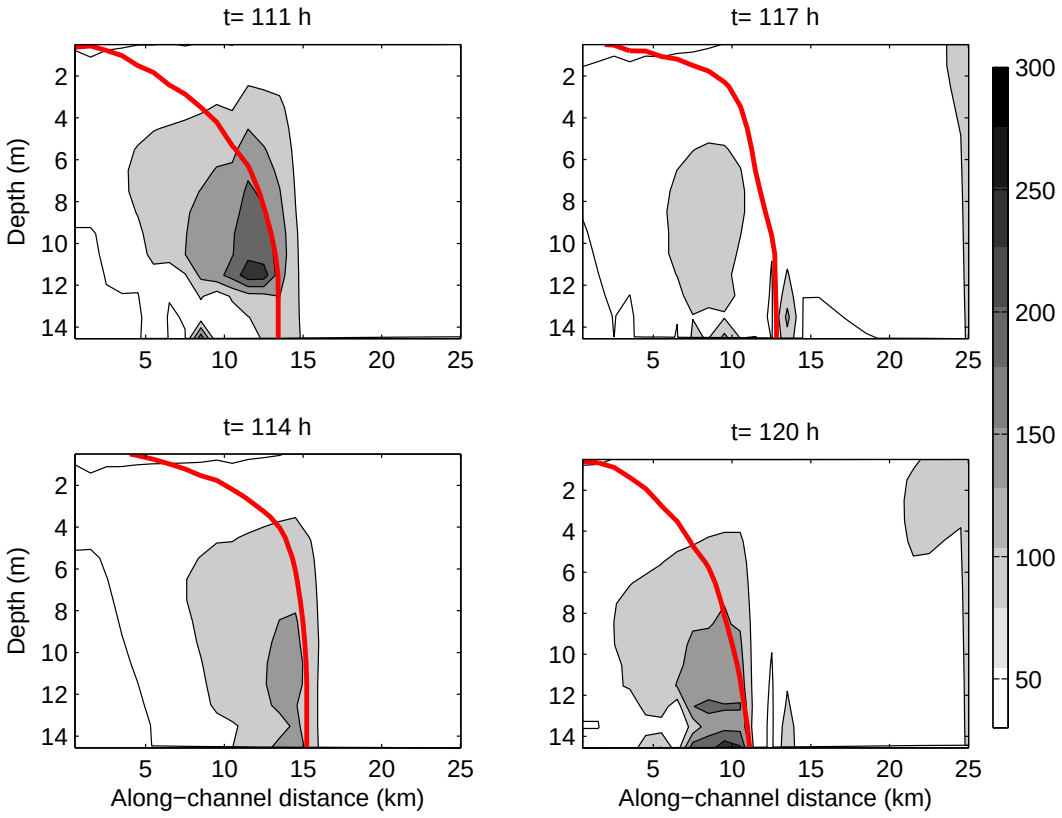

Figure 9 Instantaneous median floc size (D_{50}) distributions along the channel axis with contour interval 50 μm (solid lines) from hour 111 to 120 for size-resolved flocculation simulation with Earth rotation. The red line represents 1 psu isohaline (the salt front). The hour 111 denotes maximum flood, and hour 117 denotes maximum ebb.

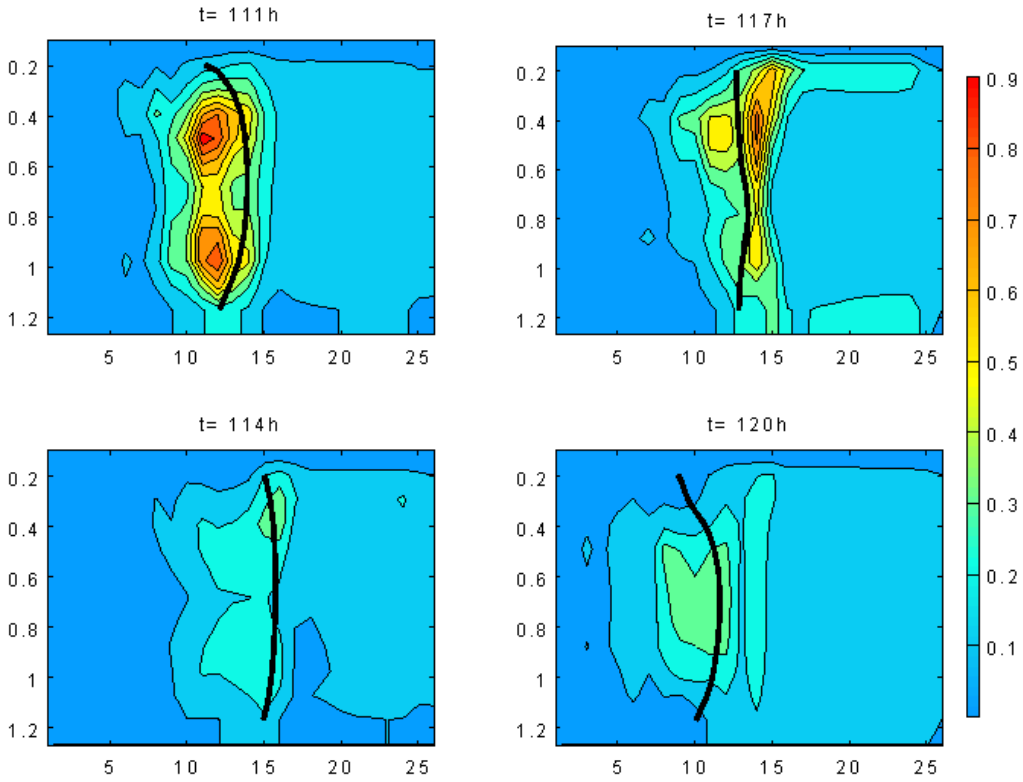

Figure 10 Instantaneous near bottom SSC distributions from hour 111 to 120 for size-resolved flocculation simulation with Earth rotation. The black line represents 1 psu isohaline (the salt front).

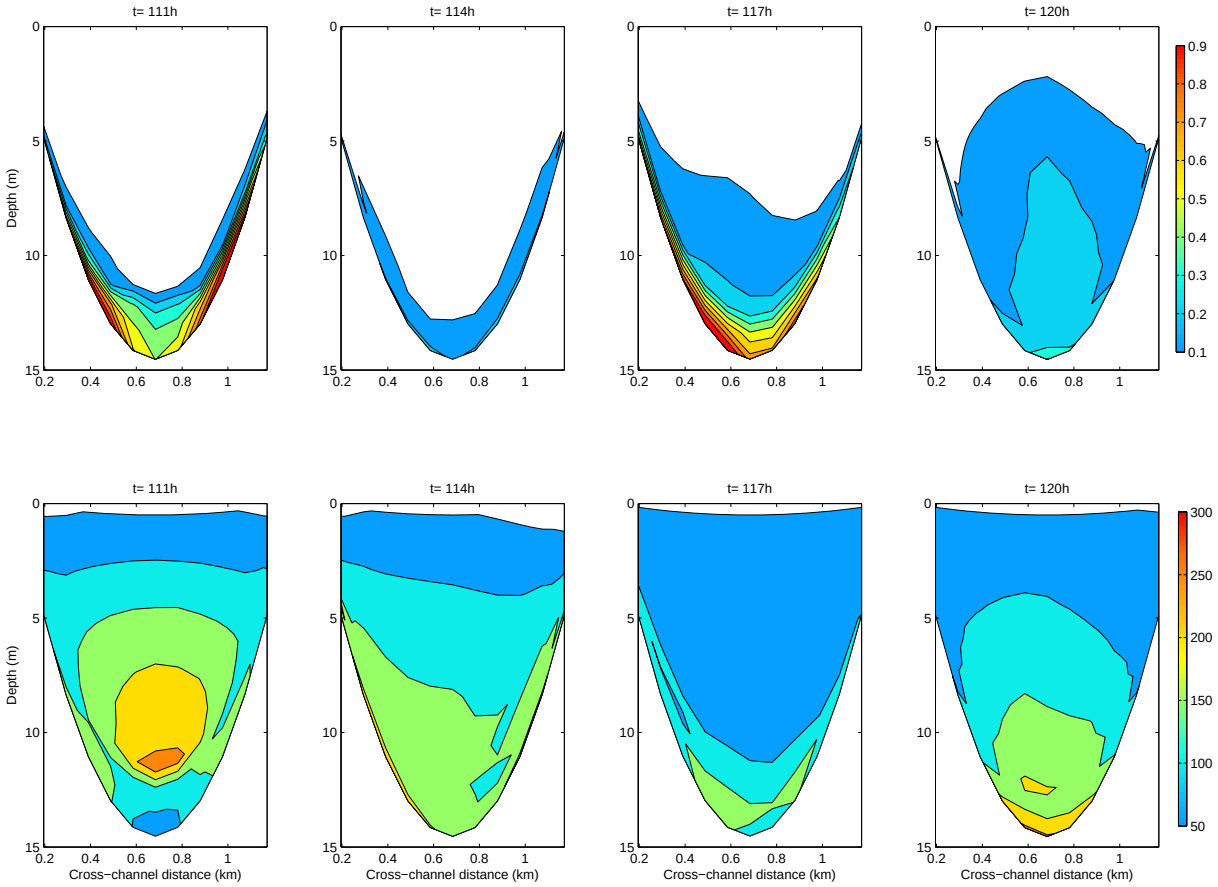

Figure 11 Cross sectional SSC distribution contour with interval 0.1 kg m^{-3} (upper panel), and the median floc size contour with interval 50 μm (lower panel), following the maximum SSC from hour 111 to 120 for size-resolved flocculation simulation with Earth rotation. The hour 111 denotes maximum flood, and hour 117 denotes maximum ebb.